NDOT Research Report

Report No: RDT04-046

A STUDY OF SHAPE-MEMORY-ALLOY REINFORCED BEAMS AND CUBES

July 2004

Prepared by Research Division
Nevada Department of Transportation
1263 South Stewart Street
Carson City, Nevada 89712

NEVADA DOT

This work was sponsored by the Nevada Department of Transportation. The contents of this report reflect the views of the authors, who are responsible for the facts and the accuracy of the data presented herein. The contents do not necessarily reflect the official views or policies of the State of Nevada at the time of publication. This report does not constitute a standard, specification, or regulation.

TECHNICAL REPORT DOCUMENTATION PAGE

1. Report No. RDT 04-046	2. Government Accession No.	3. Recipient's Catalog No.
4. Title and Subtitle A Study of Shape-Memory-Alloy Reinforced Beams and Cubes	5. Report Date October 2003	
	6. Performing Organization Code	
7. Author(s) Chadi Ayoub, M. Saiid Saiidi, Ahmad Itani	8. Performing Organization Report No. CCEER-03-07	
9. Performing Organization Name and Address Center for Civil Engineering Earthquake Research Department of Civil Engineering University of Nevada Reno, NV 89557	10. Work Unit No.	
	11. Contract or Grant No.	
12. Sponsoring Agency Name and Address Nevada Department of Transportation 1263 South Stewart Street Carson City, NV 89557	13. Type or Report and Period Covered	
	14. Sponsoring Agency Code	
15. Supplementary Notes		

16. Abstract

Collapse and severe damage of reinforced concrete structures during strong earthquakes has been a major concern for structural engineers. Current and past research has been based on yielding steel reinforcement in order to dissipate the earthquake energy. This meant the preserving of lives, but at the expense of structures, which would be severely damaged. In this report, the super-elastic behavior of shape memory alloys, in particular Nitinol, was used in doing preliminary tests to observe the extent of the ability of this alloy to confine concrete, decrease and minimize residual crack sizes in concrete, and to recover and reduce permanent deformations under cyclic loads. Eight small- scale beams and eleven cubes were tested. It was found that shape memory alloy reinforcement reduced the permanent beam deflection by more than 75% but did not reduce permanent damage in the cubes.

17. Key Words Earthquakes, earthquake energy, shape memory alloys, Nitinol, residual crack sizes, concrete		18. Distribution Statement **Unrestricted. This document is available through the National Technical Information Service, Springfield, VA 21161**	
19. Security Classif. (of this report) Unclassified	20. Security Classif. (of this page) Unclassified	21. No. Of Pages 139	22. Price

ACKNOWLEDGEMENTS

The study presented in this report was partially funded by Nevada Department of Transportation (NDOT) contract P364-00-803. The views expressed in the report are those of the authors and do not necessarily represent the views of NDOT.

Special thanks are due to Dr. Patrick Laplace, Mr. Paul Lucas, Mr. Jesus Pedroarena, and the staff of the Civil Engineering Department for their help and support.

This report is based on a Master thesis by the first author supervised by the other authors.

TABLE OF CONTENTS

LIST OF TABLES

LIST OF FIGURES

CHAPTER 1: INTRODUCTION

1.1 Background

Collapse and severe damage of reinforced concrete structures during strong earthquakes has been a major concern for structural engineers. Research has been performed on improving seismic designs to ensure the safety of human lives and important structures such as bridges. Current and past research was based on yielding steel reinforcement in order to dissipate the earthquake energy. This meant maintaining the structural integrity. However, the structure would be severely damaged. In this report, the super-elastic behavior of Nitinol (NiTi), one of the most used shape memory alloys (SMAs), is going to be used in doing preliminary tests to observe the extent of the ability of this alloy to confine concrete, decrease and minimize residual crack sizes in concrete, and to recover and reduce permanent deformations caused by applied loads on it. This characteristic of NiTi can cause a major leap in seismic design, since the base of seismic design is to yield steel to dissipate energy while encountering permanent deformation, whereas NiTi would yield under strains accompanied by seismic loads and recover deformations fully [1,2,3]. This research is a preliminary study in to understand this material.

During the last quarter of the 20th century, a new group of alloys evolved and started to be used extensively in many different areas, in engineering and non-engineering aspects [1,2]. These alloys are called shape memory alloys (SMA). SMAs are used in many different fields such as medical and orthodontic equipment, fighter jets, and even shoes and clothing. SMAs possess unique properties, which allowed them to be addressed as smart composites [1,2].

In general, SMAs exhibit two distinct crystal structures or phases [4,5,6]. These phases are martensite (M-phase) and austenite (A-phase) and are totally dependant on one or two of the three thermo mechanical variables, which are: existing temperature of the composite, the amount of mechanical loads or stresses applied, and strain [1,2,3]. Thus, the properties of SMAs are dependant on the amount of each crystal phase present. martensite is the more deformable, lower temperature phase and austenite is the stronger, higher temperature phase present in SMAs [1,2,3]. SMAs exhibit six unique properties. These six properties are: shape memory effect (SME) one-way memory, SME two-way memory, super elasticity, damping hysteresis, and practical absence of fatigue and corrosion effects [1,2,3].

In order to understand the reasons behind these unique properties, one must understand certain terminologies about these kinds of alloys. Shape memory alloys are composed of martensite and austenite, the reverse and forward thermo elastic crystallographic martensitic reversible transformation that determines the properties of SMAs (Fig. 1-1) [1,2]. The SMA starts to transform into the low temperature, martensite, when cooling down to the martensite start temperature (M_s) [1,2,3]. The transformation is complete after the temperature is cooled down past the M_s, down to the martensite finish

temperature (M_f). When in this phase, the alloy behaves ferro-elastically and can be easily manipulated in a very large strain range [1,2,3] (Fig. 1-2). In between the M_s and M_f, the alloy would exist in both the martensitic and austenitic phases [1,2,3] (Fig. 1-3). In contrast, when heating the alloy past the austenite start temperature (A_s) up to the austenite finish temperature (A_f), the alloy starts transformation into the stronger higher temperature austenite phase and completes transformation [1,2,3] (Fig. 1-4). The critical temperatures where the transformation occurs can be chosen in a temperature range between –302 degrees Fahrenheit (–150 degrees Celsius) and 392 degrees Fahrenheit (200 degrees Celsius) [1,2]. This depends on the alloy composition and micro structural constitution, the latter determined by the thermo mechanical process.

Through SME, the material has the ability to memorize a very specific configuration either in martensite or austenite phase, which is known as one-way memory (Fig. 1-5) [1,2]. Also, SMAs are capable of being trained in memorizing two different deformations in the two different phases. Deforming the alloy in the martensitic phase and heating it into the austenitic phase, at which it regains its original size prior to deformation, and by repeating this cycle many times, would achieve this (Fig. 1-5). Another interesting characteristic of SMAs is pseudo-elasticity (Fig. 1-4) [1,2]. Pseudo-elasticity is the name given to the super elastic characteristic of the SMAs. SMAs could reach strains up to 10 % and still fully recover their deformation (Fig. 1-4) [1,2,3]. Pseudo-elasticity exists in the alloy when it is above the austenite finish (A_f) temperature. Within such a range, SMAs could go through hundreds of deformation cycles (up to their maximum recoverable strains) without any accumulation of residual strain [1,2]. Finally, SMAs are known to possess a high damping capacity, in both austenitic and martensitic phases, but with a slightly higher capacity in martensite phase [7]. This is due to the stress-induced martensitic transformation and reorientation of martensitic variants under the application of an external load, respectively [1,2,3]. However, the damping hysteresis is affected by the internal and external parameters such as temperature, frequency, time, strain amplitude, alloy content, grain size, and densities of the martensite and austenite phases present [1,2].

In general, the characteristics of SMAs can be categorized into three groups. The first category would be the typical features of martensite: higher damping with respect to austenite, and the ability to completely recover residual strain by heating (shape memory effect). The second category is the typical features of austenite: Nominally zero residual strain up to 10% under arbitrary mechanical loading (pseudo elastic effect). The third and final category is the common features of both phases: high damping capacity, and practical absence of fatigue and corrosion effects.

In this study, the super elastic property occurring in the austenitic phase of the SMA, specifically Nitinol (NiTi) is investigated. NiTi has a thermal coefficient similar to that of concrete with a value of 6.11×10^{-6} / deg. Fahrenheit (11.0×10^{-6} / deg. Celsius) [8,9,10,11]. This means that under temperature fluctuations, no significant internal thermally induced stresses are present in the system.

1.2 Literature Review on Shape Memory Alloys

There is no research conducted on the ability of NiTi to confine concrete. Also little research has been directed towards understanding the ability of SMAs to recover deformations, and decrease residual deformations in concrete beams. Almost all research done on deformation recovery ability of NiTi is based on the induced recovery stresses applied on a structural component. This occurs by transforming SMA reinforcement, which is present in the martensitic phase in the structural component, into the super elastic austenitic phase by increasing its temperature through heat application. In this review, the most relevant investigations to the current study were included.

1.2.1 Self-Stressing Fiber Composites (Ref.12)

In this technical paper, shape memory alloy (SMA) composites were tested for their ability to improve reinforcing and prestressing of concrete structures. SMAs are addressed as smart composites that are able to deform and have their dimensions change and adapt with environment such as by heat, electricity or radiation treatment. Because plastic deformation of SMAs applied during the initial martensic phase can be recovered, SMAs original dimensions can be said to 'preserve' its original shape. Such physical changes undergone by phase changes can be used in prestressing of concrete. Using plate shaped concrete specimens, the authors tested the concept of self-stressing composite with SMAs. Two were plain mortar, five were steel wire reinforced, and two were SMA reinforced. Results obtained showed that SMA fibers allow self-stressing composites capable of self-healing in which significant deformation beyond the first crack can be fully recovered and cracks can be fully closed. If low water-cement ratio (<0.3) was used, healing due to natural weathering can take place allowing for reoccurring prestressing of element several times thus elongating life of structure. Results also showed that deflection due to loads could be fully recovered after unloading. Additional benefits included less deflection and smaller strains. The data also showed that higher tensile stresses can be applied, cracking can be delayed or avoided under service load conditions, and the ultimate capacity can be increased.

SMA Dampers (Ref. 13 and 14)

Experimental and analytical tests were performed on the ability of SMAs to dissipate energy by using SMA dampers made by wrapping SMA wire between two cylindrical support posts. Clark et al. [13] and Krumme et al. [14] found out by tests that SMA damping devices reduced accelerations and structural displacements by $\frac{1}{3}$ to $\frac{1}{2}$ over conventionally designed structural systems. Thus it can be used for structural vibration control. In addition to that, they found out that SMAs exhibit excellent fatigue life.

1.2.3 Damping Properties of Beams with Embedded SMA Fibers (Ref. 15)

In this paper, analytical and experimental methods are proposed to find out the damping effect of applying or embedding SMA fibers, made of Nickel and Titanium (Nitinol), into epoxy beam structural members. To observe the damping effect, two systems were introduced. The control variable was solely an electric current, which had an effect on the temperature of SMA fibers. Electric current would increase temperature of SMA fibers, thus allowing them to transform from the martensite to austenite phase at which causes the Nitinol fibers to become stiffer due to the effect of pre-straining back to its original shape. The damping effect was observed by comparing a beam with embedded Nitinol fibers and a DC voltage applied to it, with a similar beam with no current applied to it. Experimental results and discussion show that vibrations were reduced significantly. It also showed that initial vibration had higher frequency amplitude, which was induced due to the initial increase of stiffness of the composite matrix (due to the phase transformation, martensite to austenite), followed by a substantial decrease in frequency amplitude later on.

1.2.4 Stiffening Composite Materials By Embedding SMA Fibers (Ref. 16)

Shape memory alloy fibers (SMA), unlike normal plastics, have the ability to fully recover deformation when subjected to heating. Thus, SMA fibers embedded in composites can be used to control shape, elastic moduli, internal stress level and natural frequencies of vibration of the composites. In this paper, an experiment was done mainly to test the effect of SMA fibers in composites on vibration or damping of composite. Through testing, a new phase was introduced and compared to martensitic and austenitic phases. This phase is the R-phase transformation (rhombohedral distortion of the original austenitic structure), which precedes the martensic transformation. This distortion is characterized by small transformation strains, a large stress rate change with respect to smaller temperature changes, and a very small hysteresis (small temperature rate change required to transform). This phase has two important advantages over the other phase changes. It has a very high recovery stress with minimum temperature increases and higher durability due to lower shear stresses at fiber-matrix interface. Experiments done using SMA fibers embedded into an epoxy beam with the use of a shaker, strain gauges and a DC electric current applied to it gave results showing that vibrations can be controlled by applying currents on fibers, thus lowering frequency amplitudes of vibration of the composite matrix.

Overview of SMA Performance (Ref. 17)

In this paper, a brief review of SMA's thermo mechanical characteristics such as pseudoelasticity and phase transformation, shape memory effect, and damping was presented. Then the modeling aspects of such behaviors were explored followed by a literature review of different structural applications of Ti-Ni SMAs (Nitinol). Damping of SMAs was discussed in detail. SMAs posses a high damping capacity in both martensite-phase and austenite-phase. The damping property in SMAs is also controlled by

temperature, time, frequency, strain amplitude, and alloy content, grain size and phases interface. Damping capacity of SMAs in martensite-phase is a function of annealing temperature. Damping increases with temperature up to a temperature of 550 deg. Celsius (1022 deg. Fahrenheit), above which a reverse effect of decreasing damping capacity is seen. In addition, SMAs in martensite-phase adopt a decreasing damping capacity when undergoing an increasing number of loading cycles (tension-compression) until they reach a stable limit. Tests have shown that SMAs in austenite phase acquire less damping capacity than SMAs in martensite phase. Experimental studies show that if heat transfer from SMAs to surrounding medium were enough to assure an isothermal condition during loading, this would not allow the strain rate to affect the pseudoelasticity of the alloy. This is due to the fact that self-heating of SMAs has an effect on pseudoelasticity of material, and an increase in temperature causes a shift in the stress-strain hysteresis loop upward.

Retrofit of Bridges Using SMA Restrainers (Ref. 18)

The possibility of using Nitinol shape memory alloy rods as restrainers in multi-frame bridges was explored. Nitinol alloys exhibit three unique properties that allow it to be a good substitute for steel restrainers. The properties are: (1) shape memory effect, (2) super-elasticity, and (3) high damping characteristics.

Initially, tests were performed to study the effect of bar size on the super-elastic property of Nitinol (NiTi). Two specimens were used, a NiTi wire with a diameter of 0.070 inches (1.78 mm) and a rod with a diameter of 0.500 inches (12.7 mm). The test setup consisted of cyclic loading of the specimen up to strains of 60,000 **me**. Stress-Strain graphs were generated. The graph of each specimen showed substantial differences. The graph of the wire showed the classic "flag-shape" hysteresis whereas the rod showed a smaller hysteresis loop. This implied that the equivalent viscous damping in the rod (2.1%) was smaller than that of the wire (7.0%) at 6% strain. Another point is that residual strain in the rod (3,000 **me**) was smaller than that of the wire (5,000 **me**). In the case of the rod, upper loading plateau stresses occurred at 40-50 ksi (276-345 MPa), whereas in the NiTi wire, it occurred at 80 ksi (552 MPa). However, the rod exhibited a higher stress of 110 ksi (758 MPa) at 60,000 **me** strain compared to the wire that had a stress of 80 ksi (552 MPa). The stress-strain curves of the rod show that the centering potential in NiTi is excellent. This is the property that will be most useful in using NiTi as bridge restrainers. An analytical modeling of a four frame, 11-span reinforced concrete Box-girder bridge supported on single column bents was used. The bridge was analyzed in three ways: (1) without restrainers, (2) steel cable restrainers and (3) SMA restrainers. Restrainers were used to connect the end of each box girder to the beginning of the adjacent box girders. The analytical modeling consisted of using a 2-dimensional non-linear model of the bridge developed using DRAIN-2DX non-linear analysis program. The output results showed a maximum relative hinge displacement of 6.79 inches (172.5 mm), a 6.05 inches (153.7 mm) displacement (11% reduction) using conventional steel restrainers, and 3.94 inches (100.1 mm) displacement (42 % reduction) using SMA restrainers. The reasons for the effectiveness of using SMAs compared to conventional steel is that SMAs remained elastic for repeated cycles, whereas steel yielded, thus allowing the SMAs to have a greater

effective stiffness. Another point is the added stiffness in SMAs caused by strain hardening at large strains.

Design and Application of the SMA Devices in Walls (Ref. 19)

The advantages of using shape memory alloys (SMAs) in retrofitting gable-end walls were explored. A common intervention technique used to prevent the rocking of gable-end walls is to improve the connection between façade walls and floors and/or orthogonal walls by means of steel tie rods. Such a technique has been observed, from past earthquake damage, not to prevent collapse. Furthermore, the steel bars that are used as ties have a high stiffness that causes high forces to be transmitted to the masonry structure under earthquake loads. This causes the connection to fail due to the punching effect of the anchorage. SMAs have an initial stiffness lower than that of steel and an upper plateau that has a fairly constant force while undertaking a substantial deformation. In addition, SMAs have a good energy dissipation capacity that helps reduce damage while increasing structural capacity. Therefore, using SMAs to connect façade walls and floors and/or orthogonal walls, in conjunction with conventional steel tendons for masonry post-tensioning, has shown to be useful in preventing flexural collapse of tall and slender masonry structures such as bell towers and columns.

Shape Memory Alloy Ties (Ref. 20)

Application SMA ties to connect the external walls to the floors or roof or to the perpendicular walls was explored. Such a connection should be designed to behave as the following:

a) The SMA device does not apply any static force on the structural element under static loads.
b) The SMA device should remain stiff, as conventional steel does, not allowing significant displacements under low intensity dynamic horizontal actions (winds, small intensity earthquakes).
c) The stiffness of the SMA device decreases under high intensity earthquakes. This occurs under the fairly constant force of the super elastic upper yield plateau property of SMA. This allows the wall to have controlled displacements. This behavior should reduce the amplification of acceleration as compared to stiffer connections.
d) Under dynamic horizontal actions higher than design loads, the stiffness of the SMA device would increase sharply due to strain hardening, thus preventing instability and collapse of structure.

Critical points in the design of such a connection was in defining the amount of controlled displacement and the yield force level at which the SMA device stiffness should decrease. Higher controlled displacements cause higher damage in the structure.

Shape Memory Alloy Devices for Masonry Prestressing (Ref. 21)

The use of shape memory alloys (SMAs) in the prestressing of masonry walls was studied. The SMA wires were prestressed to a point where they were in the middle of their super elastic range. The length of the prestressed wired was determined by the amount of displacement required, and the super elastic range (maximum strain before strain hardening) of the SMA wires. This is implemented in a way that the SMA wires remain in the upper plateau super elastic range under all loading conditions. This prestressing method was recommended for shear masonry wall mock-up, structures subjected to in-plane loading, or for horizontal ties aimed at preventing out-of-plane collapse.

Comparison between Structures Unprotected and Protected with SMA Cables (Ref. 22)

The response of rigid bodies, representing simple models of ancient column or colonnades was studied. Prototypes used represent much larger structures. These models were subjected to various types of pull out static tests, and sinusoidal and earthquake base motions at the Earthquake Simulator Facility at Aristotle University in Greece. Comparisons were made between prototypes reinforced with SMA wires and unreinforced prototypes. The rigid prototype models used in this experimental study were made of either steel or marble. Steel prototypes represented structures that were 20 times larger, whereas the marble prototypes represented structures that were 7 times larger. Four prototypes were studied. They were: Single steel column prototype, two steel column colonnade, four steel column colonnade, and two marble column colonnade. Conclusions of the experimental tests were that insertion of SMAs in the prototypes had a noticeable favorable influence on their stability. The model structures with SMAs developed stable response at amplitudes higher than those of the models without SMA reinforcement.

Retrofit of Experimental Masonry Walls with SMA (Ref. 23)

The effects of retrofitting classical masonry walls with three SMA cross brace devices at the lower level on each face of the wall were studied. Boundary conditions imposed on the walls were as follows:

1. Beam rotation at the top of the wall was not allowed to simulate the continuity of the wall with other parts of the structure.
2. The upper part of the wall above the openings was constrained by a tendon to simulate a traditional retrofitting technique used on such structures.

The seismic input chosen was from a measured record in Lisbon, Portugal. It was modified to meet the requirements of the Eurocode 8. The unprotected wall was subjected to 0.7xLisbon, 2xLisbon (2 runs), and 3xLisbon. Severe damage occurred on the end of the second 2xLisbon loading event. The wall collapsed in the middle of the loading event of 3xLisbon. The SMA protected wall was subjected to 0.7xLisbon, 2xLisbon (2 runs), 3x Lisbon, 4xLisbon, and 5xLisbon. Damage at 4xLisbon of the protected wall was similar to that of the unprotected wall at 2xLisbon. Collapse of the protected wall occurred at 5xLisbon.

Out of Plane Response of a Masonry Wall Retrofitted with SMA Tendons (Ref. 24)

The effectiveness of using SMAs for retrofitting walls to prevent it from out-of-plane collapse in masonry structures was studied. Two identical masonry walls were constructed and connected to a stiff steel frame and placed together on a shaking table. The stiff steel frame represented the rest of the structure. The test variable was the connection between the walls and the steel frame. One of the connections was made of conventional steel tendons while the other was made of SMA tendons. The SMA connection was designed based on the following three points:

1. Under service loads, SMA tendons do not apply any static force to the linked structural elements.
2. Under low intensity horizontal actions, the SMA remains stiff in the elastic region.
3. Under higher intensity horizontal actions, SMA yields while remaining in the super elastic upper plateau yield state accompanied by a reduction in its stiffness. This enables controlled displacements in the wall while dissipating energy.
4. Under extraordinary horizontal actions, the SMA connections enter strain-hardening phase and its stiffness increases dramatically, thus preventing excessive displacements that could destabilize the wall.

Test results showed that the steel linked wall collapsed under higher loads than that of the SMA linked wall. On the other hand, the overall damage of wall was less with SMA connection. SMA was shown to increase resistance against out of plane seismic vibrations of such masonry walls by at least 50 % while reducing the top acceleration of the wall by 50 %.

Control of Permanent Deformation Using Advanced Composite Materials (Ref. 25)

The response mechanism of a composite moment resisting frame system with self-centering and energy dissipation capabilities was investigated. Although shape memory alloys were not used in this investigation, the advantageous utilization of the lower stiffness design of structural components and low residual displacements shown in this paper are relevant to the lower stiffness issue of Nitinol reinforced sections that was used in the present study.

In this study, 4 portal frames were tested under lateral loads and tests were terminated at 5% drift. Specimen number one was a conventional steel reinforced frame. Specimen number two had an FRP-reinforced (Aramid) columns and steel reinforced beams. Specimens number three and four had CFRP-reinforced columns and steel reinforced beams.

In contrast to conventional steel reinforced moment resisting frames, specimens number two, three and four were accompanied by plastic hinge formations in the beams, which was used for energy dissipation, without formation of plastic hinges at the base of the columns. Such a performance does not cause a potential collapse mechanism. The relatively large elastic deflection capacities of the columns were achieved by combining elastic FRP bars with engineered cementitious composites (ECC). ECC has a higher tensile

and deformation capacity than normal concrete. It was found that the use of ECC in combination with FRP could increase the deflection capacity of the columns and delay concrete failure that can be caused at high deflections. Permanent deflections were also reduced substantially.

1.2 Objectives and Scope of Study

The investigation described in this document was aimed mainly at the determining the ability of Nitinol (NiTi) to recover deformation when used in combination with concrete. In addition, confinement effect of NiTi on concrete cubes was explored.

The goals of this study were to investigate (a) the flexural behavior of simply supported beams under cyclic two point loads, and (b) the confinement properties of NiTi under cyclic vertical loading in concrete cubes. The test variables in the beams were the material and ratio of the longitudinal reinforcement in the critical region. Eight beams were tested, four of which were longitudinally reinforced with NiTi, and four with conventional steel. The test variables in the cubes were also the material and size of the bars used for confinement. Eleven cubes were tested, three were unconfined, four were confined with NiTi, and four were confined with steel.

The primary objectives of the research were:

1. Determining the effect of using NiTi as longitudinal reinforcement in beams on the displacement recovery and residual displacements.
2. Determining the effect of using NiTi as longitudinal reinforcement in beams on the curvature recovery and residual curvature.
3. Determining the effect of using NiTi as longitudinal reinforcement in beams on the residual cracks in the beams.
4. Determining the effect of using NiTi as longitudinal reinforcement in beams on the stiffness of the beams.
5. Determining the effects of using NiTi longitudinal reinforcement in full-scale beams and hybrid systems using theoretical models.
6. Determining the concrete confinement properties provided by NiTi and comparing it with that from steel.
7. Determining the ability of NiTi to recover deformation when used for confinement in concrete cubes and comparing it with that from conventional steel.

CHAPTER 2: TEST SPECIMENS

2.1 Introduction

Unlike steel, Nitinol (NiTi) is unknown to structural engineers. Its interactive behavior with concrete is unknown and needs to be studied before being used in new design or retrofit. To understand the behavior of NiTi, initial tests were conducted in order to observe some of the basic interactive properties between NiTi reinforcements and the concrete. Numerous tests needed to be done. Due to the cost and time involved in the testing, smaller specimens were used in the present study. The specimens chosen were standard sized concrete cubes and small-scaled beams. This chapter describes the test specimens and the material properties.

2.2 Selection of Representative Specimens

Three points were to be observed in the experimental tests: The confining capability of the NiTi, the stress-strain relationship of this material (Fig. 2-1), and the ability of NiTi to recover deformations due to applied stresses after yielding. Two categories of specimen were designed and constructed. The specimens were chosen to be small and numerous so that several test variables could be studied.

The first category consisted of fourteen, six inch (150 mm) concrete standard cubes. Six of those cubes were used to test the unconfined strength of the cubes. The remaining eight cubes were confined. The second category consisted of designing and building eight beams.

2.3 Test Specimens

2.3.1 Nitinol Rods

Although Nitinol (NiTi) is very expensive, it is actually one of the least expensive shape memory alloys (SMA) available in the market due to its availability and customer demand. NiTi was chosen for the experimental tests because of its relatively low and stable transformation temperatures. Unlike other SMAs, the Austenite finish transformation temperature can be chosen to be as low as –50 degrees Fahrenheit (-10 degrees Celsius), thus having pseudo-elastic behavior with no residual strains at temperatures above –50 degrees Fahrenheit. This temperature range is ideal for most field conditions.

The second step was to decide on where to place the Nitinol reinforcement to confine concrete, inside the concrete or outside as jackets. Two factors were to affect the decision. The first factor was that Nitinol is super-elastic, thus its ability to reach high strains and recover deformations (up to 0.08), even after yielding without any residual strains, implied that concrete was to fail long before the Nitinol. This implied that the

Nitinol is re-usable. On the other hand, placing the Nitinol confinement in the concrete would ease construction and setup of tests. Since many specimens were going to be tested, and due to economical reasons, external confinement was used to facilitate the removal and the reuse of the SMA rods.

First, the mechanical and physical properties of Nitinol were the reasons for it being chosen. Secondly, the dimensions and the shape of the NiTi to be used had to be chosen. At this point there were other factors that influenced the final decision. These factors were: connections, economy, and time to build the models.

After consulting with shape memory alloy suppliers, three common shapes of Nitinol were found to be available. These shapes were: Nitinol sheets, Nitinol wires, and Nitinol bars. By inspection, the Nitinol sheets would have been most reasonable. However, reasons for not choosing it will be discussed next.

Connecting Nitinol is not a straightforward issue. Sample wires were sent to companies to test the reaction of Nitinol towards welding. Two kinds of welding methods were tested. The first was conventional welding methods and the second was cold welding. The material turned out to be extremely sensitive to both methods. Tensile tests on these connections showed that strength of welded connections is significantly lower than the strength of Nitinol. This early discovery lead to the decision of using the bars in the experimental tests, together with the cube and beam specimens. The methods and reasons for using the Nitinol bars with the cube and beam specimens will be discussed in the following sections.

2.3.2 Concrete Cubes

Eleven 6 inch (150 mm) standard concrete cubes were chosen (Fig. 2-2 and 2-3). The side dimension was chosen to be 6 inches (150 mm), to be consistent with the standard cube size.

2.3.3 Beams

Eight small-scale beams were constructed (Figs. 2-5 to 2-9). The beams were 5 feet (1.53 m) long with a cross sectional area of 5 x 6 inches (127 x 152 mm) in the middle area and a cross sectional area of 5 x 12 inches (127 x 305 mm) at the ends. The beams were chosen to have this shape due to reasons explained in section 2.4.2. The test variables were the type and amount of reinforcement in the critical section (Table 2.1). The specimen names are B-N-L-1, B-N-H-1, B-N-L-2, B-N-H-2, B-S-L-1, B-S-H-1, B-S-L-2, and B-S-H-2. The letter B is short for beam, the letter N or S is short for Nitinol and steel respectively, the letter L or H is short for low and high respectively, and the number 1 or 2 denotes the number of bars used as longitudinal reinforcement at mid-section. Low and high are used to point to the 0.375-inch (9.525 mm) and 0.5-inch (12.7 mm) NiTi bars, respectively in B-N beams, and #3 (Ø10) and #4 (Ø13) bars, respectively in B-S specimens.

All beams had the same dimensions. The beams were divided into two groups. Each group consisted of four beams. Group 1 (B-N-L-1, B-N-H-1, B-N-L-2, B-N-H-2)

was reinforced in the longitudinal direction in the middle of the beam with Nitinol rods while group 2 (B-S-L-1, B-S-H-1, B-S-L-2, B-S-H-2) was reinforced with conventional steel bars. Beams with conventional steel were used to establish the benchmark.

Two different sizes of Nitinol rods were used. The first one consisted of 0.50-inch (12.7 mm) rods and the other consisted of 0.375-inch (9.525 mm) rods. Both rods had reduced sections (dog bone) in the middle. The half-inch rod had a reduced diameter section of 0.375-inches (9.525 mm), while the 0.375-inch (9.525 mm) rod had a reduced diameter section of 0.25 inches (6.35 mm). These reductions were made to avoid failure in the threaded section at the ends.

Two different conventional bar sizes were used. The first was # 4 (F13 mm) bar and the second was # 3 (F10 mm) bar. Tensile tests were performed on sample bars to determine the yield strengths.

2.4 Design of Specimen

2.4.1 Concrete Cubes

The cubes were to be experimentally tested under uniaxial load. The focus of the tests was to test confining effects of Nitinol (NiTi) on concrete. Two prefabricated holes were embedded in the concrete cubes (Fig. 2.2). $^{3}/_{8}$ (9.525 mm) and $^{1}/_{2}$ (12.7 mm) of an inch diameter Nitinol bars were used in the tests, and would go through the prefabricated holes. In addition, conventional # 4 (F13) and # 3 (F10) Grade 60 steel bars were used in the experimental tests. The Nitinol confinement effect was compared and judged based on the confining ability of conventional steel bars.

Nitinol and steel bars were all 10 inches (2540 mm) long. All were threaded over 1 inch (25.4 mm) from each end. These bars were passed through the cubes, and 4-inch (10.16 cm) steel plates with drilled holes in their center were attached to the bars from both ends. Each bar had on one end a steel plate only attached to it, and then Grade 80 washers and nuts came on top to fasten the plate to the side of the cube. On the other end, a small 1-inch (10.16 cm) long steel pipe, with a 2.5 inch (6.35 cm) outer diameter came around the bar. This pipe acted as a protection and cover for the strain gages that were going to be placed in this region on the bar itself. A 3-inch plate with a drilled hole right in the center was placed on top of the pipe. Then Grade 80 washers and nuts were used to fasten them to the cube.

The only concern with testing the cube was the rigidity of the plates and buckling of the pipes. Iterative finite element analysis was performed on the 4-inch (76 mm) plates to estimate the thickness of the plate required to achieve satisfactory rigidity. This was done by assuming a thickness for the plate and then analyzing it under an 800-psi (5.52 MPa) pressure. Rigidity in this case was defined as having a maximum deflection in the plate of 0.005 inches (0.127 mm) under a confining pressure of 800 psi (5.52 MPa). Iterative finite element analysis using the Structural Analysis Program (SAP 2000, [33])and market availability implied the use of Grade A36 steel with a thickness of ½ an inch (12.7 mm). This would give a deflection of 0.0043 inches (0.109 mm) under a

confining pressure of 800 psi (5.52 MPa). Finally, the pipes were checked for buckling capacity.

2.4.2 Beam Design

The beams were tested under two point loads in the middle. The two loads were 6 inches (152 mm) apart thus subjecting the mid-part of the beam to pure constant flexure. The test variable was the reinforcement ratio in mid-section. A varying number of bars used and/or cross-sectional area of the bars achieved this. Figures 2-10 and 2-11 show the test setup. "Mid-section" will refer to the constant moment region of the beam. "Outer-sections" will be used to refer to the sections of the beam outside the mid-section. The Nitinol rods available for testing were 10 inches (254 mm) long. NiTi is re-usable since it fully recovers deformation after yielding without residual strains. To minimize testing cost, the beams were reinforced from outside the concrete area of the beam. Embedding the NiTi rods in the beams meant using more rods. Thus anchoring them to the beam from the outside allowed for re-using the NiTi rods.

The idea behind the beam design test setup was to have strong and over-reinforced outer-section beam parts relative to the mid-section where the rods were going to be placed. The first step was to figure out how to attach the reinforcement without embedding it inside the concrete. For this, it was decided to use two angles anchored to the bottom of the beam (Fig. 2.6). Two anchors were used for each angle to increase its rigidity and eliminate rotation of the angles around the anchor rods. Then reinforcements were passed through these angles and were attached to the ends of the beams. Nitinol or conventional steel rods were attached to the angle at a distance of 2.5 inches (76 mm) measured from the bottom of the beam to the center of the rod. These rods were threaded at the ends and attached by Gr. 80 high strength nuts and washers. No further reinforcements were used in the 6-inch (152 mm) mid-section. Longitudinal reinforcements outside the mid-section were placed at a distance of 4.5 inches (114.3 mm) measured from the bottom of the beam to the center of the rod. The reinforcement of the outer-section was deeper than mid-reinforcement in order to increase nominal moment capacity of the outer-section beam parts. The nominal moment capacity of the outer-section was twice the nominal moment capacity of the mid-section.

External Grade B-7 (Table 2.3) all threaded steel was used for longitudinal reinforcement at the outer-section. Gr. B-7 steel has higher yield strength than conventional Gr. 60 steel. The advantage of using Gr. B-7 over Gr. 60 steel was that the steel area would be minimized and the rods are already threaded. First of all, this meant less congestion of reinforcement in the beam. Second, this allowed an easier setup of experimental tests since rods can be anchored to the angles and the end of beams using nuts and washers. Furthermore, the hardware could be reused.

For the ends of the beams, initial plan was to use end plates anchored to the beam with longitudinal reinforcement attached to these plates by nuts as shown in (Fig. 2-12). Analysis of the anchor rods showed that their pull out strength is not sufficient and the connection would fail. Another anchorage method was proposed, analyzed and used for the

beam-ends. The beam-ends were made deeper with 2 prefabricated holes along the longitudinal axis of the beam, 10.5 inches (266.7 mm) deep, measured from the top of the beam to center of the holes. The outer-section steel rods went through the holes in the beam-end, and then were anchored to the angles with nuts and washers. Similarly, the steel rods were anchored to the beam-ends by nuts with a bearing plate placed between the washers and concrete end of the beam as shown in (Fig. 2-8).

Analysis was made on the beam to find the shear and tensile forces applied on the anchors embedded in the beam. The anchor rods were then designed and 4-3/4 inch (121 mm) Grade B-7 steel anchor rods were used, 2 anchors in each group. Each of the angles was attached to each group of anchors. The anchor rods were embedded 5 inches (127 mm) in the concrete and were spaced at 1.25 inches (32 mm) from center of the anchors to edge of the beam (Fig. 2-7).

The angles were chosen to remain elastic and rigid during experimental testing. Rigidity was defined by having deflections on outer legs of the angles limited to one-hundredth (0.254 mm) of an inch during the maximum loading event of the beam. More deflections would affect the results of the strain gage reading of the mid-section reinforcement. A36 steel (Table 2-4) was used for the angles. Iterative finite element analysis using the Structural Analysis Program (SAP) was performed on the angles [32]. Analysis performed implied the use of a 1-inch thick (25.4 mm) leg angle that would have a maximum deflection of 0.00132 inches (0.033528 mm). An angle, L 8x 6x 1, was chosen because it was available. Finally, the angles were analyzed for shear and tensile stresses. Bearing plates placed at the beam-ends were then analyzed. Bearing plates were designed for concrete bearing strength. Plates chosen were grade A36 steel, 5 inches (127 mm) wide by 4.5 inches (114.3 mm) deep by 0.5 (12.7 mm) inches thick and were placed as shown in (Fig. 2-8).

The lower stubs at the beam-end regions were designed using the shear friction method specified by the ACI 318-02 code. Grade 60 conventional # 3 (F10 mm) steel was used as stirrups and longitudinal reinforcement in the beam. Single-legged stirrups were used and spaced at 2.25 inches (57.15 mm). Top compression longitudinal reinforcement was placed at a distance of 1.5 inches (38.1 mm) measured from the top of the beam to the center of bars. Bottom tension reinforcement was placed at 1.5 inches (38.1 mm) measured from bottom of beam to center of bars. This bar was saw-cut at mid span prior to testing to eliminate its contribution to resisting moments. Development length of reinforcement in beam-end region was accounted for. It was 8 inches (20.32 mm) long. Detailed drawings are shown in (Figs. 2-5 to 2-9).

2.5 Specified and Measured Material Properties and Fabrication

In the following sections, the specified and measured properties of concrete, Nitinol, and steel are described. Tables 2-3 and 2-4 present specified properties of Grade B-7 and Grade A36 (248), steel respectively. Tables 2-5 to 2-8 present the measured material properties. It is frequently common to have some differences between measured and specified material properties. Thus, it is essential to evaluate the differences for a better evaluation of expected experimental test results.

2.5.1 Reinforcement

Two types of reinforcing materials were used in the tests. The shape memory alloy (SMA) interaction with concrete was to be tested; in this case Nitinol (NiTi) was used. The second material was conventional Grade 60 (420) steel. It was used to establish reference cases.

Nitinol rods were used in the study. A total of 4 Nitinol rods were used in the testing (Fig. 2-26). These rods were cold drawn, thermally straightened to the superelastic condition; grit blasted, and with threaded ends. The Austenite start (A_s) temperature was 5 degrees Fahrenheit (–15 degrees Celsius). The NiTi rods were manufactured and supplied by Special Metals Corporation [8]. For chemical analysis of the material, refer to Figure 2-2. Two sizes of Nitinol rods were used. Two rods had a diameter of 0.500 inches (12.7 mm); the other two had a diameter of 0.375 inches (9.525 mm). All rods had the same chemical composition with the same length of 10 inches (25.4 mm). The rods were threaded at both ends with a thread length of 1 inch (25.4 mm). The threads used were UNC (coarse threads) with 13 threads per inch (5 threads per cm) for the 0.500-inch (12.7 mm) rod, and 16 threads per inch (6 threads per cm) for the 0.375-inch (9.525 mm) rods [26].

Initial tensile tests on Nitinol rods proved that threaded regions of the Nitinol rods were extremely sensitive to stress concentration. Failure occurred in threaded parts at much lower strains than anticipated failure strain of the material (Section 3.2). Thus, to prevent failure at threads, the section in the middle part of the rod was reduced by machining. The suggested reduction in the diameter of the Nitinol rods was to have a tensile area less than that of the threads. This allowed the monitoring of strain in the critical reduced section using strain gages, thus preventing failure in the threads that cannot be monitored. The 0.500-inch (12.7 mm) rods had a thread root diameter of 0.406 inches (10.3 mm) [26]. The diameter in the middle section was reduced from 0.500 inches (12.7 mm) to 0.375 inches (9.525 mm). The 0.375-inch (9.525 mm) rod had a thread root diameter of 0.298 inches (7.57 mm) [26]. The diameter of the middle segment of these rods was reduced to 0.25 inches (6.35 mm).

2.5.2 Cube Materials and Fabrication

2.5.2.1 Concrete

The concrete 28-day strength for the cubes was specified to be 4000 psi (27.6 MPa) with a maximum aggregate size of ¾ inches (19.05 mm) and a slump of 5 inches (127 mm). The high slump specified was to ensure workability. Three cylinder specimens were poured at the same time cubes were casted. The three cylinders were used for the 28-day compressive test. All specimens were tested in accordance with ASTM C39-86 [29]. The same compressive loading rate was applied on all specimens. The loading rate ranged between 60,000 and 70,000 pounds (266.7 and 311.2 KN) per minute in order to be consistent. The cylinder dimensions were 6 inches (152 mm) in diameter and 12 inches (305 mm) in length. Equivalent cube strength was found using Murdock [32] and Neville

[31] correction factors. Table 2-6 summarizes the test results. The average measured strength of 4800 psi (331. MPa) was used in theoretical calculations.

2.5.2.2 Cube Formwork and Fabrication

Cubes were built in the Bridge Structures Laboratory at the University of Nevada, Reno. Wooden forms were built using ¾ inch (19.05 mm) thick plywood. Plywood was cut into 14 long pieces and 35 small pieces. Each of the long pieces was about 40 inches (1.02 m) long. The short pieces were 6 inches (152 mm) long. Both were 6 inches (152 mm) wide. Holes, with diameters of 0.8125 inches (20.64 mm), were drilled in the long pieces at 6.75 inches (171.05 mm) on center (Fig. 2.21). The height of the holes was 3 inches (76 mm) measured from top of the long piece to the bottom of the hole (Fig. 2.21). In the short pieces, holes were drilled at 3 inches (76 mm), measured from bottom of the piece up to the top of the hole. Plastic pipes with internal diameters of $^{9}/_{16}$ inches (14.29 mm) and an outer diameter of $^{13}/_{16}$ inches (20.64 mm) were cut into pieces that would go through the drilled holes. They were fitted into the holes and all the pieces were then nailed to each other into the final form that would essentially be used to cast 6 cubes. Five of these forms were built in order to cast a total of 30 cubes (Fig. 2.19)

After the cubes were removed from the forms, two holes were drilled on the sides of the cube. The holes were located vertically above each other at ½ inch (12.7 mm) away from the edge of the cube to the center of the hole. The holes were vertically distanced from each other at 1½ inches (38.1 mm) centered and were 1 inch (25.4 mm) deep. The holes were then filled with epoxy and two nails were inserted. Laser reflector markings were placed on the nails. These markings could not be placed on the face of concrete because the corners and edges of concrete were not confined and would spall taking out the markings with them.

2.5.2.3 Mild Steel

All mild steel was specified to be Grade 60. Two, 16-inch (177.4 mm) long bars from both #3 (F10 mm) and #4 (F13 mm) bars were tested in tension in order to determine thie material properties. The bars were tested in a Tinius-olsen mechanical testing machine. The elongation was measured using a dial gage over a 2-inch (50.8 mm) gage length. The samples were tested to failure. The same type of mild steel was used in cube and beam tests. Tables 2-7 and 2-8 summarize the measured properties of the tested bars. Figures 2-13 and 2-14 show the measured stress-strain relationship for #4 (F13 mm) and #3 (F10 mm) bars.

2.5.2.4 Steel Plates and Pipes

Grade A36 Steel was specified for the 4-inch (10.16 mm) and 3-inch (76 mm) square plates, and the 2-½ inch (63.5 mm) pipes. The thickness of the square plates was ½ inch (12.7 mm). The pipes were 0.75 inches (19.05 mm) long with an inside diameter of

2.47 inches (62.74 mm) and an outside diameter of 2.875 inches (73.03 mm). Small slots were cut in the edge of the pipes to give space for passing the strain gage wires from inside the pipe to the outside to be connected to the data acquisition. Slot dimension were ¾" x ¼" (19.05 mm x 6.35 mm) (Fig. 2-23).

2.5.3 Beam Materials and Fabrication

2.5.3.1 Concrete

The concrete 28-day compressive strength for the beams was specified to be 4000 psi (27.6 MPa) with a maximum aggregate size of ¾ inches (19.05 mm) and a slump of 5 inches (127 mm). The high slump specified was to ensure proper distribution of concrete with no voids in the specimens considering the small size of form. Nine standard cylinder specimens were poured at the same time the beam concrete was poured. The 9 cylinders were distributed into 3 groups. Each group was used for one of the 7-day, 14-day, and 28-day compressive test. All specimens were tested in accordance with ASTM C39-86 [29]. The same compressive loading rate was applied on all specimens. The loading rate ranged between 60,000 and 70,000 pounds (266.7 and 311.1 KN) per minute in order to be consistent. Table 2-5 summarizes the test results. The average measured strength of 5800 psi (40 MPa) was used in theoretical calculations.

2.5.3.2 Angles

The angles that were used had specified Grade A36 steel. The angle size used was L8x6x1. Two groups of a total of four angles were used for the beam tests. Each group had a total of two identical angles. The only difference existing between the two groups was the hole locations. Each group was used for a different type of testing. One of the groups was used for testing the beams with a single bar reinforcement right at the mid-section of the beam. The other group was used for testing the beams with double bar reinforcement. The group of angles used for single reinforcement had five drilled holes in them (Fig. 2.17, 2.18). Two of the holes were in the 8-inch (20.32 mm) leg. These holes were used to attach the $^{3}/_{4}$ inch (19.05 mm) diameter anchor rods to the angles. The centers of the holes were located 2.5 inches from the edge of 8-inch (20.32 mm) leg. The diameter of the holes used was $^{7}/_{8}$ of an inch (22.25 mm). The extra $^{1}/_{8}$ inch (3.18 mm) was added to the size of all holes to account for human errors such as misplacement of anchor rods during the casting of the specimen. There are three drilled holes in the 6-inch (152 mm) leg. One of the holes was used to anchor the mid-section reinforcement to it. The location of the center of the hole was in the middle of the 6-inch (152 mm) leg at 3.5 inches (88.7 mm) from the edge. The diameter of the hole was $^{5}/_{8}$ of an inch (9.54 mm). The other two holes were used to anchor outer-section reinforcements to it. The locations of the centers of the holes were at 1.5 inches (38.1 mm) from the edge of the 6-inch (152 mm) leg. The diameters of these two holes were $^{5}/_{8}$ inch (9.525 mm). Minimum spacing and clearances of holes were

designed according to the AISC – LRFD, volumes 1 and 2 [26,27]. Refer to figs. 2-17 and 2-18 for drawing details of the angles.

The group of angles used for double reinforcement had six holes drilled in them (Figs. 2.15, 2.16). All holes had similar properties and locations as the other group of angles except for the holes used in mid-section reinforcements. In this group, two holes were used for mid-section reinforcements. Their centers were located at a distance of 3.5 inches (88.7 mm) from the edge of the 6-inch leg (152 mm). The spacing between the holes was 3 inches and their diameters were $^5/_8$ of an inch (9.525 mm).

2.6 Instrumentation

2.6.1 Introduction

The basic instrumentation consisted of strain gages to measure strains in reinforcements, transducers to measure concrete deformation, a laser to measure vertical deflections, and load cells to measure forces. The placement and exact use of instrumentations varied from the cube and beam experimental testing. Differences are described in detail in the following sections.

2.6.2 Data Acquisition Equipment

Data were collected from the experimental tests using a National Instrument control unit. This system has a maximum sampling rate of 2 Hz. Analog filters were set up at 4 Hz. Analog output was available for on-line monitoring or control of any selected input parameter. Strain gages, displacement transducers, laser, and load cells were connected to screw terminal blocks. For a list of instruments used, refer to Table 2-9.

2.6.3 Strain Gages

Strain gages used were the post yield YF-series provided by Texas Measurements inc. [30]. The specific type that was used is the YFLA-2. They have large strain measurement capacity, which could reach up to 200,000 micro-strains at room temperature. The YFLA-2 strain gage has a small backing size that enabled their adhesion to small surfaces such as the $^3/_8$ of an inch (9.525 mm) diameter NiTi bar. It has a backing length of 0.295 inches (7.49 mm) and a backing width of 0.157 inches (3.99 mm). The CN-Y compatible adhesive was used with the strain gages.

2.6.4 Load cells

Two kinds of load cells were used in experimental tests. One was the Lebow 150 kip load cell with a capacity of 150 Kips (667 KN) and the other was the Transducer Technique LWO-20 with a capacity of 20 Kips (88.9 KN). The Lebow load cell was used

to measure the vertical loading on both beams and cubes. The Transducer Technique load cell was used to measure forces in the bars used to confine the cubes.

2.6.5 Displacement Transducers

One kind of linear displacement transducer was used in the beam experimental testing. It was used to obtain data for drawing the strain profile and curvature of the beam. The manufacturer is Novotechnik and the type is TR-50 Linear Displacement Transducers.

2.6.6 Laser Device

A laser device was used to measure vertical deflections and deformations in many different applications. Data were collected from the laser extensometer by connecting it to the data acquisition. The laser extensometer had a measurement range of 0.2 inches (5.08 mm) up to 5.0 inches (127 mm). It has a resolution of 0.0001 inches (0.00254 mm). It measured deflection or deformation by scanning the specimen and detecting the location of reflective tape markings. As the marks move during the test, the laser tracks and records their exact position. The manufacturer of the laser extensometer used is Mechanical Testing and Simulation (MTS) and the type used is LX 500.

2.7 Test Procedure

2.7.1 General

All tests presented were done at the Bridge Structures Laboratory at the University of Nevada, Reno. The cube specimens were subjected to vertical compressive load and the beams were subjected to two vertical point loads, 6 inches (152 mm) apart at the middle top of the beam. Beam specimens were painted with white lime in order to detect crack propagation. Cracks were marked in each test in order to monitor flexural crack growth.

2.7.2 Tensile Tests

Tensile tests were done using the Instron and Tinius-olsen testing machine. The tensile tests conducted were done to measure physical properties of the steel and Nitinol to be used in experimental testing.

Sixteen-inch (406 mm) long steel specimen samples were used for measuring steel material properties. The specimens were placed vertically and were held in position with steel grips. Tensile loads were then applied, monitored, and recorded up until failure of specimen. The vertical elongation was measured using a dial gage over a 2-inch (50.75 mm) gage length. Strains were recorded by taking readings from the dial gage at 500 pound (2.2 KN) increments. Data were plotted and properties were tabulated. Tables 2-7 and 2-8 summarize the measured properties of the tested bars. Figures 2-13 and 2-14 show graphs of measured stress-strain relationship for #4 (F13 mm) and #3 (F10 mm) bars.

No samples were available for testing Nitinol in order to determine its properties. Therefore, the Nitinol bars that were used in experimental testing were also used to perform tensile tests. In this case, tensile tests were not performed until failure. They were stopped slightly after yielding. This was sufficient to obtain the flag-shape stress-strain relationship that would show upper, and lower plateau yield stresses. Table 2-10 summarizes the measured properties of the tested bars. Figures 2-24 and 2-25 show graphs of measured stress-strain relationship for both, the 0.50-inch (12.7 mm) bar, and the 0.375-inch (9.525 mm) bar.

2.7.3 Cubes

The cubes were tested in a Satec compression machine. Four strain gages were placed on each of the bars used in the experimental test. The strain gages were placed at 90 degree spacing, circumferentially around the bar, at approximately 1.5 inches (38.1 mm) from its end. The bars were then placed in the prefabricated holes in the cube. The 4-inch (10.16 mm) plates, steel pipes, and the 3-inch (63.5 mm) plates were then attached to the rods with nuts and washers. The small washer load cells were then placed in between the washers and the steel plate to measure stresses in the bars. The Lebow 150-kip (666.8 KN) load cell was placed on the top face of the cube right under the compression arm of the machine. Two laser reflector markings were then placed on the nails that were embedded in the sides of the cubes. Laser extensometer was placed on the tripod and targeted towards the markings. Strain gages, laser, and load cells were then connected to the data acquisition system.

Two different types of test methods were conducted on the cubes: Monotonic loading and cyclic loading. The laser, gage, and load cell readings were monitored from the screen of the computer attached to the data acquisition. The loading of the specimen took place until the failure of the concrete and a significant drop in load was visible.

2.7.4 Beams

The beams were tested in a Reihle machine (Figs. 2.10 and 2.11). Four strain gages were placed on each bar. The strain gages were placed at 90 degree spacing, circumferentially around the bar, at the longitudinal center of it. The bars were attached to the angles, and all necessary bearing plates were placed in position. The load cell was placed between the top of the two-point load and the loading plate of the Reihle machine. Two Tr-50 Novotechnik linear displacement transducers were placed on the face of the beam at mid-region. The tips of the transducers were placed six inches apart at the same location as the point loads. One transducer was placed at a distance of $^5/_8$ in. (9.525 mm) from the top of the beam; the other was placed at a distance of 1 inch (25.4 mm) from the bottom of the beam. All instruments were connected to the data acquisition. The laser extensometer was placed on the other side of the beam. A laser device was used to measure maximum deflections at the middle of the beam.

The beams were tested under half-cycle loads. The laser, gage, and load cell readings were monitored from the screen of the computer attached to the data acquisition.

Load cycles had increments of approximately half measured yield displacement. Theoretical half yield loads, and yield loads were calculated before test. Beams were then loaded up to half yield load and then unloaded to 0.3 kips (1.33 KN). The 0.3 kip-load was left to keep the system stable. After that the beam was loaded carefully to the yield load. The load-displacement graph was monitored on the computer screen that was connected to the data acquisition. Based on the measured yielding of the beam that was visible from the computer graph, the applied displacement amplitude was selected. The yield displacement was then measured graphically. Cyclic loads with half yield load increments were then applied to the beam. Consistent loading and unloading rates were used on all beams.

CHAPTER 3: Test Results

3.1 Introduction

This chapter presents the measured data and the observed behavior of the beam specimens and the concrete cubes. The experimental work also included in developing anchorage details for Nitinol wires wrapped around concrete cylinders. This chapter also describes this anchorage method and its evaluation.

3.2 Tensile Tests

Tensile tests were performed on Nitinol and mild steel to find their properties. Experimental results were discussed in Section 2.5.2.3 and 2.7.2. Unlike the steel bars, problems were encountered with the strain gages placed on the Nitinol rods. Initially, four strain gages were placed on each rod circumferentially at 90 degree spacing as discussed in Chapter Two by using the conventional method. That is, smoothening the surface with sand paper followed by thorough cleaning with acid and then base solutions. Bars were left to dry and then CN-Y adhesive was placed on the surface of the strain gage. The strain gage was then placed on the desired location on the surface of the bar and then pressed firmly for ten to fifteen minutes. The process was repeated until all strain gages were placed in their appropriate locations. This process worked well with the NiTi rods when used in cube tests but in beam testing, an unexpected phenomenon was observed. This phenomenon was first observed in BNH1. As soon as the bars reached yielding and the load was released, load-strain plots being monitored during the test showed a sudden drop in strains. By the time load was reduced down to 0.3 kips (1.3 KN); the strain gages were showing significant compression in the bars. The beam was reloaded to yield and unloaded again, and the same phenomenon was observed. The second time, strain readings showed even higher compressive strains.

The CN-Y adhesive was not functioning properly. Slippage was occurring between the strain gages and the surface of the bars. Direct tensile tests were performed on the Nitinol bars to observe if this would happen again. This time all four bars were tested. The bars were loaded to significantly high strains of approximately 40,000 microstrains. This strain would be similar to that achieved by the bars during the beam tests. Same observation was made on most of the strain gages on the four bars. Slippage occurred after bars started to yield.

It took one to two minutes for the adhesive to dry on the steel bars and ten to fifteen minutes to dry on the Nitinol bars. It appeared that slippage was perhaps due to the fact that the strain gages needed to be held while being pressed for a longer time. Another method was proposed and tested. Instead of holding the gages for ten to fifteen minutes, the gages were firmly wrapped by electrical insulating tape. This implied that the gages would be left under pressure for a long time thus giving the adhesive sufficient time to dry. More space was needed to be able to tape the gages. Gages had to be staggered along the middle of the bar (Fig. 3.1).

A new method was tested in tension in conjunction with laser extensometer to verify the strain gage readings. All strain gage and laser extensometer readings on the four bars were consistent. Bars were used in beam tests and were proved to work properly.

3.3 Nitinol Wire Anchorage Method

Nitinol (NiTi) cannot be welded to itself or any other form of steel using current technology. To use NiTi, wires were needed as external confinement reinforcement for concrete. It would not be possible to connect it by conventional methods. An anchorage method was designed and experimentally tested as a part of the current study (Figs. 3.2-3.6). A rectangular steel plate curved to match the surface of a 6-inch (150 mm) diameter concrete cylinder with two predrilled holes was used (Fig. 3.2-3.3). A 2-inch (50.8 mm) slice of the concrete cylinder was saw cut. Two holes were drilled in the standard cylindrical concrete slice specimen going through it from one side to the other. The holes were 1.5 inches (38.1 mm) apart. The steel plate was bent in order to have a radius of curvature equal to that of the concrete cylindrical specimen. The two holes were filled with epoxy by pressure injection. After that, NiTi wire with a diameter of 0.1 inches (2.54 mm) was squeezed through one of the epoxy filled concrete holes, and into one of the holes of the plate, back into the second plate hole and through the second epoxy filled concrete hole, simultaneously applying epoxy around the wire to ensure proper distribution around it (Fig. 3.4-3.5). A pullout test was performed on the wire (Fig. 3-6). The wire was pulled until failure. The wire failed in the region outside the holes and the steel plate region. Such a failure implied that no high stress concentrations existed in the region were the wire was bent at the steel plate. Adhesion forces between the epoxy and the NiTi wires were sufficient to transfer forces to steel plate region. This meant that the anchorage mechanism performed well.

3.4 Cube Specimens

Three unconfined and eight confined cubes were tested under vertical loads (Section 2.7.3). The cubes had 6 inch (152.4 mm) side dimension. The confined cubes were divided into two groups. Group 1 had four cubes confined with Nitinol (NiTi) bars. Two cubes were confined with 0.25-inch (6.35 mm) NiTi bars; the remaining two cubes were confined with 0.375-inch (9.5 mm) NiTi bars. Group 2 had four cubes confined with conventional steel bars. Two cubes were confined with #3 (F10) steel bars whereas the other two cubes were confined with #4 (F13) bars. Tests were conducted to determine the effect of confining concrete in comparison with conventional steel. Displacement recovery of the cubes and strain recovery of NiTi bars were monitored under cyclic loads. The specimen designations were C-N-L-1, C-N-L-2, C-N-H-1, C-N-H-2, C-S-L-1, C-S-L-2, C-S-H-1, and C-S-H-2. The letter C is short for cube, the letter N or S is short for Nitinol or steel respectively, the letter L or H is short for low or high respectively, and the number 1 or 2 denotes the specimen number in its category. Low and high are used to point to the 0.375-inch (9.525 mm) and 0.5-inch (12.7 mm) diameter bars respectively. Specimen C-S-

H-2 results are not presented because the test was not completed due to problems encountered during experimental procedure.

3.4.1 Load - Displacement Results

Vertical load vs. displacement curves were studied to determine the confinement effects of Nitinol (NiTi) compared to conventional steel. Three factors were of particular interest. The ultimate load, ultimate displacement and the residual displacement of the specimens. Loads and displacements were normalized with respect to the highest recorded values for each respectively. Ultimate loads reached by NiTi confined cubes were significantly lower than those confined by conventional steel (Table 3.1)(Figs. 3.7 -3.13). Taking the average of the ultimate loads reached by C-N specimens would give 136 kips (603 KN), which is significantly lower that those of C-S specimens that gave a value of 186 Kips (829 KN) (Table 3.2). Residual displacements were monitored to see if superelastic behavior of NiTi would result in more displacement recovery than that of steel. Normalizing the residual displacements of the specimens showed that those of NiTi and steel confined cubes had the same results (Table 3.1)(Figs. 3.14-3.20). Taking the average percent residual displacement of C-N specimens and those of the C-S specimens would give 79% for both groups (Table 3.2). Further analysis of analytical versus measured stress-strain relationship will be discussed in Chapter 4.

3.4.2 Load - Bar Strain Results

Load vs. average bar strains curves (Figs. 3.21-3.27) showed similar results as load-displacement curves. Lateral residual strain for both C-N and C-S specimens were similar (Table 3.1). The average of the residual strains recorded for the C-N specimens was 0.90, whereas the average of the C-S specimens recorded was 0.88 (Table 3.2).

3.4.3 Appearance of Cubes after Failure

Confined cubes had common features after failure. They all had approximately the same concrete spalling affected area all around their corners. Cubes were confined with 4-inch (101.6 mm) square steel plates. The cubes had a dimension of 6 inches (152.4 mm). Concrete crushing and spalling of the corners were occurring at the unconfined region. Looking at the plan view of the tested cubes, triangular concrete spalling is visible at the four corners (Figs. 3.28-3.29). They are approximately 1 inch (25.4 mm) long measured from the corners. The elevation of the cube shows the same phenomenon occurring along all edges of the cubes. As loads increased on cubes during early stages of tests, spalling of concrete would be visible at the edges of the cubes (Fig. 3.30). As cyclic loads are applied to the cube until failure, extensive crushing and spalling of concrete edges would be very clear (Fig. 3.31-3.33).

3.5 Beam Specimens

The beams were tested under half-cycle loads. The laser, gage, and load cell readings were monitored from the screen of the computer attached to the data acquisition. Load cycles had increments of approximately half measured yield displacement. Theoretical half yield loads, and yield loads were calculated before test. Beams were then loaded up to half yield load and then unloaded to 0.3 kips (1.33 KN). The 0.3 kip-load was left to keep the system stable. After that the beam was loaded carefully to the yield load. The load-displacement graph was monitored on the computer screen that was connected to the data acquisition. Based on the measured yielding of the beam that was visible from the computer graph, the applied displacement amplitude was selected. The yield displacement was then measured graphically. Cyclic loads with half yield load increments were then applied to the beam. Consistent loading and unloading rates were used on all beams. The beam specimens are B-N-L-1, B-N-H-1, B-N-L-2, B-N-H-2, B-S-L-1, B-S-H-1, B-S-L-2, and B-S-H-2. The letter B is short for beam, the letters N/S are short for Nitinol/steel respectively, the letters L/H are short for low/high respectively, and the number 1/2 denotes the number of bars used as longitudinal reinforcement at mid-section. Low and high are used to point to the 0.375-inch (9.53 mm) and 0.5-inch (12.7 mm) NiTi bars respectively.

3.5.1 Cracking Behavior

All beams had a two-inch saw cut in the mid-span (Fig. 3-41). This cut, as discussed in the previous chapter, was made to cut the bottom longitudinal steel reinforcement in the beam. This was done to have better control on the testing procedure by excluding the effect of the longitudinal reinforcements that was embedded in the concrete at the time of casting. Essentially, the only active tensile longitudinal reinforcement in the beam would be the ones attached to the anchored angles.

All beam specimens with doubly reinforced longitudinal bars at midsection, except for BNL2, had one bar yield before the other during experimental testing. Before experimental testing, bar strains were monitored while tightening the nuts on the middle reinforcements in order of achieving similar strains in both bars prior to testing. This method still did not prevent the premature yielding of one bar with respect to the other after loading the specimens. This is explained by the possible dissymmetry of the beam cross-section. The dissymmetry of the cross-section caused the longitudinal reinforcements to have different depths from center of bars to the extreme compression fiber of the beam. This in turn caused different stress distributions in the bars during loading, which in turn caused deeper reinforcement to yield before the other. Such a behavior had an affect on the cracking behavior of the specimens. The first was the cracking behavior observed from both faces of the beams. The side parallel and closer to the bar that yielded first would have more extensive cracking than the other face of the beam. Figures shown in this section represent the sides with the more extensive cracks.

3.5.1.1 BNL1

BNL1 had no visible cracks prior to loading (Fig. 3-41). As loading began, minor flexural cracks were observed at reasonably low loads (Fig. 3-42). Cracks would propagate starting from the top of the cut in the bottom of the beam located at mid-span. Flexural cracks at anchor rod regions would follow at loads close to yield loads (Fig. 3-43). BNL1 was not loaded untill failure.

3.5.1.2 BNL2

BNL2 had no visible cracks prior to loading (Fig. 3-44). As loading began, minor flexural cracks were observed at reasonably low loads (Fig. 3-45). Cracks would propagate starting from the top of the cut in the bottom of the beam located at mid-span. Flexural cracks at anchor rod regions would follow up at loads close to yield loads (Fig. 3-46). BNL2 was not loaded till failure. Cracking behavior was similar to BNL1.

3.5.1.3 BNH1

BNH1 had minor visible flexural cracks prior to loading (Fig. 3-47). As loading began, minor flexural cracks were observed at reasonably low loads at midspan and anchor rod regions. Midspan cracks propagated starting from the top of the cut in the bottom of the beam located at mid-span (Fig. 3-48, 3-49). Cracks at anchor rod region propagated from above the anchor rods (Fig. 3-48, 3-49). Horizontal cracks at the top of the beam at midspan appeared at load cycles higher than yield indicating near crushing failure of concrete (Fig. 3-41, 3-49). BNH1 was not loaded till failure. Final crack propagation was similar to BNL1 and BNL2 but more extensive.

3.5.1.4 BNH2

BNH2 had visible flexural cracks prior to loading at anchor rod regions (Fig. 3-50). As loading began, minor flexural cracks were observed at reasonably low loads at midspan and anchor rod regions. Midspan cracks propagated starting from the top of the cut in the bottom of the beam located at mid-span (Fig. 3-51). Cracks at the anchor rod region propagated from above the anchor rods (Fig. 3-51). Horizontal cracks at the top of the beam at midspan appeared at load cycles higher than yield indicating near crushing failure of concrete (Fig. 3-51). BNH2 was loaded till failure. BNH2 failure mechanism was crushing of concrete at midspan (Fig.3-52). Crack propagation was similar to BNH1.

3.5.1.5 BSL1

BSL1 was first tested before it had the saw cut at midspan (Fig. 3-53). Therefore, cracks marked on the beam were different than other beam specimens. Unlike other beam specimens, BSL1 had flexural cracks propagating from locations under point loads from the bottom of the beam, above the anchor rods and at corners, where 12-inch (304.8 mm)

deep ends of beam intersect the middle 6-inch (152.4 mm) deep middle area (Fig. 3-54). BSL1 was tested again after getting a saw cut. Final cracks did not change and remained the same after final load cycle (Fig. 3-55). Beam was not loaded till failure.

3.5.1.6 BSL2

BSL2 had no visible cracks prior to loading (Fig. 3-56). As loading began, minor flexural cracks were observed at reasonably low loads at midspan and anchor rod regions. Midspan cracks propagated starting from the top of the cut in the bottom of the beam located at mid-span (Fig. 3-57). Shear and flexural cracks at the anchor rod region propagated from above the anchor rods at loads approaching yield (Fig. 3-57). Horizontal cracks at the top of the beam at midspan appeared at load cycles higher than yield indicating near crushing failure of concrete (Fig. 3-58). BSL2 was not loaded till failure. BSL2 had extensive shear and flexural cracks at the anchor rod regions with lower flexural cracks at midspan when comparing them to each other. BSL2 had crack propagation very much different than BN and BSL1 specimens.

3.5.1.7 BSH1

BSH1 had no cracks prior to loading (Fig. 3-59). As loading began, minor flexural cracks were observed at reasonably low loads at midspan and anchor rod regions. Midspan cracks propagated starting from the top of the cut in the bottom of the beam located at mid-span (Fig. 3-60). Cracks at anchor rod region propagated form above the anchor rods (Fig. 3-60). Horizontal cracks at top of beam at midspan appeared at load cycles higher than yield indicating near crushing failure of concrete (Fig. 3-61). BSH1 was loaded till failure. BSH1 failure mechanism was crushing of concrete at midspan (Fig.3-61). Crack propagation was similar to BN and BSL1 specimens.

3.5.1.8 BSH2

BSH2 had visible a flexural crack prior to loading at on anchor rod region (Fig. 3-62). As loading began, minor flexural cracks were observed at reasonably low loads at midspan and anchor rod regions. Midspan cracks propagated starting from the top of the cut in the bottom of the beam located at mid-span at a lower rate than at anchor rod regions (Fig. 3-63). Shear and flexural cracks at anchor rod region propagated from above the anchor rods at loads approaching yield with a high rate (Fig. 3-63). Horizontal cracks at top of the beam at midspan appeared at load cycles higher than yield, indicating near crushing failure of concrete but then stopped while cracks at anchor rods increased extensively (Fig. 3-64). BSH2 was loaded till failure. BSH2 had a failure mechanism of a shear-flexural failure at one of the anchor rod locations. BSH2 had extensive shear and flexural cracks at the anchor rod regions with lower flexural cracks at midspan when comparing them to each other. BSH2 had crack propagation very much similar to BSL2.

3.5.1.9 Summary

In general, B-N specimens had higher residual cracks than B-S specimens (Table 3-3). Residual cracks for the beam specimens were not all recorded. This was due to extensive cracks taking place in regions other than at midspan and thus affecting the crack width at midspan. Unrecorded residual cracks were marked by "N.R" in table 3-3. This data is not consistent with residual displacement data, which shows the exact opposite. Measured residual displacements in B-N specimens were significantly lower than residual displacements in B-S specimens. Reasons for inconsistent results between residual cracks and residual displacements are discussed in Section 4.3.

3.5.2 Measured Data for Beam Specimens

In this section, the Nitinol superelastic behavior together with the load - displacement, ductility, stiffness properties and moment - curvature results are going to be discussed.

3.5.2.1 Load – Displacement Results

As mentioned before in chapter 2, a laser extensometer was used to measure deflections and a load cell was used to measure loads. Displacement recovery in B-N specimens was significantly higher than that achieved by B-S specimens (Table 3-5). Detailed analysis of calculated and measured load-displacement data will be discussed in Chapter 4.

The average residual deformation in the B-N specimens was equal to 0.091 whereas that of the B-S specimens was equal to 0.449 (Table 3.6) (Figs. 3.65-3.72). Normalizing load – displacement results for each specimen with respect to the highest loads and displacements achieved by each respectively, and plotting them show significant residual deformation difference between the B-N and B-S specimens (Figs.3.73-3.80).

Specimens B-N-H and B-S-L had the same longitudinal reinforcements at mid-section except that one had NiTi as longitudinal reinforcements and the other had conventional steel reinforcements. Residual displacement comparisons made between those two groups would give a clear understanding of the advantages of using NiTi as longitudinal reinforcement over conventional steel. Specimens B-N-H-1 and B-S-L-1 had a residual deformation of 0.01179 inches (0.3 mm) and 0.0466 inches (1.18 mm) respectively, which is a significant difference with a ratio of 1 to 4 (Figs. 3.65, 3.67). Specimens B-N-H-2 and B-S-L-2 had a residual deformation of 0.03 inches (0.77 mm) and 0.31 inches (7.83 mm) respectively, which is a significant difference with a ratio of 1 to 10 (Figs. 3.66, 3.68).

The ratios of residual displacement to maximum displacement for beam specimens were studied (Table 3.7). B-N specimens had a significantly lower ratio. Specimens B-N-H and B-S-L had the same reinforcement ratio. Comparing these specimens to each other show a significant difference. The ratio of the average of residual displacement to maximum displacement for B-N-H to B-S-L was 0.054 (Table 3.7). The ratio of the

average of residual displacement to maximum displacement for B-N to B-S specimens was 0.2016 (Table 3.7).

3.5.2.2 Nitinol Pseudo-Elastic Behavior

All Nitinol (NiTi) bars showed pseudo-elastic behavior when used as a longitudinal reinforcement in the beam specimens. Bars almost fully recovered deformation without any residual strains even after yielding (Fig.3.81-3.87). The graph of B-N-H-1 was not shown because of the strain gage failure as discussed in section 3.2. Specimens B-N-H-2 and B-S-L-2 had the same amount of reinforcement at mid-section. The average residual strain in specimen B-N-H-2 is 0.004, whereas the average residual strain in specimen B-S-L-2 is 0.017 (Figs. 3-85, 3-87). This meant that B-S-L-2 had an average residual strain 4.25 times higher than that of B-N-H-2.

3.5.2.3 Ductility

Test results did not clearly show the effective yield loads of the specimens. These loads were needed to calculate beam ductilities. A consistent method was developed for use on all specimens to capture the yield loads. To facilitate the process, deflections were first converted to drift. Drift was defined to be the ratio of displacement at midspan to half the span length. On the load - drift plots; a line parallel to the initial tangent of the graph was drawn with an offset of 0.05% drift. The intersection of this line and the graph was assumed to be the effective yield point (Fig. 3-88, 3-89). Table 3.3 summarizes the measured effective yield loads for all specimens. Detailed analysis of analytical versus measured ductility data will be discussed in Chapter4.

After yield loads were determined, displacement ductilities for all specimens were found (Table 3.3). Lowest displacement ductility achieved was for specimen B-N-L-1. Specimen B-S-L-2 achieved the highest displacement ductility. Ultimate displacement ductilities were found for specimens B-N-H-2, B-S-H-1, and B-S-H-2, since they were the only beams to fail. All had very similar ultimate displacement ductilities of approximately 2.

3.5.2.4 Stiffness Properties

Measured initial tangent stiffness and effective pre-yield stiffness of B-N and B-S specimens were compared (Table 3-4). The effective pre-yield stiffness was taken as the ratio of the yield load to yield displacement. The yield displacement was determined using drift-offset method discussed in Section 3.5.2.3. The stiffness of B-N specimens was relatively lower than those of the B-S specimens. Specimens B-N-H and B-S-L had the same amount of reinforcement. The ratio of the measured initial tangent stiffness of B-N-H to that of B-S-L specimens is 0.61, whereas the ratio of the effective pre-yield stiffness of B-N-H to that of B-S-L specimens is 0.64 (Table 3-4). This shows that reinforcing beams with Nitinol significantly affects beam stiffness although Nitinol reinforcement was limited to a small region of the beam that was 6 inches (152.4 mm) long with a beam span

of 50 inches (1270 mm). This can be explained by the lower modulus of elasticity of the Nitinol when compared to that of steel (Tables 2.7, 2.8, 2.10). Detailed analysis of analytical versus measured stiffness properties of beams will be discussed in Chapter 4.

3.5.2.5 Moment – Curvature Results

Two transducers were placed on the beam at mid-span parallel to the longitudinal axis of the beam. Each transducer was 6 inches (152.4 mm) long and was placed right under the two point load locations. One was placed at a distance of 0.5 inches (12.7 mm) from top of the beam while the other was placed at a distance of 5 inches (127 mm) from top of the beam. The data recorded by the top transducer resembled compression in beam, which were transformed into compressive strains. The data recorded by the bottom transducer resembled tension in the beam, which were transformed into tensile strains. Using the calculated strains from measured data, the depth of the neutral axis was determined at each given load. For each measured load, curvature was found from the ratio of concrete compressive strain to the depth of neutral axis. Loads were then transformed into moments and the measured moment – curvature results were plotted for each beam (Figs.3.90 –3.97).

Measured moment - curvature graphs (Figs. 3.90-3.97) demonstrated significant curvature recovery in all B-N specimens compared to the B-S specimens (Table 3.5). Specimen B-N-H-2 (Fig. 3-91) recorded the lowest normalized residual curvature of zero whereas specimen B-S-L-2 (Fig. 3-93) recorded the highest residual curvature of 0.630. The ratio of the average of normalized residual curvatures for B-N specimens to that of B-S specimens is about 1 to 2. B-N specimens recorded an average equal to 0.287 whereas the B-S specimens recorded an average equal to 0.524 (Table 3.5).

Specimens B-N-H and B-S-L had the same longitudinal reinforcements at mid-section except that one had NiTi as longitudinal reinforcements and the other had conventional steel reinforcements. Residual curvature comparisons made between those two groups would give a clear understanding to the advantages of using NiTi as longitudinal reinforcement over conventional steel. Specimens B-N-H-1 and B-S-L-1 had a residual curvature of 0.000169 rad/in (0.0046 rad/m) and 0.0006541rad/in (0.02575 rad/m) respectively, which is a significant difference with a ratio of approximately 1 to 4 (Figs. 3-90, 3-92). Specimens B-N-H-2 and B-S-L-2 had a residual curvature of 0 and 0.00565 rad/in (0.0222 rad/m) respectively, which is a significantly large difference (Figs. 3-91, 3-93).

CHAPTER 4: Analysis of Test Results

4.1 Introduction

This Chapter compares test results presented in Chapter 3 to theoretical calculations. Comparison between theoretical and measured confinement properties will be discussed. Measured stiffness, ductilities, and load-displacement relationships will be compared to theoretical results. Finally, a theoretical load-displacement analysis of four full-scale beams will be studied and compared.

4.2 Comparison of Measured Confinement Properties

Measured confined stress–strain results were compared with the results of Mander's confinement model [34]. Mander's model was used because it is one of the most widely used models, even though this model is developed for steel confined concrete. Cube deflections from experimental results were not the actual concrete deflections. Deflections recorded were the relative displacement of the loading head of the Satec testing machine and the base of the machine. Reasons for using this method are discussed in detail in section 4.2.2. These deflections were higher than those of the actual concrete deflections due to machine deformation. Nonetheless, this deflection allowed for the evaluation of relative performance of confinement provided by steel versus Nitinol.

4.2.1 Measured Stress Calculations

Vertical stresses on cubes were calculated based on the observed confined area. The confined region was assumed to be a 5-inch (127 mm) square region in middle of the cube plan view for reasons discussed in Section 3.3.3 (Fig. 4-1). The confined area in the confined cube tests was assumed to be 25 in^2 (16,129 mm^2) whereas vertical stresses in unconfined cube tests were based on the whole surface area of the cube, 36 in^2 (23,226 mm^2). The assumption of the lower confined region was done for a fair evaluation between unconfined and confined concrete strength since unconfined corners in the cubes spalled at early stages of loading.

4.2.2 Measured Vertical Strain

Direct measurement of vertical deformations in the concrete cubes was unsuccessful. Laser reflector marks taped to the surface of the cubes fell off the face of the cube while testing due to the spalling of concrete. Nails embedded in concrete with laser reflector markings taped to their heads did not work because the nails rotated as concrete was compressed. Laser markings were then taped to the loading head and the base of the Satec testing machine. Deformations measured by laser extensometer were the relative displacement of the head to the base, not concrete cube deformation. Results obtained were significantly higher than real cube deformations due to the settlement that took place in the

machine head during the loading process and machine deformation. Nonetheless, such deflection measurements allowed comparison between C-S and C-N cubes.

4.2.3 Average Measured Confined Pressure

Washer load cells were initially used to measure confinement loads in each bar but did not give consistent results. A probable explanation for the inconsistency of the load measurements provided by the load cells is that it was caused by its extreme sensitivity to moments and torques caused by the twisting and bending of the bars when the cubes were loaded. Therefore, confinement pressures were calculated using another method that seems to be reasonable and fairly accurate. Strain gage readings during experimental tests showed that the NiTi and steel bars confining the cubes yielded. Therefore, the average measured confined pressure was calculated based on the yield loads for each of the NiTi/steel bars respectively. Nitinol and steel measured yield loads and strains were discussed in Chapter 2. Nitinol yield loads were calculated based on reduced bar section area. Steel yield loads were calculated based on the cross sectional areas of steel bars. The calculated yield loads were divided by the area of the 4-inch (101.6 mm) square steel plates that were used to confine the concrete cube. This resulted in finding the average measured confined pressure for the cubes (Table 4-1). Average confined pressure ranged from 178 psi (1.23 MPa) for C-N-L to 800 psi (5.52 MPa) for C-S-H.

4.2.4 Measured vs. Calculated Confined Properties

Theoretical confined concrete properties were calculated based on Mander's confinement equation [34]. Equations used were as the following:

$$f'_{cc} = f'_c \times \left(-1.254 + 2.254 \times \sqrt{1 + \frac{7.94 \times f'_l}{f'_c}} - 2 \times \frac{f'_l}{f'_c} \right)$$

Where,

f'_{cc} = Compressive strength of concrete confined by plates

f'_c = Unconfined concrete strength

f'_l = Average confinement stress

$$\varepsilon_{cc} = 0.002 \times \left[1 + 5 + \left(\frac{f'_{cc}}{f'_c} - 1 \right) \right] \qquad \varepsilon_{cu} = 0.004 + 1.4 \times \rho_s \times \frac{f_{yh} \times \varepsilon_{sm}}{f'_{cc}}$$

$$\rho_s = \frac{A_s}{A_p} \qquad f'_c = \frac{f'_{cc} \times X \times r}{r - 1 + X^r} \qquad X = \frac{\varepsilon_c}{\varepsilon'_{cc}}$$

$$E_c = 57{,}000 \times \sqrt{f'_c} \text{ (psi)} \qquad E_{sec} = \frac{f'_{cc}}{\varepsilon'_{cc}}$$

Where,

f_{yh} = Yield stress

ε_{cc} =Strain at stress of f'_{cc}

ε_{cu} = Ultimate compression strain at f'_{cu}

E_c = Modulus of elasticity of concrete

E_{sec} = Secant modulus of elasticity

The average of the measured results of each two similarly confined cubes was calculated (Tables 4-2 and 4-3). Measured and calculated compressive strengths were close to each other (Table 4-2). In most cases, the calculated compressive strengths were more conservative than the measured strengths except in the case of specimens CSL, which were slightly higher than the calculated values. Measured to calculated strength ratios for CNH, CNL, CSL and CSH respectively were 0.91, 0.79, 1.05 and 0.91 (Table 4-2). This means that Mander's confinement model [34] can be considered to be adequate for measuring the confinement strength of NiTi because the relative difference between measured and calculated confinement strengths in steel and Nitinol cubes were similar. In general, steel confined cubes acquired higher compressive strengths than Nitinol confined cubes. This can be explained by the relatively higher modulus of elasticity of steel compared to Nitinol. The higher modulus of elasticity of steel prevented excessive deformation in the confined cubes under loading as compared to the softer NiTi. This in turn prevented gradual damage in concrete. Specimens CNH and CSL had the same confining bar diameters. Comparing them to each other shows that CNH had a compressive strength of 5.78 Ksi (39.85 MPa) whereas CSL had a higher compressive strength of 7.33 Ksi (50.53 MPa) (Table 4-2).

Measured and calculated strains at compressive strengths were significantly different, in part, because the measured data included machine deformation (Table 4-2). Ratios of measured to calculated strains at compressive strength ranged from 3.5 to 4.8 for all specimens, which is consistent. Although the measured and calculated strains are significantly different, the consistency of the 3.5 to 4.8 factor common in all specimens' results that is caused by the machine deformation, implies that Mander's confinement equation [34] can be fairly accurate in approximating confinement strains. This is because Mander's equation [34] is mostly used in approximating confinement properties and has been proven to give fairly accurate results for steel confinement. In this case, the error factor between the measured and calculated strains in steel and Nitinol confined cubes are consistent. Strains reached by C-S specimens were higher than those achieved by C-N specimens (Table 4-2). Ultimate compression strains reached by C-S specimens were also higher than those reached by the C-N specimens (Table 4-3). Higher strains and compressive strengths in the steel confined cubes indicated that steel-confined cubes have higher energy dissipation capacity than Nitinol confined cubes.

In addition, NiTi did not improve deformation recovery in the cubes. CNH and CSL had the same bar diameter. Superimposing the stress-strain curves of both cubes show that residual strain in CSL is lower than that of CNH (Fig. 4-2). Although CSL has a lower residual strain than CNH, CNH reached higher strains during experimental tests (Fig. 4-2). To give a fair evaluation of deformation recovery, the ratios of residual strain to maximum strain for each specimen were compared. CNH had a ratio of 0.80 whereas CSL had a slightly lower ratio of 0.77. Both ratios were similar; therefore, using NiTi in such a method of confinement was unsuccessful.

This confinement study was only exploratory. The use of NiTi wire as spiral reinforcement was not studied due to time constraints. Further testing on spirally confined specimens could be done by wrapping NiTi wire around a cylindrical specimen from the outside, and using the anchorage mechanism discussed in Chapter 3 to anchor the ends of the wire from the top and bottom of the specimen.

4.3 Response of Beams

In this section, measured results will be compared to calculated results for the test beams. Load-displacement, Stiffness, and displacement ductilities will be discussed. Significant differences were expected between the calculated and measured yield displacements, which in turn affected the ultimate displacements. These differences were due to the complex beam system used in experimental tests. There were many connections used outside the beam itself to facilitate the reuse of SMA and steel reinforcement in the critical region. These connections had to have some effect on the stiffness of the system that in turn affected displacements. Reinforcement used outside the concrete area of the beam structure was not expected to act similar to a system that had reinforcement embedded in the concrete. A beam that has reinforcements embedded in the concrete would have frictional forces acting between reinforcement and concrete that would allow the system to act as a whole. Slippage between them might come later as loads increase. In the case that was used in the experimental tests in this paper, no frictional forces were acting between reinforcements and the concrete in the beam because reinforcements were anchored to the beam from the outside using angles. These connections were joined using nuts and washers. Connections were only placed at the middle of the beams, were angles were located, and at the end of the beams. These connections had washers and nuts that could affect the measured displacement results because of the deformations occurring at these joints.

4.3.1 Load-Displacement

The measured and calculated load-displacement results are discussed in this section. Analytical load-displacement results were found by doing a moment-curvature analysis using RCMC [34]. Moment-curvature analysis for each beam was done for three different sections. Two of those sections remained constant for all eight beams. These two sections were the end of the beam where the section was 12 inches (304.8 mm) deep, and the section of the beam where the external Grade B-7 steel reinforcement was placed. These sections were significantly stiffer than the middle region of the beam where the reinforcements were changed depending on the specimen tested (Table 4-4).

Calculated load-displacement results were then found from the moment-curvature results obtained from RCMC [34] using moment-area method. The measured load-displacement results were superimposed on the calculated ones (Figs. 4.3-4.10). Each figure shows two curves. The dashed curves represent the calculated load-displacement results whereas the solid curves represent the measured load-displacement results. Measured and calculated load-displacement curves were significantly different for all

specimens except for BNH1 and BNL2. Reasons for this were discussed previously in Section 4-3.

Table 4-5 shows that the calculated yield loads were close to the measured yield loads. In general, calculated yield loads exceeded the measured yield loads with the exception of specimen BNL1, which had a lower calculated yield load (Table 4-5). Specimen BNH1 results were the most accurate of all other beams (Table 4-5). Three specimens were loaded until failure. These specimens were BNH2, BSH1, and BSH2. Measured ultimate loads were close to the calculated ones (Table 4-5). In general, calculated ultimate loads were slightly lower than measured ones. These results meant that common analysis and design methods used on conventional steel reinforced beams could be applied to estimate the capacity of Nitinol reinforced beams.

4.3.2 Measured and Calculated Stiffness

Calculated and measured beam effective pre-yield stiffnesses were significantly different due to reasons mentioned in Section 4.3. In general, the measured pre-yield stiffness estimations were higher than calculated ones except for BNL1 (Table 4-6). The calculated stiffnesses of BN specimens were closer to the test data than those of BS specimens were. The ratio of measured to calculated stiffness for BN specimens ranged from 0.52 to 1.93, whereas the range of measured to calculated stiffness for BS specimens was 3.00 to 4.87. Comparisons made between the measured BN and BS initial tangent and effective pre-yield stiffness were discussed previously in Section 3.5.2.4.

4.3.3 Displacement Ductility

Termination of experimental testing of the B-N specimens was dictated by the amount of strains in the Nitinol bars. The strains in Nitinol bars were closely monitored during experimental testing and B-N specimens were carefully loaded so that the Nitinol bars would not fail. Failure of the bars was not accepted because they were going to be reused in other beam and cube tests. The Nitinol bars are reusable because of the superelastic property they have that allows them to recover deformations even after yielding.

Three specimens failed due to damage to concrete. These specimens are BNH2, BSH1 and BSH2. Measured displacement ductilities of failed beams were found from the ratio of ultimate to yield displacements. Measured displacement ductilities for beams that did not fail were found from the ratio of maximum to yield displacements. Measured maximum and yield deflections were affected by the complexity of the beam specimens as mentioned in Section 4.3, which in turn caused the inconsistency between measured and calculated results.

Ultimate measured displacement ductility of specimen BNH2 is 1.87 (Table 4-7). BNH2 had the same reinforcement ratio as BSL2. Maximum measured displacement ductility of BSL2 is 3.96, which is more than twice what BNH2 anticipated at ultimate (Table 4-7). BSL2 had higher displacement ductility than BNH2 although BSL2 was not loaded to failure. Loading BSL2 to failure would lead to even higher ultimate displacement

ductility. The lower displacement ductility achieved by BNH2 can be explained by the higher yield displacement it has. The reason Nitinol has a higher yield displacement is because its modulus of elasticity is lower than that of steel, which, in turn, lowered the stiffness of the beam. Table 4-8 lists the measured displacement ductilities reached by the beam specimens indicating if the beam failed or not.

Capability of NiTi-reinforced beams to recover their maximum displacement was evaluated at different ductility ratios. Table 4-9 shows the ratio of the residual displacement to the maximum displacement at different displacement ductilities. Displacement ductilities ranged from 1.0 to 4.0 increasing at increments of 0.5. Linear interpolation was used to obtain data for intermediate ductilities when required displacement ductilities fell in between actual measured data points. Not applicable (N.A) was used to mark ratios for relative displacement ductilities that were not reached in experimental testing. In general, B-N specimens had significantly lower ratios. This implied that the relative ratios of residual displacements for varying displacement ductilities for B-N specimens were lower than those of B-S specimens. The average of the ratios calculated for B-N specimens ranged from 0.01 to 0.186 whereas the average of the ratios calculated for the B-S specimens ranged from 0.254 to 0.515 (Table 4-9). Ratio of the average value of the B-N specimens to the average value of the B-S specimens was calculated for the relative displacement ductilities. The ratios ranged from 0.021 to 0.681(Table 4-9). The ratios of the B-N to B-S specimens decreased as displacement ductilities increased. This phenomenon can be explained by the fact that higher permanent deformations accompanied an increase in displacement ductilities for the B-S specimens since steel longitudinal reinforcements yielded. On the other hand, NiTi longitudinal reinforcements in the B-N specimens would try to recover fully any strains, even after yielding due the superelastic property. Any residual deformations visible in the B-N systems would occur because of the fact that superelastic recovery stresses in the NiTi bars were not sufficient to close the cracks completely in the concrete beam.

4.4 Analysis of Full Scale Beams

4.4.1 Descriptions of The Beams

Four theoretical models were studied to demonstrate the effect of using Nitinol (NiTi) as conventional longitudinal reinforcement on one hand, and in hybrid systems on the other. Hybrid systems were modeled in order to study their effect on the stiffness of the beam. Using NiTi alone as reinforcement was expected to lower stiffness of the beam dramatically as was proven in the experimental study discussed previously in Chapter 3 and this chapter. A conventionally reinforced singly supported steel beam was used as a benchmark for comparison. The three other models consisted of Nitinol alone, NiTi and a high strength steel (HS steel) hybrid system, and NiTi and a carbon fiber reinforced plastic (CFRP) hybrid system. In all models, the longitudinal reinforcement in the plastic hinge region was the variable with all other reinforcement remaining constant. The concrete in the beam was modeled as unconfined with a strain of 2,000 me at concrete strength of

4000 psi (27.6 MPa), and a strain of 4,000 me at ultimate strength. The beam has a span of 240 inches (6096 mm), a height of 18 inches (457.2 mm) and a width of 12 inches (304.8 mm). The 4 beams had a reinforcement ratio of about 0.005 in the plastic hinge region and 0.01 in the rest of the beam. A higher reinforcement ratio was used in areas other than the plastic hinge region in order to provide it with enough flexural capacity to avoid premature failure in these regions. Two symmetrical point loads are applied on the beam, 40 inches (1016 mm) apart at midspan (Fig. 4-11). Nitinol (NiTi) and steel used as longitudinal reinforcement were assumed to have a yield stress of 60 ksi (414 MPa). High strength steel used in the analysis was assumed to have a yield stress of 120 ksi (827 MPa). The CFRP bars had a yield stress of 180 ksi (1241 MPa). Modulus of elasticity of steel, NiTi, high strength steel, and CFRP were, respectively, 29,000 ksi (199,947 MPa), 12,000 ksi (82,700 MPa), 29,000 ksi (199,947 MPa) and 14,000 ksi (96,526 MPa). The moduli of elasticity of NiTi and CFRP used in analysis were based on the common products available on the market.

The reinforcement ratio of 0.005, while still within the ACI limits, is close to the minimum amount specified by ACI. In principle, the ACI limits are intended to ensure ductile failure. Because of the high yield strain of NiTi, the upper limit on NiTi-reinforced beams is considerably lower than that of steel-reinforced beams, thus making 0.005 a reasonable value.

The total area of the reinforcement used in the plastic hinge region of the beams was calculated to be 1.08 in^2 (697 mm^2). In the steel only and NiTi only beams, the whole area was allocated for either case. In the hybrid models, the initial assumption was to allocate half the reinforcement area for NiTi and the other half for either CFRP or HS steel, depending on what is used. Such a distribution of the longitudinal reinforcements in the hybrid systems seemed to be unreasonable because the hybrid system sections would have significantly higher yield loads than the single type reinforced beams. Another distribution of reinforcements in the hybrid systems was used. To allow for comparison of all the models, the areas of reinforcement in hybrid models was reduced in a way that the first yield load was the same as that of the steel alone and NiTi alone models. That is, in the NiTi and HS steel beam, the HS steel would yield before the NiTi. Therefore, the area of HS steel was reduced from 0.54 in^2 (348.4 mm^2) to 0.33 in^2 (212.9 mm^2) while the area of NiTi remained constant at 0.54 in^2 (348.4 mm^2). On the other hand, in the NiTi and CFRP beam, the NiTi reinforcement would yield before the failure of CFRP. Therefore, the area of NiTi was reduced from 0.54 in^2 (348.4 mm^2) to 0.43 in^2 (277.4 mm^2) while the area of CFRP remained constant at 0.54 in^2 (348.4 mm^2).

Moment-curvature analysis was performed on each section using RCMC [35] program (Fig. 4-13). Applying moment-area method on moment-curvature results gave load-displacement relationships for the 4 models (Fig. 4-14).

4.4.2 Load-Deformation Responses

The failure of concrete controlled the ultimate point in all models. In the NiTi and high strength steel model, the HS steel yielded before the NiTi because HS has a lower yield strain. The load-displacement curve shows clearly a reduction in the beam stiffness

after the first yield (Fig. 4-14). In this model, not full deformation recovery is expected since the HS steel, which has a modulus of elasticity higher than that of NiTi, yields and permanent deformation in the stiffer HS steel bar would lead to permanent displacement in the beam. In the NiTi and CFRP model, NiTi reinforcement yielded before the CFRP failed. CFRP ultimate strength and modulus of elasticity were chosen so that concrete failure and yielding of NiTi would occur prior to failure of CFRP, thus preventing a brittle failure. This was done to demonstrate that such a hybrid system could be used to increase deformation recovery while dissipating energy from the system at higher cyclic or dynamic loading. Since the CFRP reinforcement will remain elastic until failure of concrete, this property means that deformations accompanied by high loads on the beam that would essentially yield the NiTi reinforcement and reduce stiffness of the beam, could be mostly, if not fully, recovered. In addition to that, NiTi reinforcements would help dissipate energy from the system due to yielding.

First yield loads reached by all models were similar since this is how they were designed (Table 4-10). Yield displacement in the NiTi case was significantly higher than that of steel (Table 4-10). The ratio of steel yield displacement to that of NiTi was 0.61. This can be explained by the lower modulus of elasticity of NiTi. The other two hybrid systems had lower yield displacements than that of NiTi alone, but higher than that of steel alone (Table 4-10). The ratio of steel yield displacement to that of NiTi+HS steel and NiTi+CFRP respectively were 0.73 and 0.66. This was expected since the stiffness of the hybrid sections were relatively higher than that of the NiTi alone reinforced beams. The higher stiffness was caused by the higher moduli of elasticity of the CFRP and HS steel with respect to NiTi, which was placed in combination with the NiTi reinforcement. Ultimate loads in the steel alone beam and NiTi alone were close (Table 4-11). The ultimate displacement of the steel reinforced beam was lower than that of the NiTi. The ratio of steel ultimate displacement to that of NiTi was 0.83 (Table 4-11). On the other hand, the ultimate displacement reached by the NiTi+CFRP was the highest (Table 4-11). The value of the ultimate displacement of the NiTi+HS steel beam came in between those of the NiTi alone and steel alone beams.

4.4.3 Initial Stiffness

The initial stiffness of the steel reinforced beam was higher than that of NiTi (Table 4-11). The ratio of steel alone beam stiffness to that of NiTi alone was 1.61. NiTi was used as longitudinal reinforcement only in the plastic hinge region, which coincided with the length between the two point loads. This length was calculated to be approximately 40 inches (1016 mm). The span of the beam was 240 inches (6096 mm). This meant that NiTi longitudinal reinforcement was used in $1/6^{th}$ of the span length of the beam and the stiffness of the beam was reduced down to about $3/5^{th}$ of that of the steel beam. To illustrate the effect of using hybrid systems on the overall initial stiffness of the beam, the initial stiffness ratios of steel to NiTi+HS steel and steel to NiTi+CFRP were considered. The ratio of Steel to NiTi+HS steel was 1.32, which is less than the ratio of steel to NiTi (1.61) (Table 4-11). This meant that stiffness of beam increased from $3/5^{th}$ to $2/3^{rd}$ of that of steel alone. On the other hand, the ratio of steel stiffness to NiTi+CFRP stiffness was

similar to that of steel to NiTi. Both had ratios of 1.56 and 1.61 respectively (Table 4-11). The similarity of the beam initial stiffness with the NiTi alone and the NiTi+CFRP was due to the fact that the modulus of elasticity of CFRP was close to the modulus of elasticity of NiTi.

4.4.4 Displacement Ductilities

The load-displacement relationship of all beams was transformed into an elastic-plastic bilinear relationship (Fig. 4-15). This was done by, first superimposing the elastic part of the load-displacement graph with the whole graph. Second, the elastic line was extended and the plastic line was drawn, simultaneously equating the areas above and below the plastic line with respect to the inelastic region of the original load-displacement relationship. This transformation was applied to determine their effective yield displacements in order to find the displacement ductilities. Displacement ductility of the steel alone model was found to be the highest with a value of 2.11 (Table 4-11). The NiTi alone and NiTi+HS steel displacement ductilities came second with values of 1.63 and 1.72 respectively (Table 4-11). The NiTi+CFRP had the lowest displacement ductility of 1.49 (Table 4-11). The ranking of displacement ductilities, from highest to lowest, coincided with the ranking of the stiffness from highest to lowest except with the NiTi+CFRP. The NiTi+CFRP beam had lower effective displacement ductility, because when converting the relationship from its original form to the elastic-plastic bilinear form, the high slope of the elastic region of the graph caused a major increase in the effective yield point. This caused a decrease in the displacement ductility since the ratio of ultimate to yield displacement decreased.

4.4.5 Concluding Remarks

This theoretical study showed that using NiTi alone as longitudinal reinforcement could lead to reinforced concrete elements with lower stiffness. As mentioned above, NiTi reduced the displacement ductility and the stiffness of the beam whereas yield and ultimate loads were not affected significantly. On the other hand, NiTi showed extraordinary deformation recovery after yielding of the beam specimens in the experimental results (Section 3-4). In some cases full deformation recovery was observed in BN specimens. Hybrid systems that have NiTi as part of the longitudinal reinforcement in the plastic hinge region would be a better choice of design. Stiffness could be increased while maintaining similar displacement ductility relative to using NiTi alone as can be seen in the NiTi+CFRP hybrid system. In addition to that, lower stiffness of sections reinforced by NiTi or a combination of NiTi and HS steel/or CFRP can be utilized in a useful manner. NiTi reinforcements embedded in engineered cementitious composites (ECC), which has a high elastic deflection capacity, could result in structural elements with relatively high flexural strength and sufficient elastic deflection capacity to prevent the formation of a collapse mechanism under extreme dynamic loading events, while fully recovering deformations caused by dynamic excitations [25].

CHAPTER 5: Summary and Conclusions

5.1 Summary

Collapse and severe damage of reinforced concrete structures during strong earthquakes has been a major concern for structural engineers. Current and past research was based on yielding steel reinforcement in order to dissipate the earthquake energy. This meant the preserving of lives, but at the expense of structures, which would be severely damaged. In this report, the super-elastic behavior of Nitinol (NiTi), one of the most used shape memory alloys (SMAs), was used in experimental tests to observe the extent of the ability of this alloy to dissipate energy, reduce permanent damage, and explore its confinement effect on concrete. This characteristic of NiTi can cause a major leap in seismic design, since the base of seismic design is to yield steel to dissipate energy while encountering permanent deformation, whereas NiTi would yield under strains accompanied by seismic loads and can recover deformations. This research was a preliminary study to understand this material and its interaction with concrete.
This research was mostly experimental, but included analytical studies of test beams, cubes, and full-scale beams. The test beams included eight small-scale beams. The beams were 5 feet (1.53 m) long with a cross sectional area of 5 x 6 inches (127 x 152 mm) in the middle area and a cross sectional area of 5 x 12 inches (127 x 305 mm) at the ends. The beams were tested under two point cyclic loads. The test variables were the type and amount of reinforcement in the critical section at midspan, which was 6 inches (152 mm) long. The bar diameters used in NiTi reinforced beams were of $^3/_8$" (9.525 mm) and ¼" (6.35 mm) diameter. In addition, conventional # 4 (F13 mm) and # 3 (F10 mm) Grade 60 steel bars were used in the tests. The beams were divided into two groups. Each group consisted of four beams. Group 1 was reinforced in the longitudinal direction in the middle of the beam with Nitinol rods while group 2 was reinforced with conventional steel bars. Beams with conventional steel were tested to establish the benchmark.

The cube tests included eleven 6 inch (150 mm) standard concrete cubes. Three cubes were unconfined, four cubes were confined with NiTi bars, and four were confined with steel bars. The cubes were tested under uniaxial cyclic load. The test variables were the type and amount of confinement in the cubes. The focus of the tests was to test confining effects of Nitinol (NiTi) on concrete. Two prefabricated holes were embedded in the concrete cubes. The bar NiTi diameters used in the tests were of $^3/_8$" (9.525 mm) and ¼" (6.35 mm) diameter, and went through the prefabricated holes and were then attached to confining steel plates that covered 64% of the cube face. In addition, conventional # 4 (F13 mm) and # 3 (F10 mm) Grade 60 steel bars were used in the experimental tests. The Nitinol confinement effect was compared with and judged based on the confining ability of conventional steel bars.

The study of full-scale beams was analytical and it included the study of four models to demonstrate the effect of using Nitinol (NiTi) as longitudinal reinforcement by themselves or in hybrid systems. Hybrid systems were modeled to study their effect on the stiffness and ductility of the beam. Using NiTi alone as reinforcement was expected to lower the stiffness of the beam dramatically. A conventionally steel reinforced simply

supported beam was used as a benchmark for comparison. The three other models consisted of Nitinol alone, a NiTi and high strength steel (HS steel) hybrid system, and a NiTi and carbon fiber reinforced plastic (CFRP) hybrid system. In all models, the longitudinal reinforcement in the plastic hinge region was the variable with all other reinforcement remaining constant. The beam had a span of 240 inches (6096 mm), a height of 18 inches (457.2 mm) and a width of 12 inches (304.8 mm). Two symmetrical point loads were applied on the beam, 40 inches (1016 mm) apart at midspan. To allow for comparison of all the models, the areas of reinforcement in hybrid models were reduced in a way that first yield load was the same in all the beams.

5.2 Conclusions

The ability of shape memory alloys (SMAs), specifically Nitinol (NiTi), to recover deformations and dissipate energy in flexural simply supported beams introduced in this study was experimentally verified. In contrast NiTi was not able to recover its deformation when used in confinement of the cubes. There was, however, an increase in concrete compressive strength due to confinement. The NiTi confinement ability requires more research since conventional spiral and tie confinement was not tested due to time constraints.

In general, experimental tests proved NiTi to be an excellent type of alloy for controlling deformations and recovering them when used as longitudinal reinforcement in concrete beams. Beam experimental results showed that beam plastic hinge sections reinforced with NiTi longitudinal reinforcements exhibit large deformation recovery, if not fully, even in underreinforced sections. Lower stiffness of the sections reinforced with NiTi due to its lower modulus of elasticity, when compared to steel, could be adjusted by using it in hybrid sections. For example, a combination of NiTi and high strength steel reinforcements. Lower stiffness of sections reinforced by NiTi can be utilized in a useful way. NiTi reinforcements embedded in engineered cementitious composites (ECC), which has a high elastic deflection capacity, results in structural elements with relatively high flexural strength and sufficient elastic deflection capacity to prevent the formation of a collapse mechanism under extreme dynamic loading events.

In light of this exploratory study, the following conclusions can be drawn:

1. The average residual displacement in the NiTi reinforced test beams was less than one-fifth of that of the steel reinforced test beams.
2. All Nitinol (NiTi) bars showed pseudo-elastic behavior when used as a longitudinal reinforcement in the beam specimens. Bars almost fully recovered deformation without any residual strains even after strains well in excess of yield strains were experienced. The average residual strains of the similarly reinforced NiTi and steel beams were 0.004 and 0.017 respectively. This meant that the steel reinforced beam had an average residual strain 4.25 times higher than that that of the NiTi reinforced beam.
3. Displacement ductilities in NiTi and steel reinforced beams were nearly the same.

4. The stiffness of NiTi reinforced test beams was lower than those of the steel reinforced test beams. Comparisons made between NiTi and steel reinforced test beams showed that stiffnesses were reduced by approximately 60%.
5. Measured moment - curvature results demonstrated significant curvature recovery in all NiTi reinforced tests beams compared to the steel reinforced beams. The lowest recorded residual curvature was zero for the NiTi beams. The ratio of residual curvatures for NiTi beams to steel beams with similar reinforcement was 1 to 4.
6. Ultimate loads reached by NiTi confined cubes were significantly lower than those confined by conventional steel. The ratio of the average of the ultimate loads reached by NiTi confined cubes to that of steel was 0.73. The lower modulus of elasticity of NiTi compared to steel caused excessive deformations in the cube at lower loads, which in turn led to early crushing of concrete at lower loads than that of the steel cubes.
7. NiTi used for confinement in cubes did not improve deformation recovery. The ratios of concrete residual strain to maximum strain for NiTi and steel confined cubes were compared. NiTi cubes had an average ratio of 0.80 whereas the steel cubes had a ratio of 0.77. Both ratios were close; therefore, using NiTi in such a method of confinement was not beneficial.
8. The theoretical study of full scaled beams showed that using NiTi alone as longitudinal reinforcement could lead to reinforced concrete elements with lower stiffness than that of steel reinforced beams. NiTi reduced the displacement ductility and the stiffness of the beam whereas yield and ultimate loads were not affected significantly. Hybrid systems that have NiTi as part of the longitudinal reinforcement in the plastic hinge region combined with high strength steel or CFRP appeared to be a better choice of design.

REFERENCES

1. Otsuka, K. and Wayman, C. M. (1998) *Shape Memory Materials*, Cambridge University Press.

2. Eucken, S. (1991) *Progress in Shape Memory Alloys*, Alle Rechte Vorbehalten.

3. Auricchio, F., Faravelli, L., Magonette, G. and Torra, V. (September 1998) *Shape Memory Alloys. Advances in Modelling and Applications*, Printed by: Artes Graficas Torres 17, 08029 Barcelona, Spain

4. Gall, G., Sehitoglu, H., Anderson, R., Karaman, I., Chumlyakov, Y.I. and Kireeva, I.V., "On the Mechanical Behavior of Single Crystal NiTi Shape Memory Alloys and Related Polycrystalline Phenomenon," *Material Science and Engineering* A317 (2001), pp.85-92

5. Auricchio, F., "A Robust Integration-Algorithm for a Finite-Strain Shape-Memory-Alloy Superelastic Model," *International Journal of Plasticity*, Volume 17 (2001), pp.971-990

6. Peng, X., Yang, Y. and Huang, S., "A comprehensive Description for Shape Memory Alloys with a Two-Phase Constitutive Model," *International Journal of Solids and Structures*, Volume 38 (2001), pp.6925-6940

7. Saadat, S., Salichs, J., Duval, L., Noori, M.N., Hou, Z., Bar-on, I. and Davoodi, H., "Utilization of Shape Memory Alloys for Structural Vibration Control," A summary review for presentation at US-Japan workshop on Smart Materials and New Technologies for Improvement of Seismic Performance of Urban Structures, Disaster Prevention Research Institute Kyoto University, Japan, February 17-18,1999. Building Research Institute, Tsukuba City, Japan, February 19, 1999

8. Special Metals Corporation. New Hartford, New York. http://www.specialmetals.com/

9. Nitinol Devices and Components (NDC). Fremont, California. http://www.nitinol.com/

10. Memry Western Corporation. Menlo Park, California. http://www.memry.com/

11. Shape Memory Applications, inc. San Jose, California. http://www.sma-inc.com/

12. Krstulovic-Opara, N. and Naaman, A.E., "Self-Stressing Fiber Composites," *ACI Structural Journal*, Title no. 97-S38 (March-April 2000), pp. 335-344

13. Clark, P. W., Aiken, I. D., Kelly, J. M., Higashino, M. and Krumme, R. C., "Experimental and Analytical Studies of Shape Memory Alloy Dampers for Structural Control," *Smart Structures and Materials 1995: Passive Damping,* Proceedings of SPIE, Volume 2445 (1995), pp. 241-251

14. Krumme, R.; Hayes, J.; and Sweeney, S., "Structural Damping with Shape-Memory Alloys: One Class of Devices," *Smart Structures and Materials: Passive Damping,* Proceedings of SPIE, Volume 2445 (1995), pp. 225-240

15. Ju, D.Y. and Shimamoto, A., "Damping Properties of Epoxy Matrix Composite Beams with Embedded Shape Memory Alloy Fibers," *Journal of Intelligent Material Systems and Structures*, Volume 10 (1999), pp. 514-521

16. Bidaux, J.E., Manson, E. and Gotthardt, R., "Active Stiffening of Composite Materials By Embedded Shape-Memory-Alloy Fibers," *Materials for Smart Systems II*, Volume 459 (1997), pp.107

17. Saadat, S., Salichs, J., Duval, L., Noori, M.N., Hou, Z., Bar-on, I. and Davoodi, H., "Utilization of Shape Memory Alloys for Structural Vibration Control," A summary review for presentation at US-Japan workshop on Smart Materials and New Technologies for Improvement of Seismic Performance of Urban Structures, Disaster Prevention Research Institute Kyoto University, Japan, February 17-18,1999. Building Research Institute, Tsukuba City, Japan, February 19, 1999

18. DesRoches, R. and Delemont, R., " Seismic Retrofit of Bridges Using Shape Memory Alloy," *Engineering Structures,* Volume 24, Issue 3 (2002), pp. 325-332

19. Auricchio, F., Faravelli, L., Magonette, G. and Torra, V. (1998) *Shape Memory Alloys. Advances in Modelling and Applications*, Printed by: Artes Graficas Torres 17, 08029 Barcelona, Spain, pp. 285-287

20. Auricchio, F., Faravelli, L., Magonette, G. and Torra, V. (1998) *Shape Memory Alloys. Advances in Modelling and Applications*, Printed by: Artes Graficas Torres 17, 08029 Barcelona, Spain, pp. 287-291

21. Auricchio, F., Faravelli, L., Magonette, G. and Torra, V. (1998) *Shape Memory Alloys. Advances in Modelling and Applications*, Printed by: Artes Graficas Torres 17, 08029 Barcelona, Spain, pp. 291-296

22. Auricchio, F., Faravelli, L., Magonette, G. and Torra, V. (1998) *Shape Memory Alloys. Advances in Modelling and Applications*, Printed by: Artes Graficas Torres 17, 08029 Barcelona, Spain, pp. 313-323
23. Auricchio, F., Faravelli, L., Magonette, G. and Torra, V. (1998) *Shape Memory Alloys. Advances in Modelling and Applications*, Printed by: Artes Graficas Torres 17, 08029 Barcelona, Spain, pp. 324-333

24. Auricchio, F., Faravelli, L., Magonette, G. and Torra, V. (1998) *Shape Memory Alloys. Advances in Modelling and Applications*, Printed by: Artes Graficas Torres 17, 08029 Barcelona, Spain, pp. 333-343

25. Fischer, G. and Li, V., "Intrinsic Response Control of Moment-Resisting Frames Utilizing Advanced Composite Materials and Structural Elements," *ACI Structural Journal,* Title no. 100-S18 (March-April 2003), pp.166-176

26. American Institute of Steel Construction. (1998) *Load & resistance factor design: manual of steel construction / AISC Volume 1*, American Institute of Steel Construction printing, Chicago, Illinois

27. American Institute of Steel Construction. (1998) *Load & resistance factor design: manual of steel construction / AISC Volume 2*, Chicago, Illinois: American Institute of Steel Construction printing

28. ACI Committee 318. (2002) *Building code requirements for structural concrete: (ACI 318-02) and commentary (ACI 318R-02) / reported by ACI Committee 318* Farmington Hills, Mich.: American Concrete Institute printing

29. American Society for Testing and Materials (2000), ASTM C39-86, "Standard Test Method for Compressive Strength of Cylindrical Concrete Specimens". Philadelphia, Pa.: ASTM printing

30. Texas Measurements, Inc. P.O. Box 2618-303. Anderson College Station, TX 77841

31. Neville, Adam M. (1986) *Properties of Concrete*, Pitman Books.
32. Murdock, L. J., Brook K. M., and Dewar J. D. (1991) *Concrete Materials and Practice*, Edward Arnold.

33. Structural Analysis Program 2000 (SAP). Version 6.1. Computers and Structures, Inc. (1995). Berkeley, California.

34. Mander, J. B., Priestley, M. J. N. and Park, R., "Theoretical Stress-Strain Model for Confined Concrete," *ASCE Journal of Structural Engineering*, Volume 114, No.8 (August 1988), pp. 1804-1826

35. Wehbe, N. and Saiidi, M. (1999) "RCMC v.1.2: A Computer Program for Moment-Curvature Analysis of Confined and Unconfined Reinforced Concrete Sections," Report No.: CCEER-99-6

Table 2-1: Beam Test Variables

Specimen	Reinforcement Type	Reinforcement at Mid Span	Reinforcement Ratio (ρ) at Mid Span
B-N-L-1	Nitinol	1 bar, ϕ=0.25 in (ϕ=6.35 mm)	0.00115
B-N-L-2	Nitinol	2 bars, ϕ=0.25 in (ϕ=6.35 mm)	0.003
B-N-H-1	Nitinol	1 bar, ϕ=0.375 in (ϕ=9.525 mm)	0.00259
B-N-H-2	Nitinol	2 bars, ϕ=0.375 in (ϕ=9.525 mm)	0.00518
B-S-L-1	Steel	1 bar, ϕ=0.375 in (ϕ=9.525 mm)	0.00259
B-S-L-2	Steel	2 bars, ϕ=0.375 in (ϕ=9.525 mm)	0.00518
B-S-H-1	Steel	1 bar, ϕ=0.500 in (ϕ=12.7 mm)	0.00471
B-S-H-2	Steel	1 bar, ϕ=0.500 in (ϕ=12.7 mm)	0.00941

Table 2-2: Chemical Analysis of NiTi Provided by Special Metals Corporation

Element	WGT %
Nickel	55.90
Titanium	Balance
Oxygen	257 ppm
Carbon	374 ppm
Cu, Cr, Co, Mn, Mo, W, V	<0.01
Nb, Al, Zr, Si, Ta, Hf	<0.01
Ag, Pb, Bi, Ca, Mg, Sn, Cd	<0.01
Zn, Sb, Sr, Na, As, Be, Ba	<0.01
Fe	<0.05
B	<0.001
Hydrogen	14 ppm

Table 2-3: Specified Grade B-7 Steel Properties

Yield Strength (F_y)	105 Ksi (723.9 MPa)
Ultimate Strength (F_u)	125 Ksi (861.8 MPa)
Modulus of Elasticity (E)	29000 Ksi (200,000 MPa)

Table 2-4: Specified Grade A36 Steel Properties

Yield Strength (F_y)	36 Ksi (248.2 MPa)
Ultimate Strength (F_u)	58-80 Ksi (400-551.6 MPa)
Modulus of Elasticity (E)	29000 Ksi (200,000 MPa)

Table 2-5: Measured Compressive Strengths for Concrete in Beams

Description	Average Failure Load	Average Compressive Stress
7 day	115.955 kips (515.4 KN)	4.10 Ksi (28.3 MPa)
14 day	155.635 kips (691.8 KN)	5.50 Ksi (37.92 MPa)
28 day	163.118 kips (725.1 KN)	5.77 Ksi (39.78 MPa)

Table 2-6: Cube – Measured Concrete Compressive Strengths

Description	Average Cylinder Compressive Stress	Equivalent Cube Strength using L.J. Murdock	Equivalent Cube Strength using A.M. Neville
28 day	3.95 Ksi (27.23 MPa)	4.94 Ksi (34.06 MPa)	4.84 Ksi (33.37 MPa)

Table 2-7: # 3 - Measured Mild Steel Properties

Yield Strain	Yield Stress	Ultimate Stress	Young's Modulus of Elasticity
0.00215	63.64 Ksi (438.78 MPa)	106.82 Ksi (736.5 MPa)	29600 Ksi (204,085 MPa)

Table 2-8: # 4 - Measured Mild Steel Properties

Yield Strain	Yield Stress	Ultimate Stress	Young's Modulus of Elasticity
0.00208	61.25 Ksi (422.3 MPa)	94.125 Ksi (648.97 MPa)	29518 Ksi (203,519 MPa)

Table 2-9: Data Acquisition Instrumentation

Manufacturer:	Model:
National Instruments	SCXI-1121 Amplifier
National Instruments	SCXI-1321 Strain Terminal Block
National Instruments	SCXI-1327 Attenuator Block
National Instruments	PC-MCIA DAQ Card / AI-16-XE-50
National Instruments	LabVIEW software

Table 2-10: NiTi Rod - Measured Properties

Bar Size	Yield Strain	Yield Stress	Young's Modulus of Elasticity
0.375 inches (9.525 mm)	0.013	58 Ksi (400 MPa)	5034 Ksi (34078 MPa)
0.500 inches (12.7 mm)	0.013	74 Ksi (510 MPa)	5692 Ksi (39245 MPa)

Table 3-1: Maximum Load, Residual Displacement and Residual Strains in Bars for Cubes

Specimen	Maximum Load	Normalized Residual Displacement	Average of Normalized Residual Strains in Bars
C-N-L-1	126 Kips (560 KN)	0.72	0.94
C-N-L-2	127 (Kips (565 KN)	0.78	0.93
C-N-H-1	159 Kips (707 KN)	0.84	0.89
C-N-H-2	130 Kips (578 KN)	0.81	0.85
C-S-L-1	175 Kips (778 KN)	0.71	0.88
C-S-L-2	191 Kips (850 KN)	0.80	0.91
C-S-H-2	193 Kips (859 KN)	0.87	0.85

Table 3-2: Average of Maximum Loads, Average of Normalized Residual Displacements and Average of Normalized Residual Strains in Bars Reached by NiTi Specimens and Steel Cube Specimens

	Average of Maximum Loads	Average of Normalized Residual Displacement	Average of Normalized Residual Strains in Bars
C-N Specimens	136 Kips (603 KN)	0.79	0.90
C-S Specimens	186 Kips (829 KN)	0.79	0.88

Table 3-3: Summary of Displacements, Drift Ratios, Curvatures, Failure Mechanisms and Ductilities for Beam Specimens

	Yield Displacement	Yield Curvature	Yield Drift Ratio	Maximum Drift Ratio	Maximum Curvature	Maximum Dispalcement	Maximum Displacement Ductility	Maximum Curvature Ductility	Average Residual Crack Width	Failure Mode
B-N-H-1	0.1216 in (3.09 mm)	0.002801 rad/in (0.110275 rad/m)	0.0049	0.0160	0.004744 rad/in (0.186785 rad/m)	0.3995 inches (10.1473 mm)	3.29	1.69	N.R	None
B-S-L-1	0.0983 in (2.50 mm)	0.000742 rad/in (0.029212 rad/m)	0.0039	0.0057	0.001406 rad/in (0.055364 rad/m)	0.1420 inches (3.6068 mm)	1.44	1.90	0.0177 in (0.45 mm)	None
B-N-H-2	0.28275 in (7.18 mm)	0.002329 rad/in (0.091692 rad/m)	0.0113	0.0211	0.004688 rad/in (0.1845867 rad/m)	0.5278 inches (13.4061 mm)	1.87	2.01	0.049 in (1.25 mm)	Concrete Crushing
B-S-L-2	0.15345 in (3.90 mm)	0.000175 rad/in (0.006890 rad/m)	0.0061	0.0243	0.000897 rad/in (0.035333 rad/m)	0.6071 inches (15.4226 mm)	3.96	5.13	0.049 in (1.25 mm)	None
B-N-L-1	0.09385 in (2.39 mm)	0.001029 rad/in (0.040512 rad/m)	0.0038	0.0047	0.001173 rad/in (0.046185 rad/m)	0.1164 inches (2.9553 mm)	1.24	1.14	N.R	None
B-S-H-1	0.2475 in (6.29 mm)	0.000648 rad/in (0.025511 rad/m)	0.0099	0.0234	0.001723 rad/in (0.067857 rad/m)	0.5840 inches (14.8344 mm)	2.36	2.66	0.028 in (0.70 mm)	Concrete Crushing
B-N-L-2	0.1718 in (4.36 mm)	0.001211 rad/in (0.047677 rad/m)	0.0069	0.0139	0.003019 rad/in (0.118885 rad/m)	0.3469 inches (8.8130 mm)	2.02	2.49	0.039 in (1.00 mm)	None
B-S-H-2	0.38095 in (9.68mm)	0.001247 rad/in (0.049094 rad/m)	0.0152	0.0275	0.002444 rad/in (0.096222 rad/m)	0.6882 inches (17.4803 mm)	1.81	1.96	N.R	Shear-Flexure Failure

Table 3-4: Stiffness Properties

Specimen	Initial Tangent Stiffness	Effective Pre-Yield Stiffness
B-N-L-1	45.62 Kip/in (7.99 KN/mm)	39.85 Kip/in (6.98 KN/mm)
B-N-L-2	36.67 Kip/in (6.42 KN/mm)	33.80 Kip/in (5.92 KN/mm)
B-N-H-1	33.62 Kip/in (5.89 KN/mm)	30.93 Kip/in (5.42 KN/mm)
B-N-H-2	39.87 Kip/in (6.98 KN/mm)	37.98 Kip/in (6.65 KN/mm)
B-S-L-1	59.77 Kip/in (10.47 KN/mm)	52.09 Kip/in (9.12 KN/mm)
B-S-L-2	60.67 Kip/in (10.62 KN/mm)	55.13 Kip/in (9.65 KN/mm)
B-S-H-1	43.47 Kip/in (7.61 KN/mm)	41.66 Kip/in (7.29 KN/mm)
B-S-H-2	45.24 Kip/in (7.92 KN/mm)	43.67 Kip/in (7.65 KN/mm)
Average of B-N-H	36.75 Kip/in (6.44 KN/mm)	34.46 Kip/in (6.03 KN/mm)
Average of B-S-L	60.22 Kip/in (10.54 KN/mm)	53.61 Kip/in (9.39 KN/mm)
Ratio of B-N-H to B-S-L	0.61	0.64

Table 3-5: Maximum Load and Residual Deformations in Beams

Specimen	Maximum Load	Normalized Residual Displacement	Normalized Residual Strains in Bars	Normalized Residual Curvatures
B-N-L-1	3.89 Kips (17.31 KN)	0.023	0.00056	0.208
B-N-L-2	8.17 (Kips (36.36 KN)	0.246	0.00394	0.405
B-N-H-1	7.58 Kips (33.70 KN)	0.033	Not Recorded	0.247
B-N-H-2	15.91 Kips (70.78 KN)	0.061	0.00363	0
B-S-L-1	5.84 Kips (26.00 KN)	0.334	0.00796	0.465
B-S-L-2	15.01 Kips (66.75 KN)	0.534	0.01690	0.630
B-S-H-1	10.70 Kips (47.61 KN)	0.465	0.00580	0.431
B-S-H-2	21.02 Kips (93.51 KN)	0.461	0.00480	0.571

Table 3-6: Average of Maximum Loads, Average of Normalized Residual Displacements and Average of Normalized Residual Strains in Bars Reached in Beams

	Average Normalized Residual Displacement	Average Normalized Residual Strains in Bars	Average Residual Curvatures
B-N Specimens	0.091	0.0027	0.287
B-S Specimens	0.449	0.0089	0.524
Ratio of B-N to B-S Data	0.2	0.3	0.54

Table 3-7: Ratio of Residual Displacement to Maximum Displacement for Beams

Specimen	Ratio of Residual Displacement to Maximum Displacement
BNL1	0.0227
BNL2	0.2458
BNH1	0.0333
BNH2	0.0608
BSL1	0.3376
BSL2	0.5344
BSH1	0.4650
BSH2	0.4611
Ratio of BNH to BSL	0.0540
Ratio of BN to BSL	0.2016

Table 4-1: Confinement Pressure for Different Bars

Bar Diameter inches (mm)	Bar Material	Confinement Pressure psi (MPa)
0.25 (6.4)	Nitinol	178 (1.23)
0.375 (9.5)	Nitinol	509 (3.51)
0.375 (9.5)	Steel	440 (3.03)
0.500 (12.7)	Steel	800 (5.52)

Table 4-2: Measured and Calculated Confined Concrete Properties at Peak Strengths

Specimen	f'_{cc} Measured ksi (MPA)	ε'_{cc} Measured	f'_{cc} Mander's Equation ksi MPA	ε'_{cc} Mander's Equation	Ratio of Measured to Calculated Strengths	Ratio of Measured to Calculated Strains
C-N-L	5.07 (34.96)	0.0231	5.59 (38.57)	0.0048	0.91	4.8
C-N-H	5.78 (39.85)	0.0304	7.28 (50.18)	0.0088	0.79	3.5
C-S-L	7.33 (50.53)	0.0335	6.96 (48.80)	0.0076	1.05	4.3
C-S-H	7.75 (53.40)	0.0523	8.47 (58.41)	0.0112	0.91	4.6
Unconfined Cube	4.47 (30.82)	0.0071	None	None	None	None

Table 4-3: Measured and Calculated Confined Concrete Properties at Ultimate

Specimen	f_{cu} Measured	e_{cu} Measured	f_{cu} Mander's Equation	e_{cu} Mander's Equation
C-N-L	4.06 Ksi (27.97 MPa)	0.04235	4.48 Ksi (30.86 MPa)	0.0136
C-N-H	5.09 Ksi (35.10 MPa)	0.0370	5.82 Ksi (40.15 MPa)	0.036
C-S-L	5.86 Ksi (40.43 MPa)	0.0568	5.57 Ksi (38.40 MPa)	0.0312
C-S-H	6.20 Ksi (42.75 MPa)	0.0931	6.78 Ksi (31.88 MPa)	0.0568
Unconfined Cube	3.57 Ksi (24.61 MPa)	None	None	None

Table 4-4: EI Values for Constant Beam Sections

Section	EI K-in^2 (KN-m^2)
Beam End	742,706 (2,132)
Outer-Section	564,854 (1621)

Table 4-5: Measured and Calculated Yield and Ultimate Loads for Beams

Specimen	Measured Yield Load	Measured Ultimate Load	Calculated Yield Load	Calculated Ultimate Load
B-N-L-1	3.7 Kips (16.6 KN)	≥ 3.9 Kips (17.6 KN)	2.9 Kips (12.9 KN)	3.7 Kips (16.5 KN)
B-N-L-2	5.5 Kips (24.8 KN)	≥ 8.2 Kips (36.5 KN)	5.6 Kips (24.9 KN)	6.4 Kips (28.5 KN)
B-N-H-1	6.8 Kips (29.9 KN)	≥ 7.7 Kips (34.3 KN)	6.3 Kips (28.0 KN)	7.3 Kips (32.5 KN)
B-N-H-2	12.3 Kips (54.1 KN)	15.9 Kips (70.37 KN)	12.5 Kips (55.6 KN)	13.7 Kips (60.9 KN)
B-S-L-1	5.1 Kips (22.8 KN)	≥ 5.8 Kips (25.8 KN)	6.0 Kips (26.7 KN)	8.1 Kips (36.0 KN)
B-S-L-2	8.1 Kips (36.2 KN)	≥ 15.0 Kips (66.7 KN)	10.1 Kips (44.9 KN)	14.1Kips (62.7 KN)
B-S-H-1	8.3 Kips (36.7 KN)	11.80 Kips (52.49 KN)	8.8 Kips (39.1 KN)	11.1 Kips (49.4 KN)
B-S-H-2	16.5 Kips (73.5 KN)	21.05 Kips (93.64 KN)	17.7 Kips (78.7 KN)	19.8 Kips (88.1 KN)
Average of BNH	9.6 Kips (42.0 KN)		9.4 Kips (41.8 KN)	
Average of BSL	6.6 Kips (29.4 KN)		8.1 Kips (35.8 KN)	

Table 4-6 Measured and Calculated Stiffness for Beams

Specimen	Measured Effective Pre-Yield Stiffness	Calculated Effective Pre-Yield Stiffness	Ratio of Calculated to Measured Stiffness
B-N-L-1	39.9 Kip/in (7.0 KN/mm)	20.9 Kip/inch (3.7 KN/mm)	0.52
B-N-L-2	33.8 Kip/in (5.9 KN/mm)	45.1 Kip/inch (7.9 KN/mm)	1.33
B-N-H-1	30.9 Kip/in (5.4 KN/mm)	45.1 Kip/inch (7.9 KN/mm)	1.46
B-N-H-2	38.0 Kip/in (6.7 KN/mm)	73.5 Kip/inch (12.9 KN/mm)	1.93
B-S-L-1	52.1 Kip/in (9.12 KN/mm)	156.4 Kip/inch (27.4 KN/mm)	3.00
B-S-L-2	55.1 Kip/in (9.7 KN/mm)	173.7 Kip/inch (30.4 KN/mm)	3.15
B-S-H-1	41.7 Kip/in (7.3 KN/mm)	173.0 Kip/inch (30.3 KN/mm)	4.14
B-S-H-2	43.7 Kip/in (7.7 KN/mm)	213.0 Kip/inch (37.3 KN/mm)	4.87
Ratio of BNH1 to BSL1	0.59	0.29	None
Ratio of BNH2 to BSL2	0.69	0.42	None

Table 4-7: Measured and Calculated Displacement for Beams

Specimen	Measured Displacement Ductility
B-N-L-1	1.24
B-N-L-2	2.02
B-N-H-1	3.29
B-N-H-2	1.87
B-S-L-1	1.44
B-S-L-2	3.96
B-S-H-1	2.36
B-S-H-2	1.81

Specimen	Measured Displacement Ductility						
	1.0	1.5	2.0	2.5	3.0	3.5	4.0
BNL1	Yes	1.24					
BNL2	Yes	Yes	2.02				
BNH1	Yes	Yes	Yes	Yes	Yes	3.29	
BNH2	Yes	Yes	1.87 (Failed)				
BSL1	Yes	1.44					
BSL2	Yes	Yes	Yes	Yes	Yes	Yes	3.96
BSH1	Yes	Yes	Yes	2.36 (Failed)			
BSH2	Yes	Yes	1.81 (Failed)				

Table 4-8: Measured Displacement Ductilities for Beam Specimens

TABLE 4-9: MEASURED RATIO OF RESIDUAL DISPLACEMENT TO MAXIMUM DISPLACEMENT FOR BEAMS

Specimen	Measured Displacement Ductility						
	1.0	1.5	2.0	2.5	3.0	3.5	4.0
BNL1	0.273	N.A	N.A	N.A	N.A	N.A	N.A
BNL2	0.262	0.313	0.252	N.A	N.A	N.A	N.A
BNH1	0.046	0.069	0.119	0.133	0.010	N.A	N.A
BNH2	0.110	0.120	N.A	N.A	N.A	N.A	N.A
BSL1	0.27	N.A	N.A	N.A	N.A	N.A	N.A
BSL2	0.186	0.278	0.362	0.459	0.487	0.515	0.508
BSH1	0.260	0.369	0.466	N.A	N.A	N.A	N.A
BSH2	0.300	0.444	N.A	N.A	N.A	N.A	N.A
Average of NiTi Beams	0.173	0.167	0.186	0.133	0.01	N.A	N.A
Average of Steel Beams	0.254	0.363	0.414	0.459	0.487	0.515	0.508
Ratio of NiTi to Steel	0.681	0.460	0.449	0.290	0.021	N.A	N.A

Table 4-10: Yield Loads and Displacements

Model	First Yield Load kips (KN)	Second Yield Load kips (KN)	First Yield Displacement inches (mm)	Second Yield Displacement inches (mm)
Steel	18.8 (83.6)	N.A.	0.84 (21.27)	N.A.
Nitinol	19.4 (86.3)	N.A.	1.38 (35.22)	N.A.
NiTi + HS Steel	19.5 (86.8)	21.6 (95.9)	1.15 (29.14)	1.43 (36.40)
NiTi + CFRP	19.0 (84.4)	N.A.	1.28 (32.49)	N.A.
Ratio of Steel to NiTi Results	N.A.	N.A.	0.61	N.A.
Ratio of Steel to NiTi+HS Steel Results	N.A.	N.A.	0.73	N.A.
Ratio of Steel to NiTi+CFRP Results	N.A.	N.A.	0.66	N.A.

Table 4-11: Ultimate Loads and Displacement, Displacement Ductility and Stiffness

Model	Ultimate Load kips (KN)	Ultimate Displacement inches (mm)	Displacement Ductility	Stiffness kips/inch (KN/mm)
Steel	20.8 (92.5)	1.96 (49.7)	2.11	22.5 (3.9)
Nitinol	20.3 (90.3)	2.36 (94.14)	1.63	14.0 (2.5)
NiTi + HS Steel	30.2 (134.5)	2.08 (52.90)	1.72	17.0 (3.0)
NiTi + CFRP	34.5 (153.3)	2.89 (72.79)	1.49	14.4 (2.5)
Ratio of Steel to NiTi results	1.07	0.83	1.36	1.61
Ratio of Steel to NiTi+HS steel results	0.75	0.94	1.35	1.32
Ratio of Steel to NiTi+CFRP results	0.66	0.68	1.56	1.56

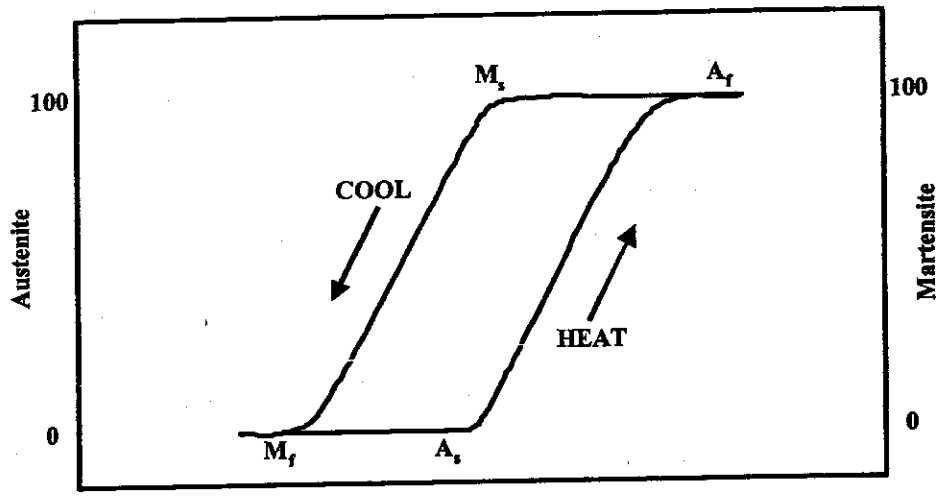

Figure 1-1: Temperature Hysteresis

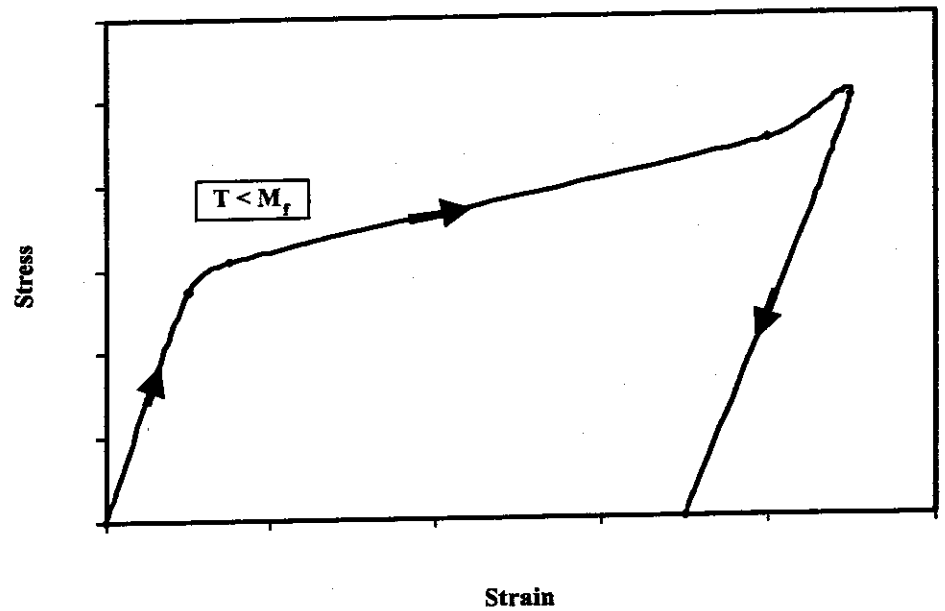

Figure 1-2: Stress-Strain Relationship

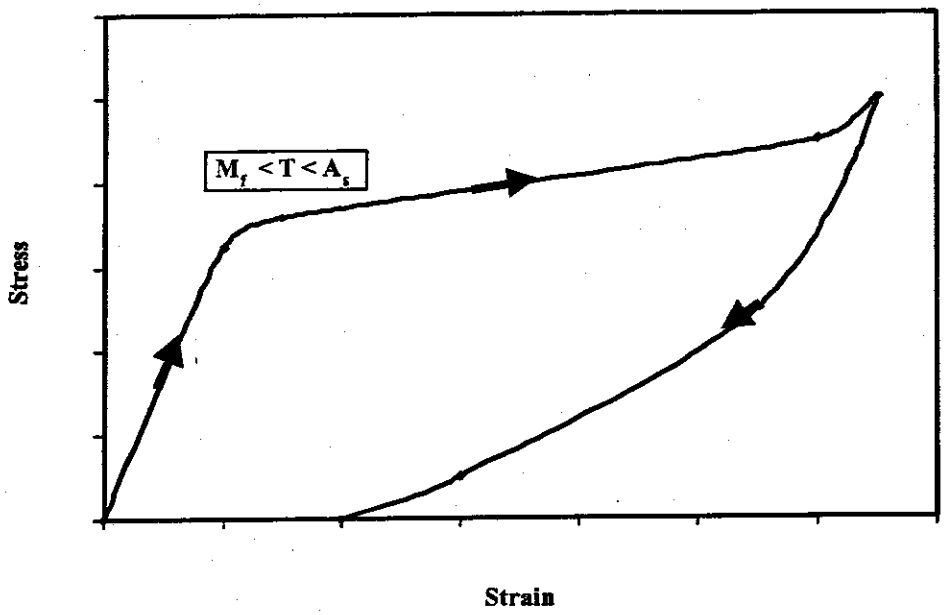

Figure 1-3: Stress-Strain Relationship

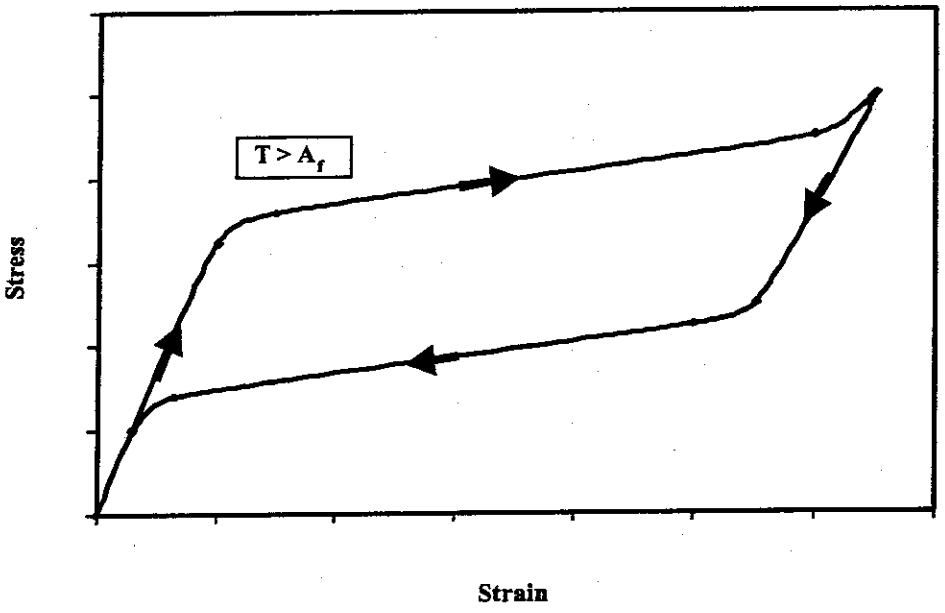

Figure 1-4: Stress-Strain Relationship

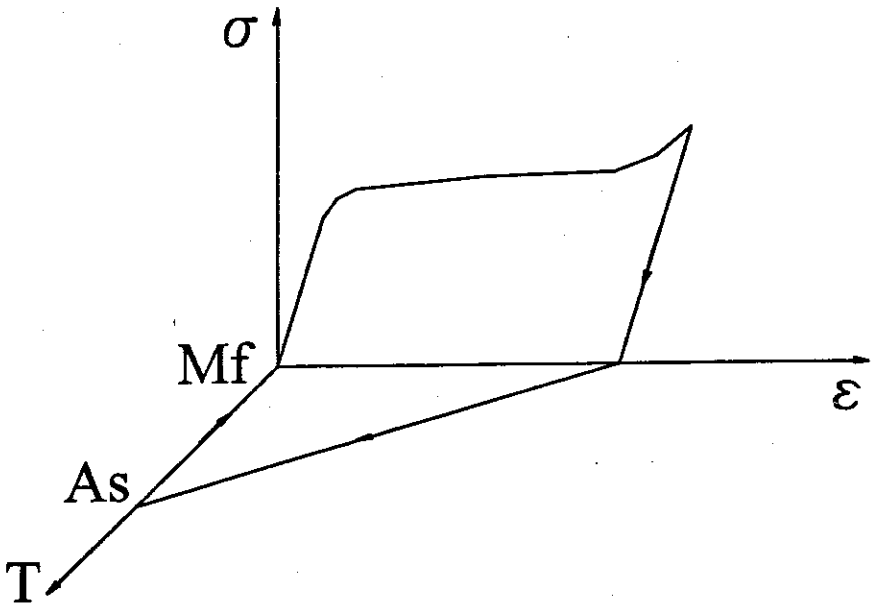

Figure 1-5: Stress-Strain-Temperature Curve of SME

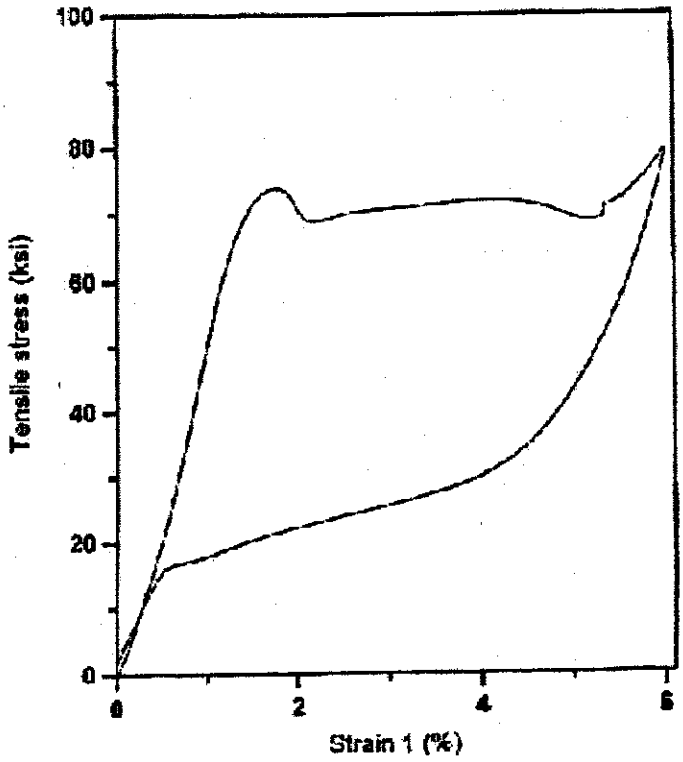

Figure 2-1: Stress-Strain of 0.500" NiTi Rod

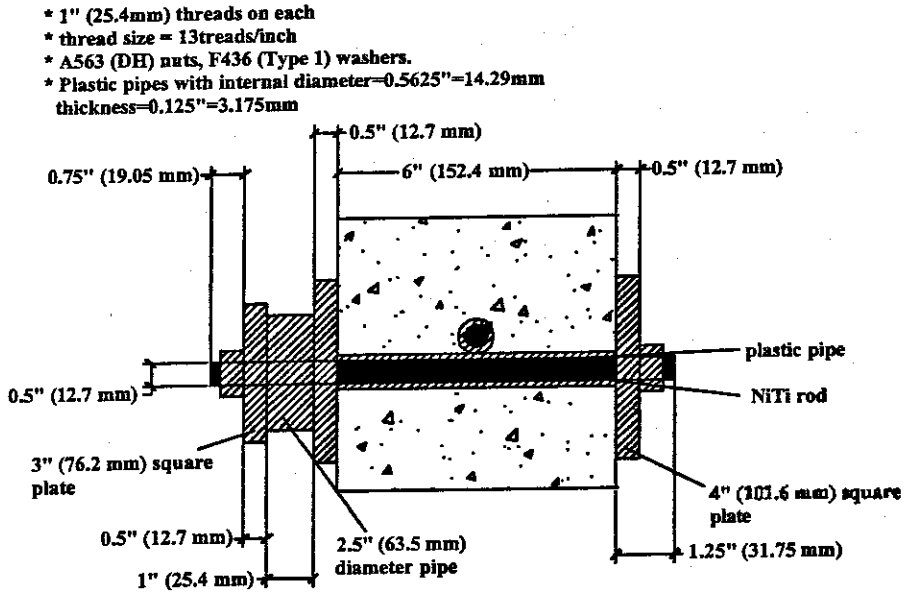

Figure 2-2: Cube Setup

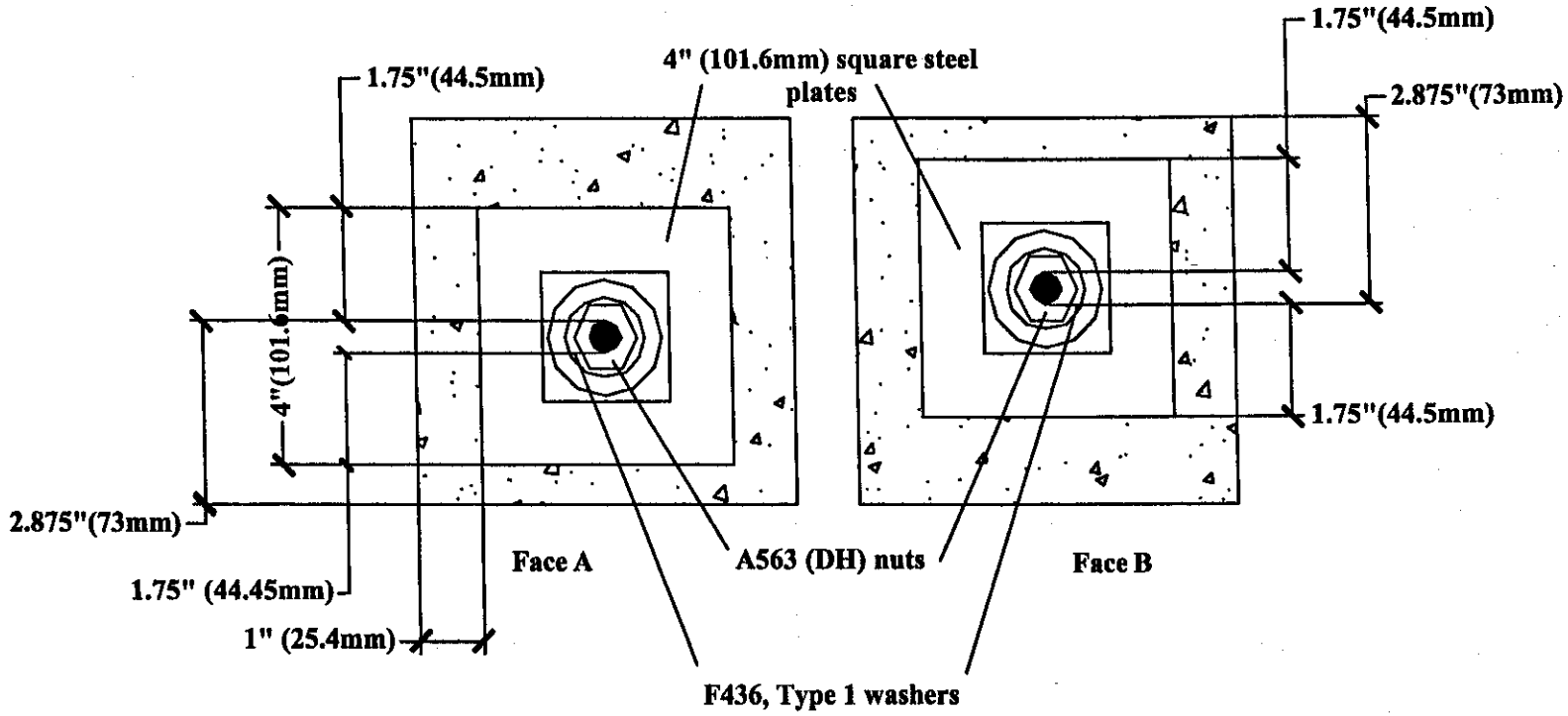

Figure 2-3: Cube Setup, Side View

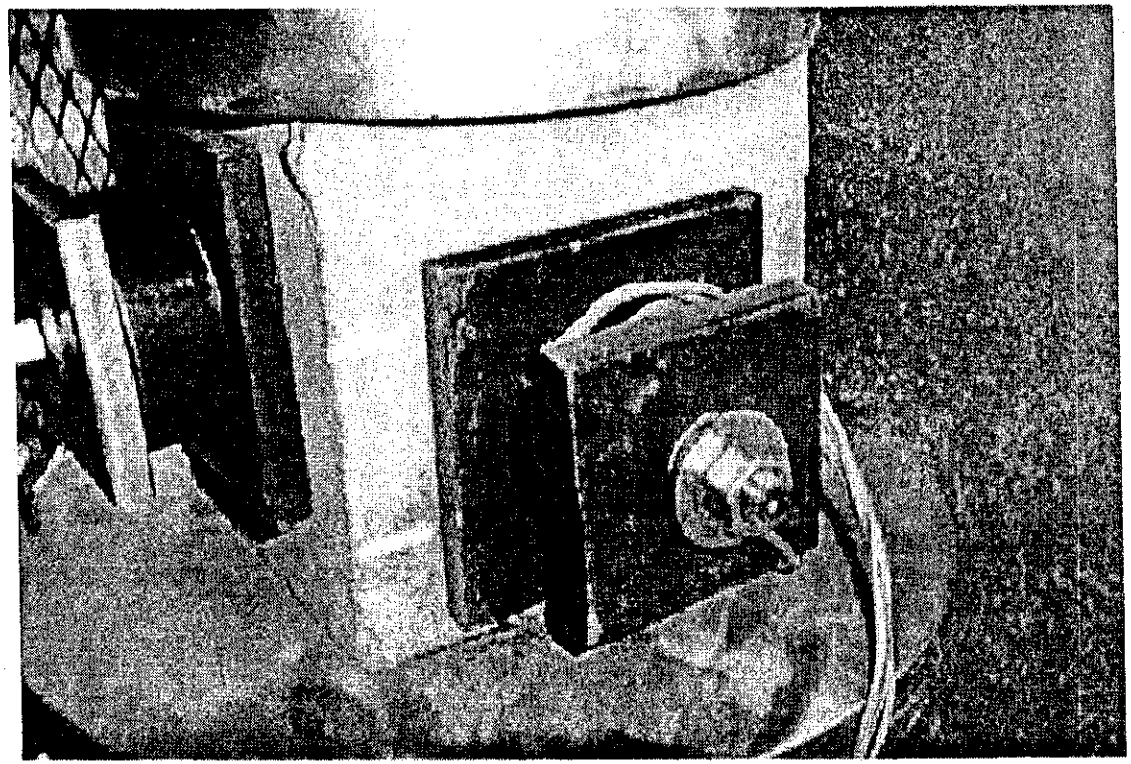

Figure 2-4: Test Setup for Cube

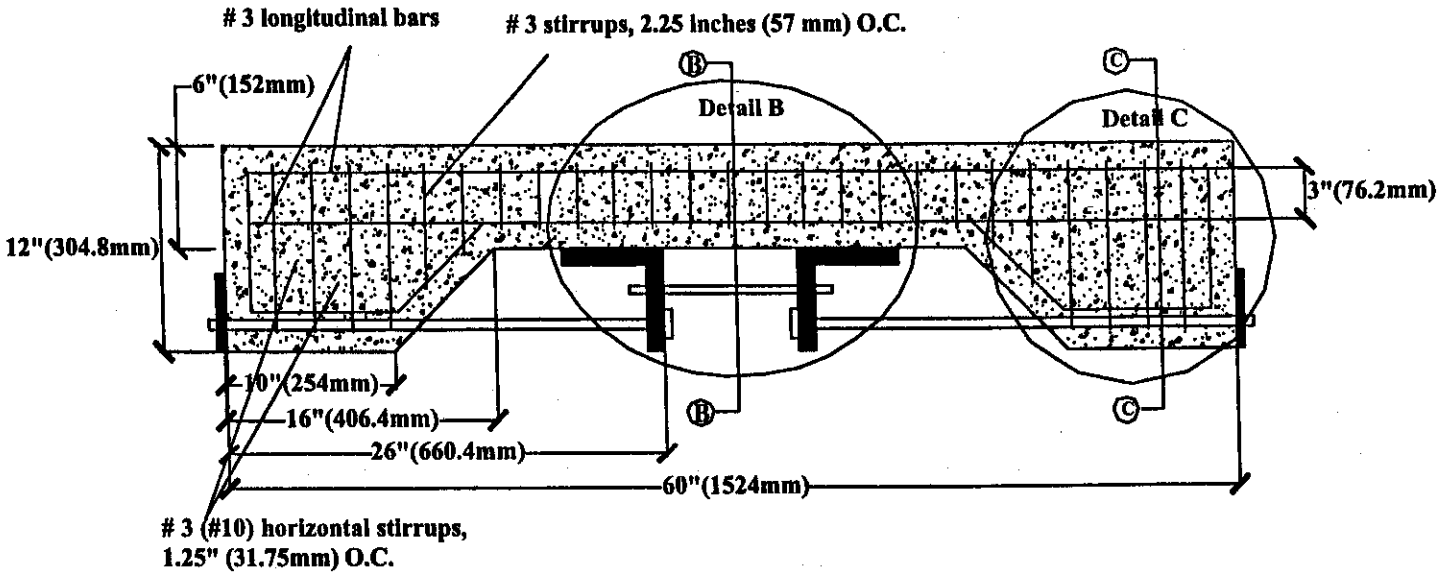

Figure 2-5: Beam Elevation

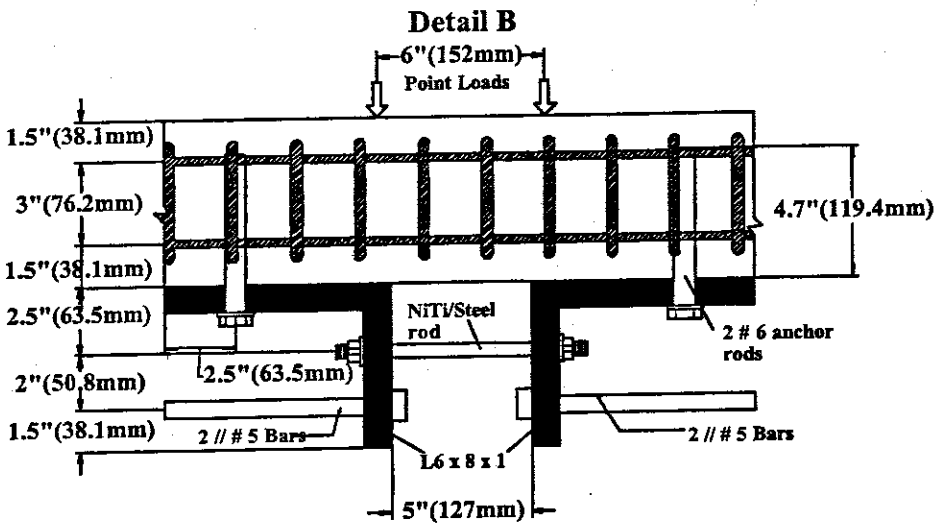

Figure 2-6: Beam Detail B

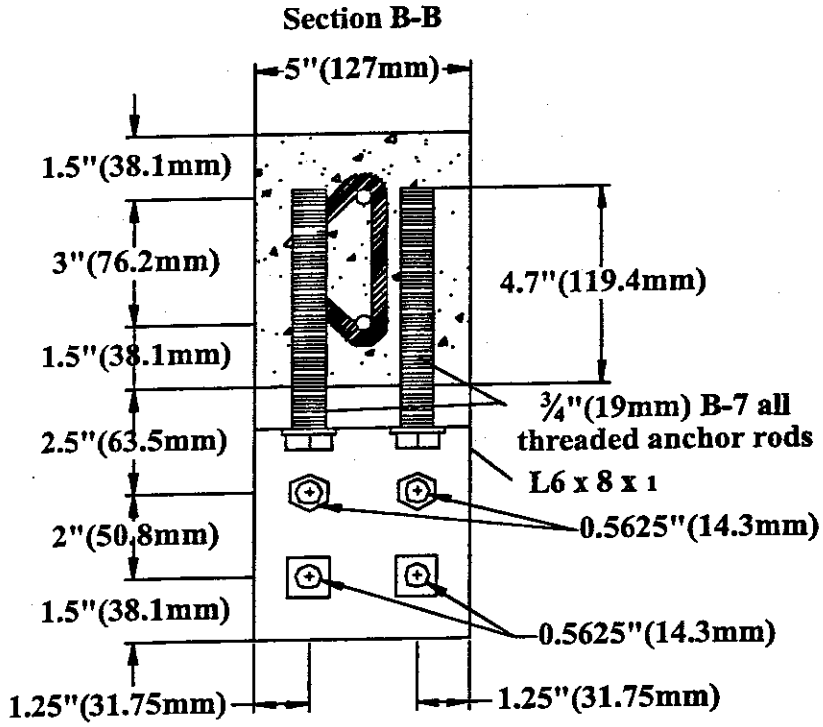

Figure 2-7: Beam Cross-Section B-B

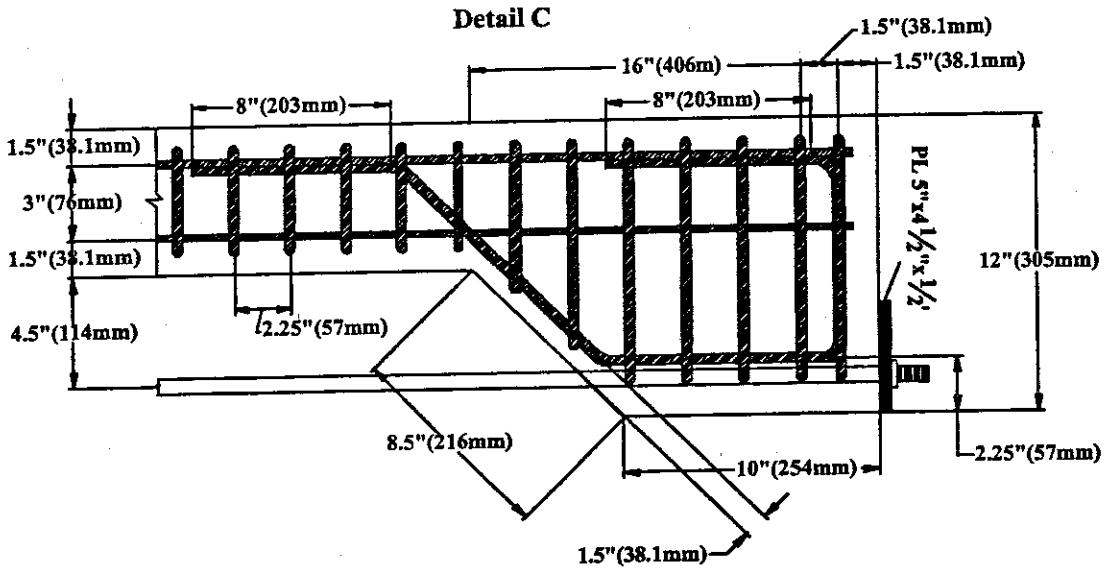

Figure 2-8: Beam Detail C

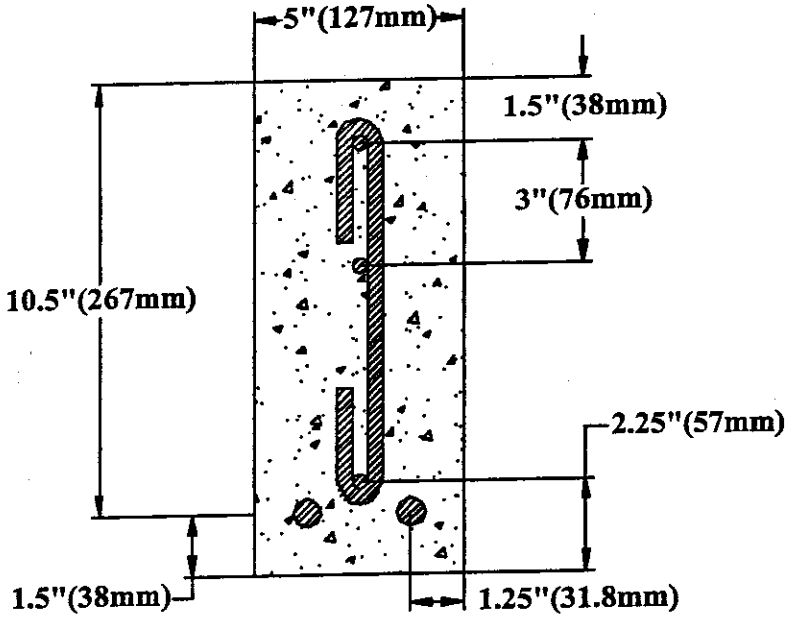

Figure 2-9: Beam Cross-Section C-C

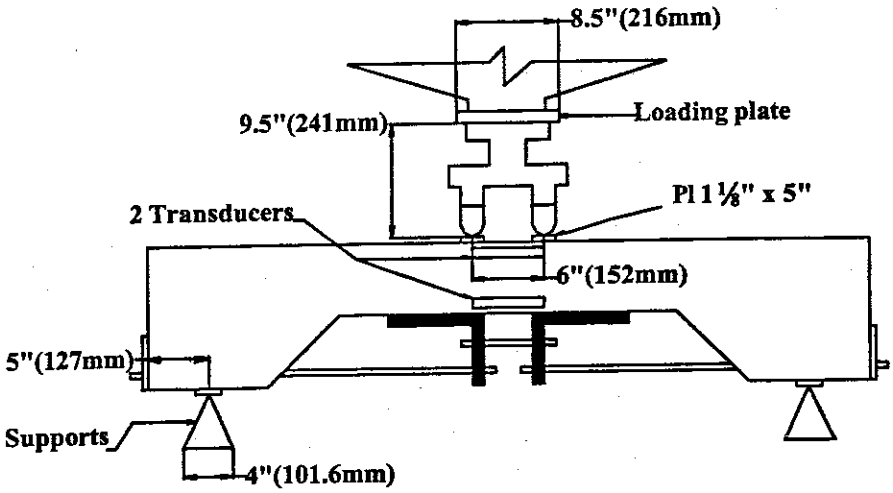

Figure 2-10: Beam Test Setup

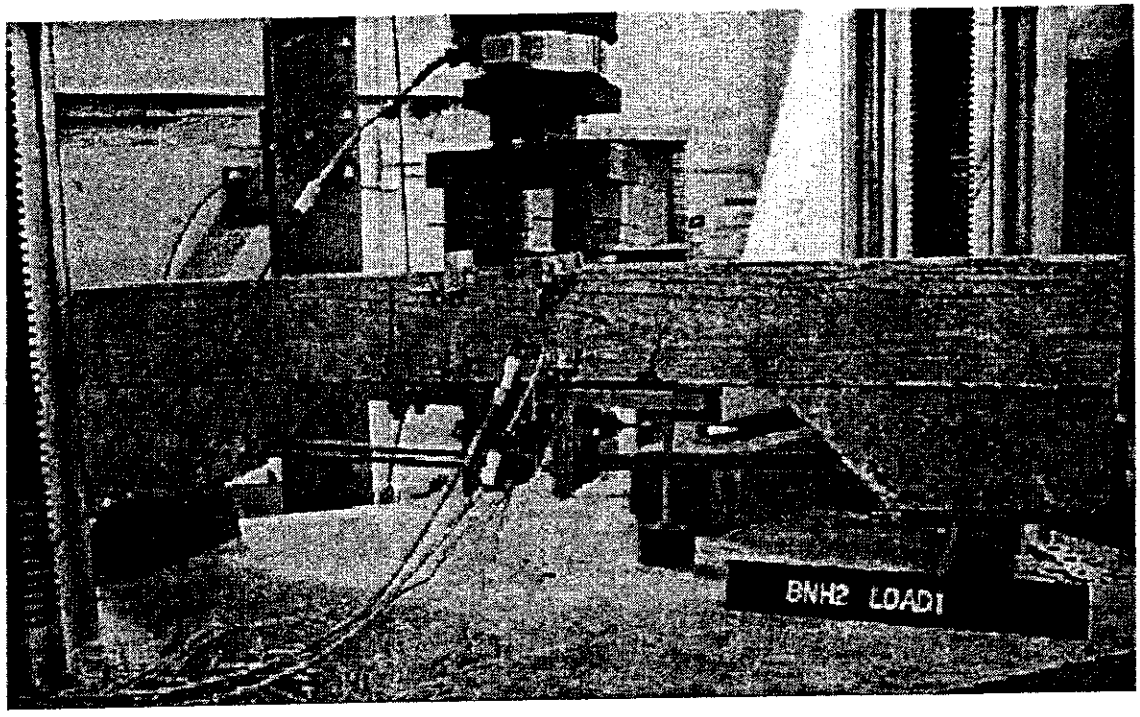

Figure 2-11: Test Setup of Specimen B-N-H-2

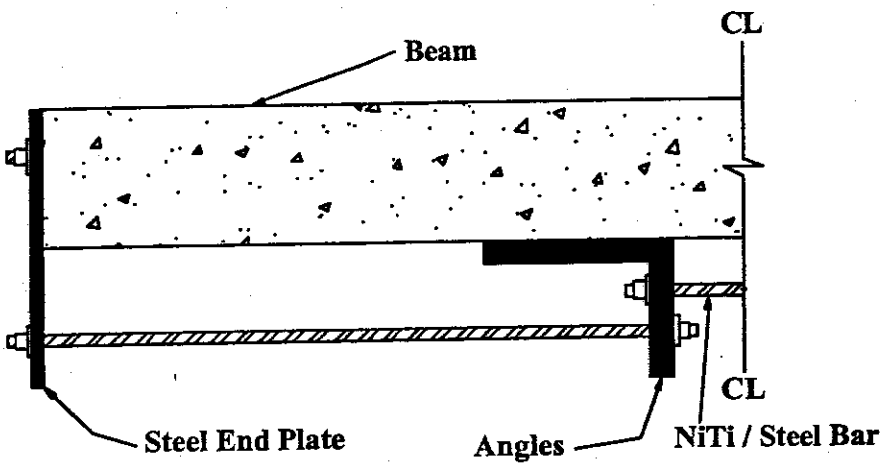

Figure 2-12: Initial Setup of Beam before Change

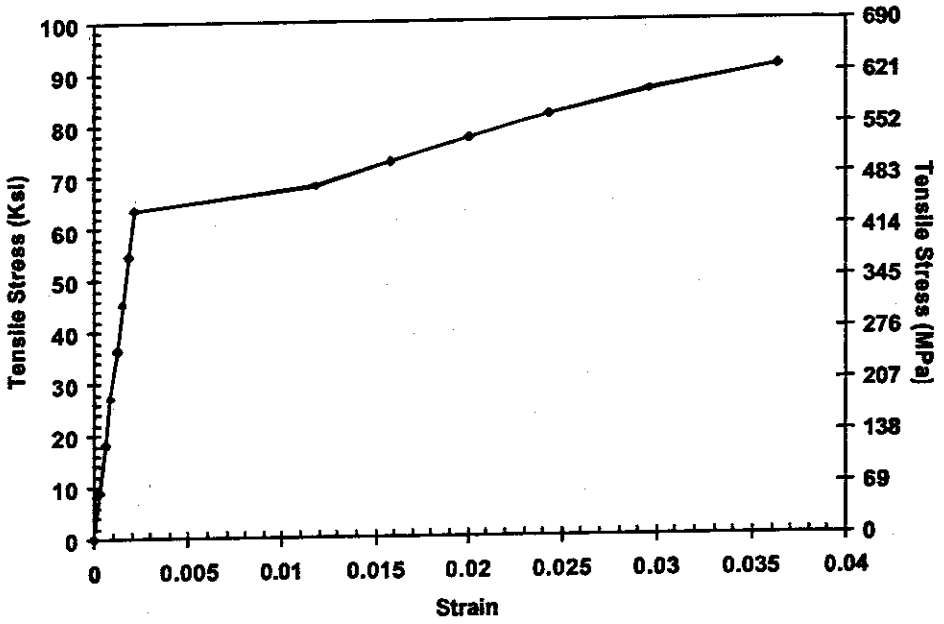

Figure 2-13: Measured Stress -Strain Relationship for #4 Bars

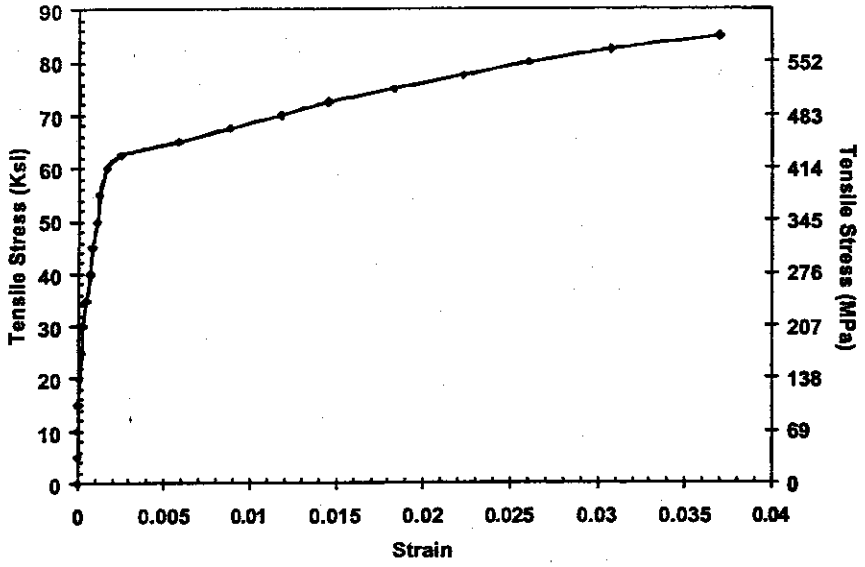

Figure 2-14: Measured Stress -Strain Relationship for #3 Bars

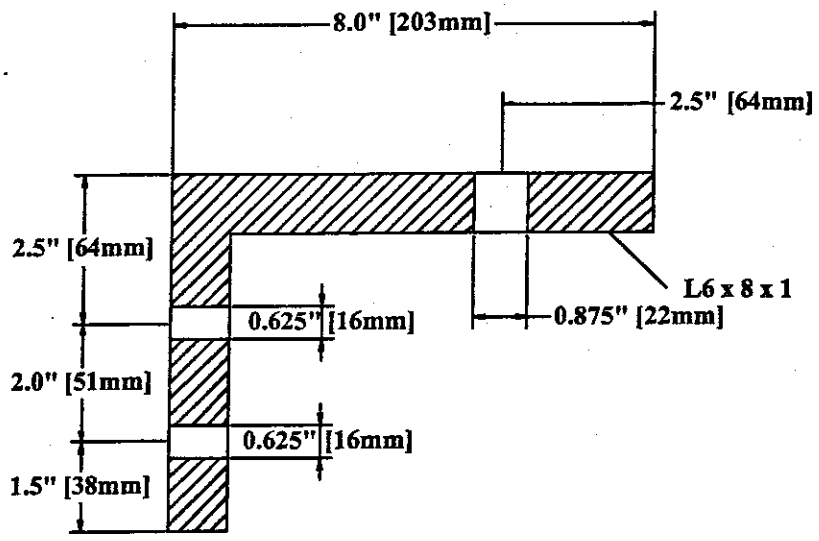

Figure 2-15: Angles Used in Double Reinforcement

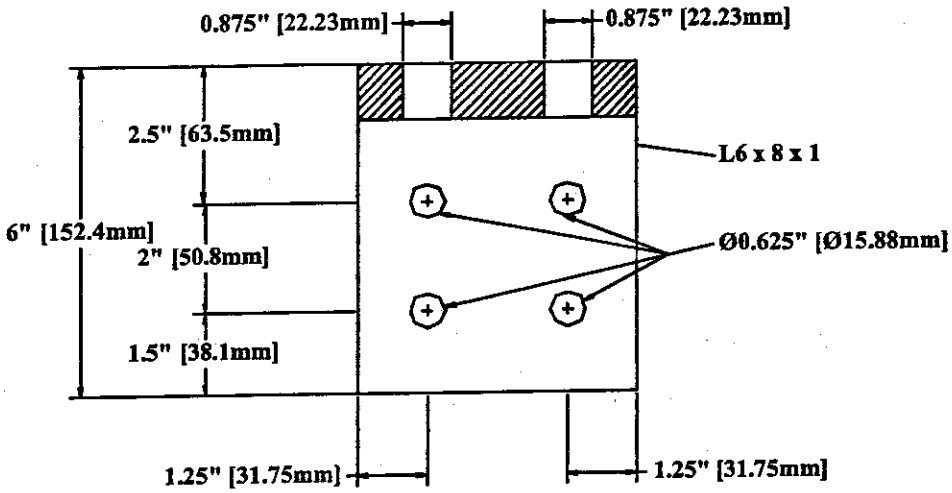

Figure 2-16: Angles Used in Double Reinforcement

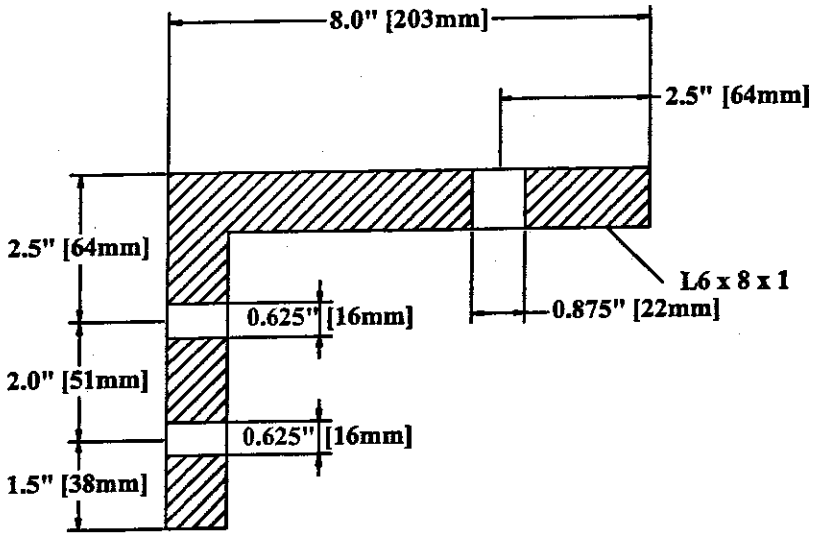

Figure 2-17: Angles Used in Single Reinforcement

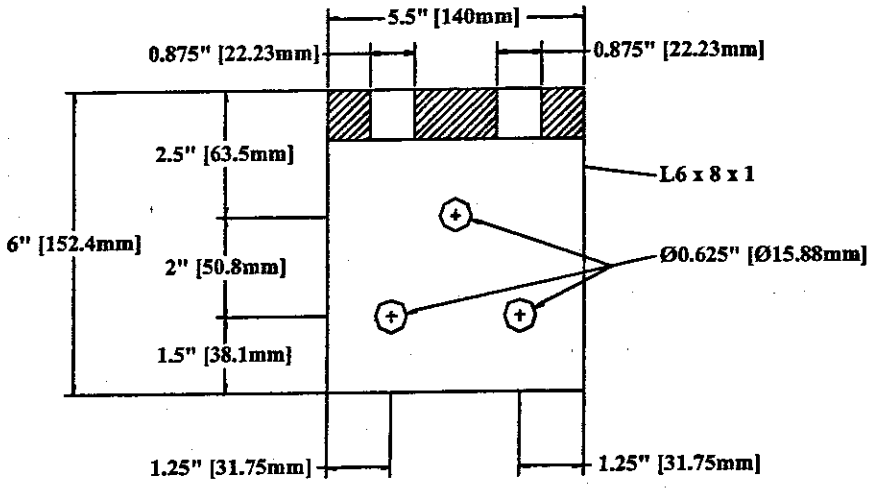

Figure 2-18: Angles Used in Single Reinforcement

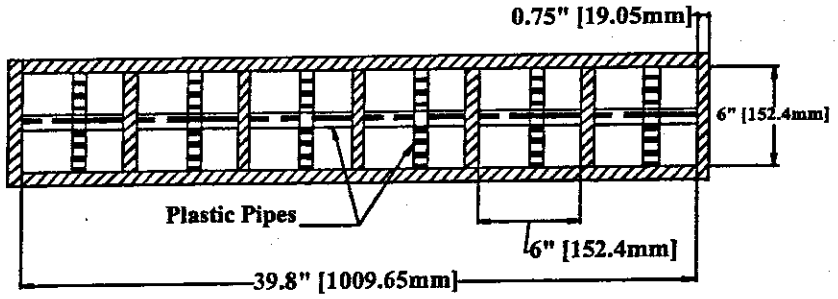

Figure 2-19: Plan View of Cube Form Work

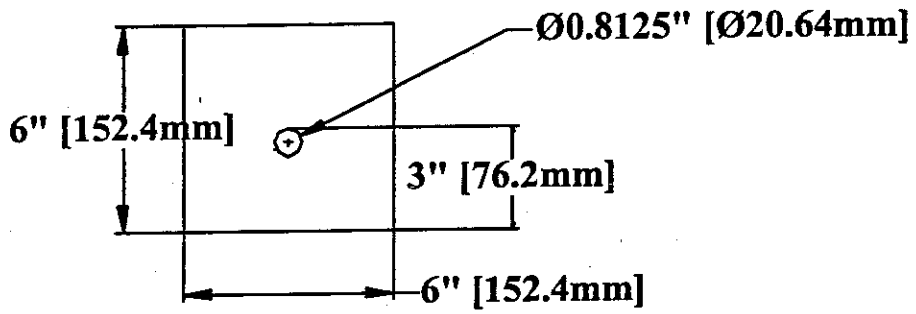

Figure 2-20: Small Piece for Cube Formwork Showing Dimensions and Hole Locations

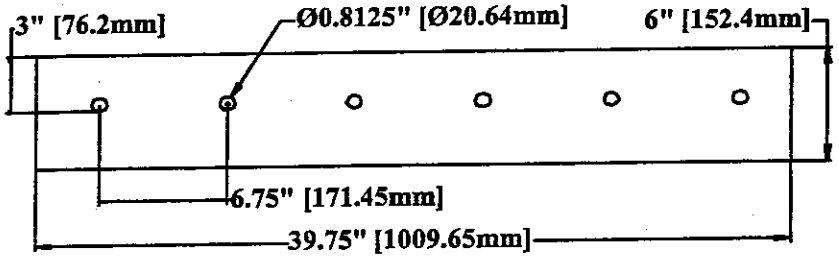

Figure 2-21: Long Piece for Cube Formwork Showing Dimensions and Hole Locations

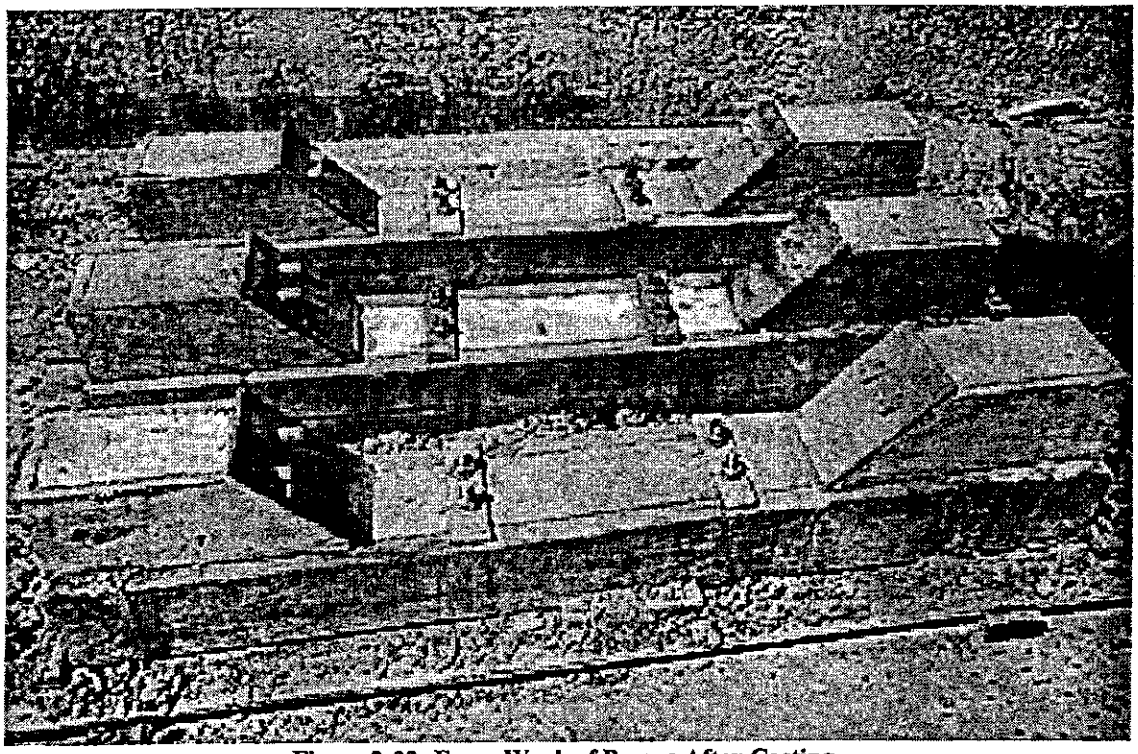

Figure 2-22: Form Work of Beams After Casting

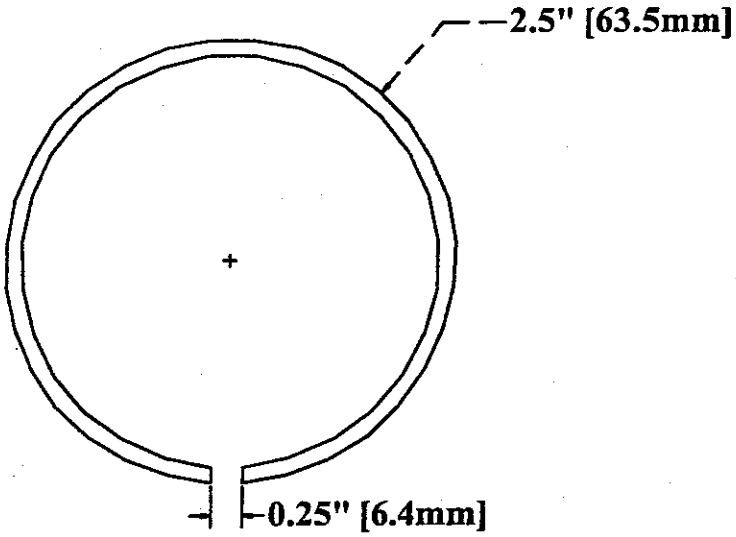

Figure 2-23: A36 - $2^1/_2$ " Pipe used with Cubes to Protect Strain Gages

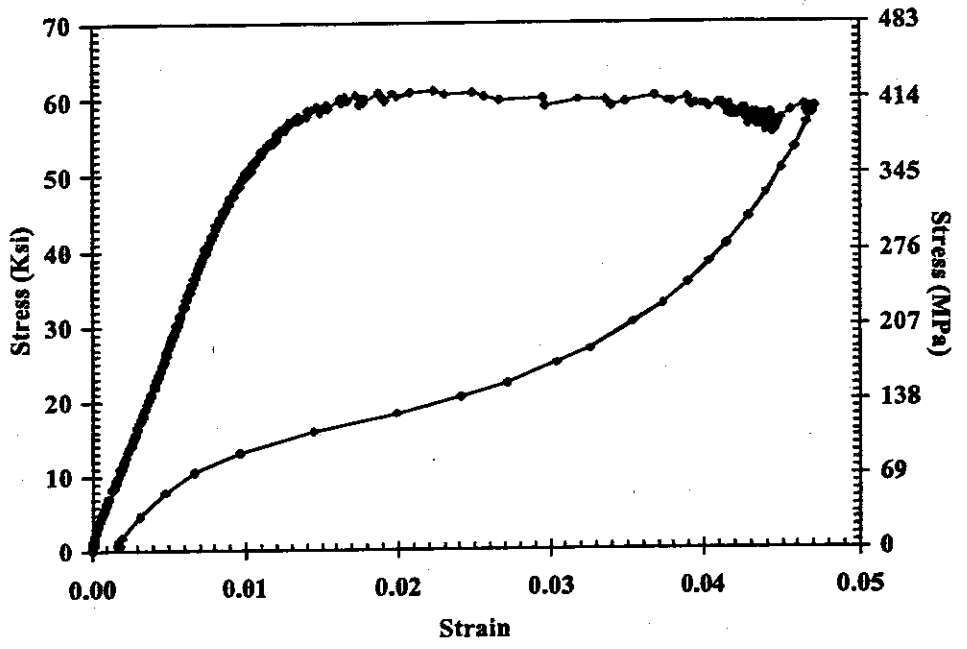

Figure 2-24: Stress-Strain Curve for 0.375-inch NiTi Rod

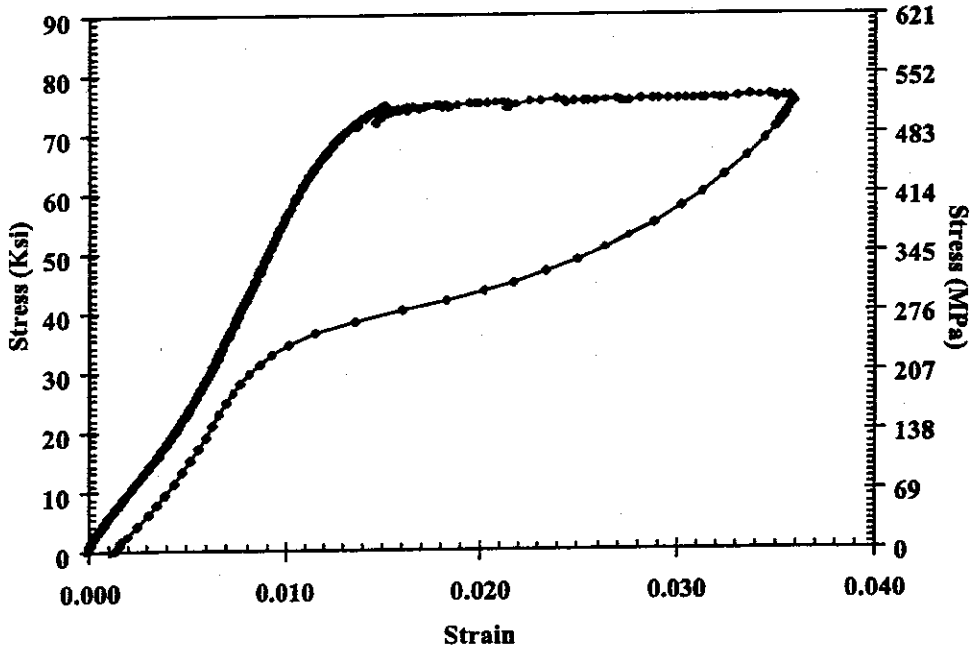

Figure 2-25: Stress-Strain Curve for 0.500-inch NiTi Rod

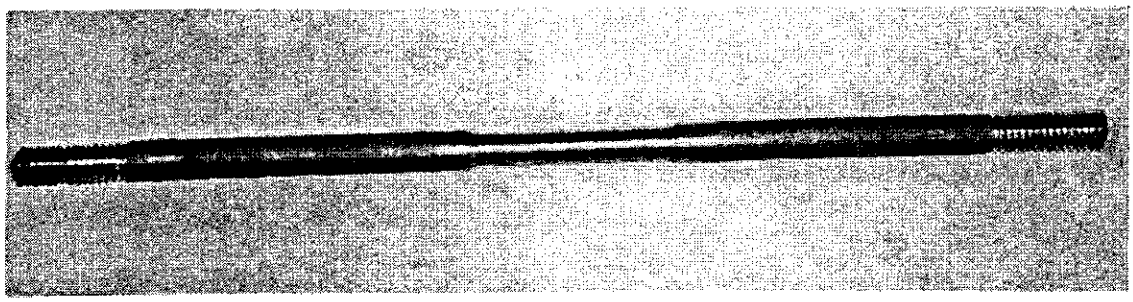

Figure 2-26: Reduced Section and Threads on 0.375-in NiTi Bar

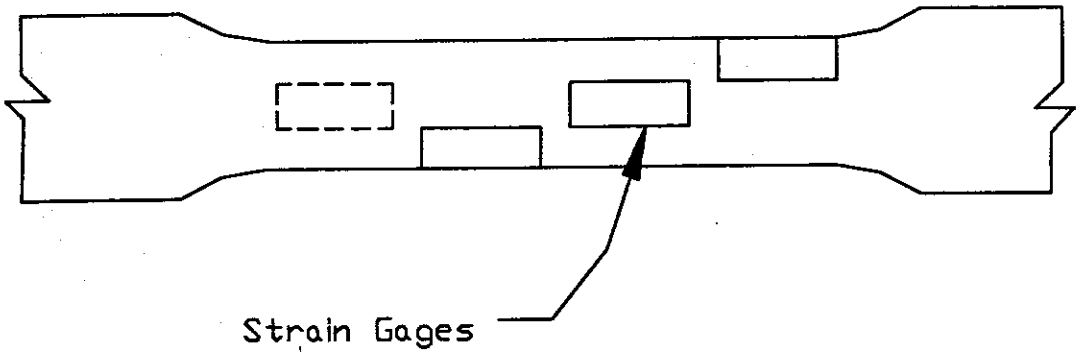

Figure 3-1: Staggered Locations of Strain Gages on Nitinol Bars

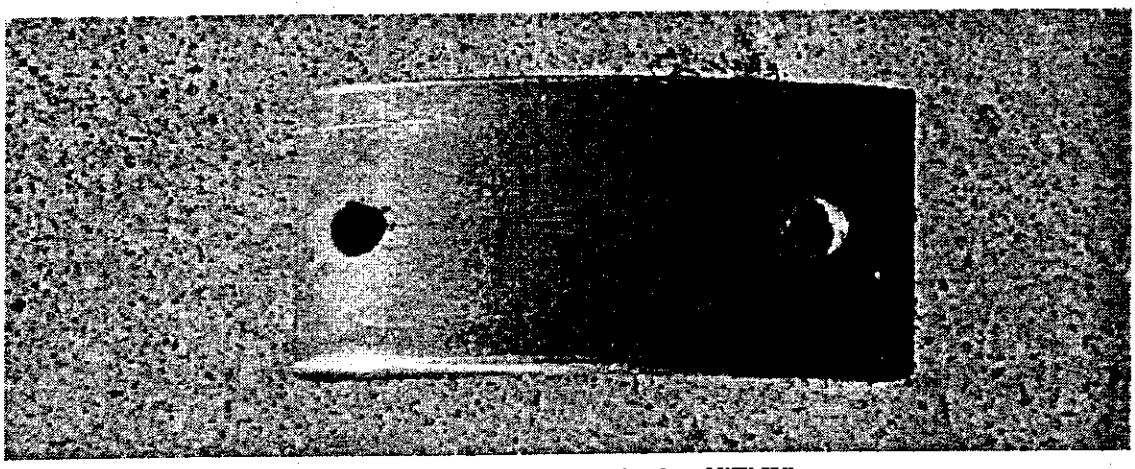

Figure 3-2: Steel Plate Used to Anchor NiTi Wires

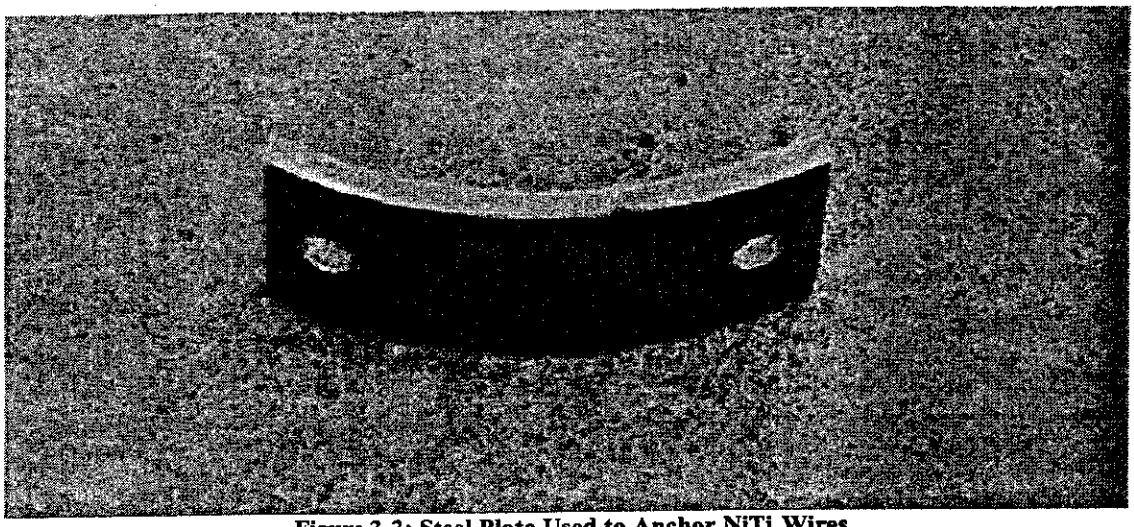

Figure 3-3: Steel Plate Used to Anchor NiTi Wires

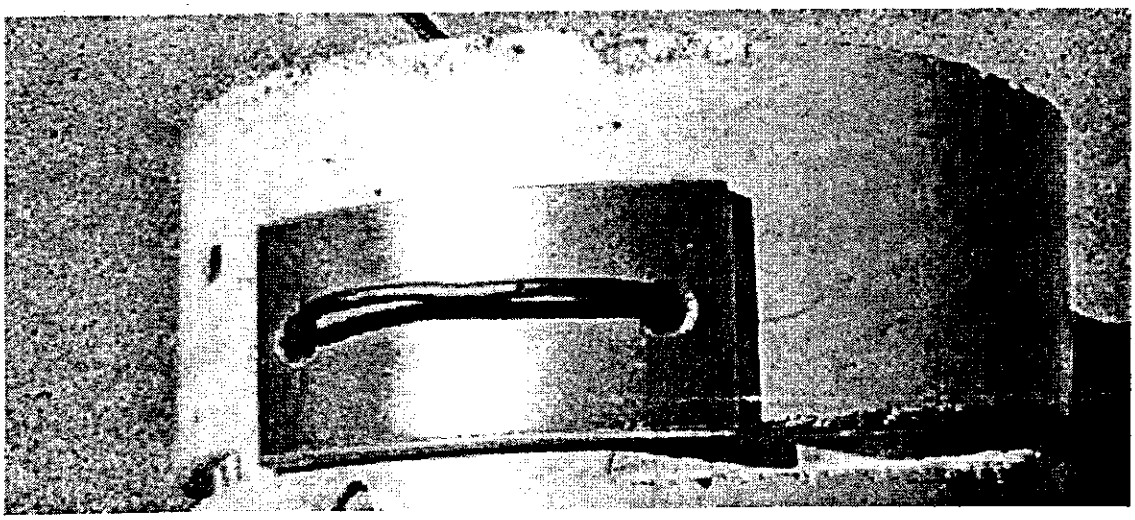

Figure 3-4: Anchorage Mechanism for NiTi Wires

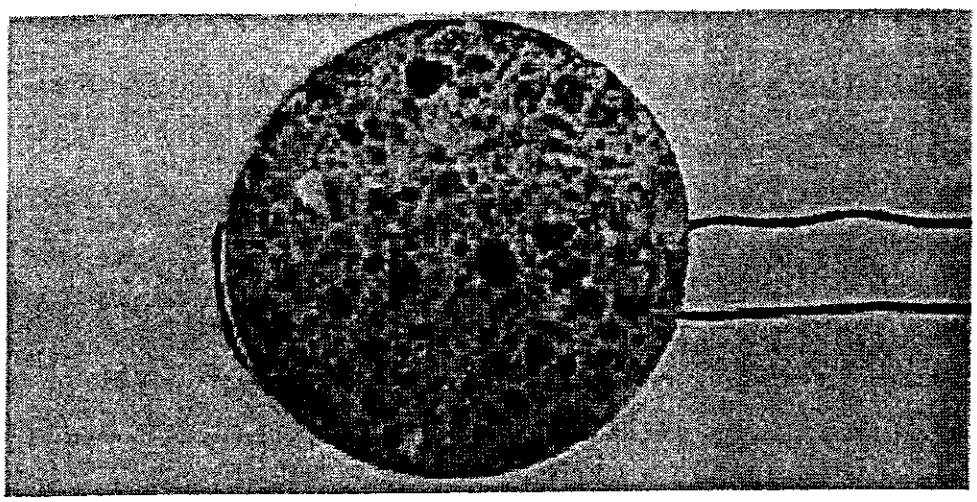

Figure 3-5: Plan of Anchorage Mechanism for NiTi Wires

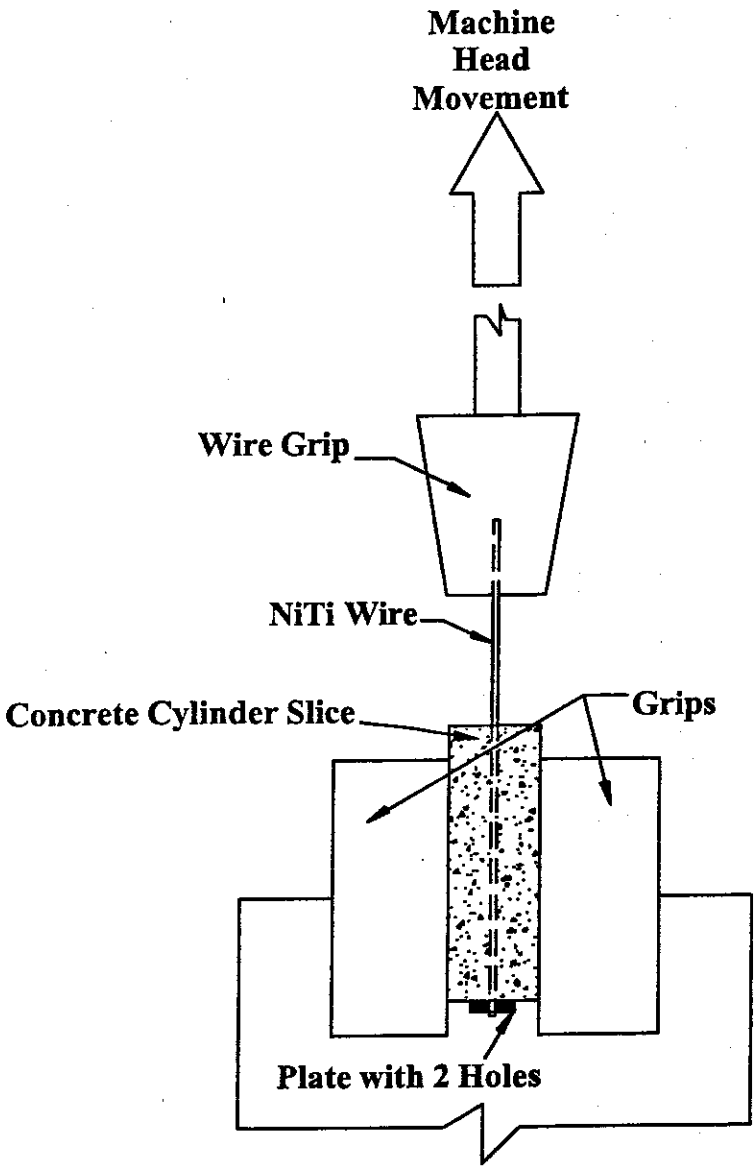

Figure 3-6: Wire Anchorage Test Setup

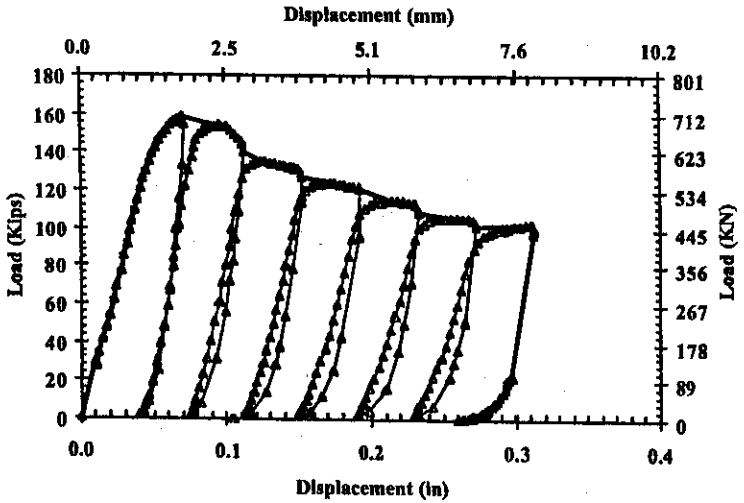

Figure 3-7: Load vs. Displacement Curve for C-N-H-1

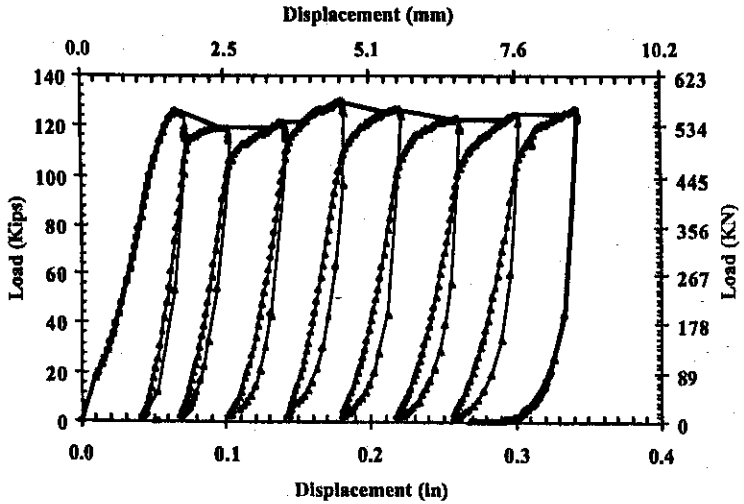

Figure 3-8: Load vs. Displacement Curve for C-N-H-2

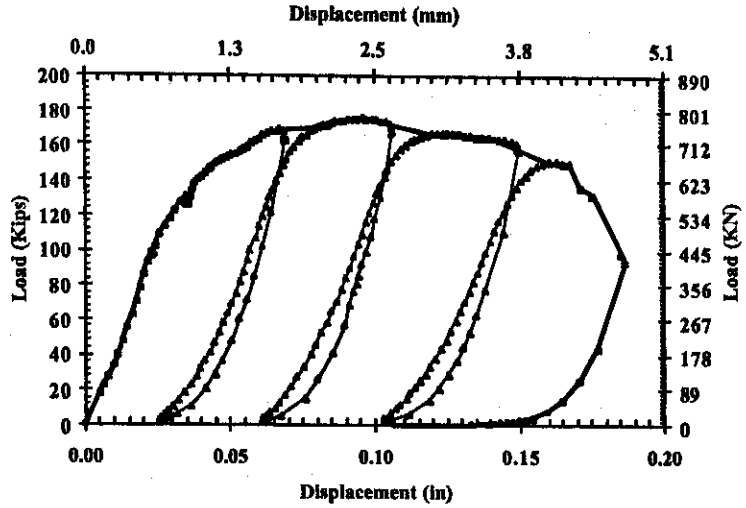

Figure 3-9: Load vs. Displacement Curve for C-S-L-1

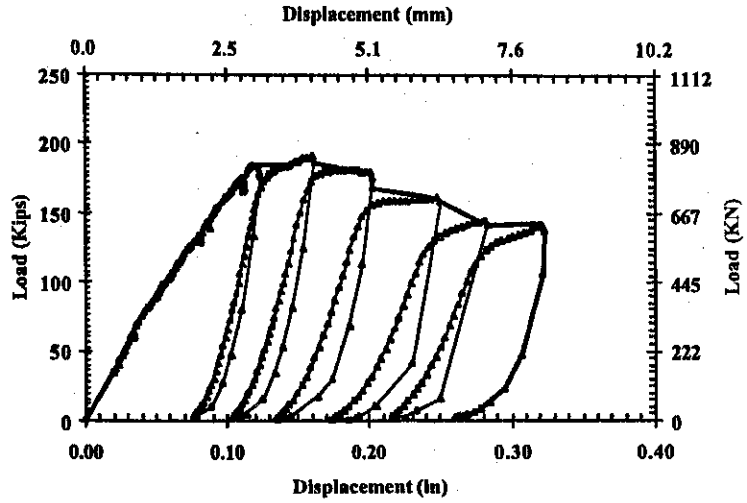

Figure 3-10: Load vs. Displacement Curve for C-S-L-2

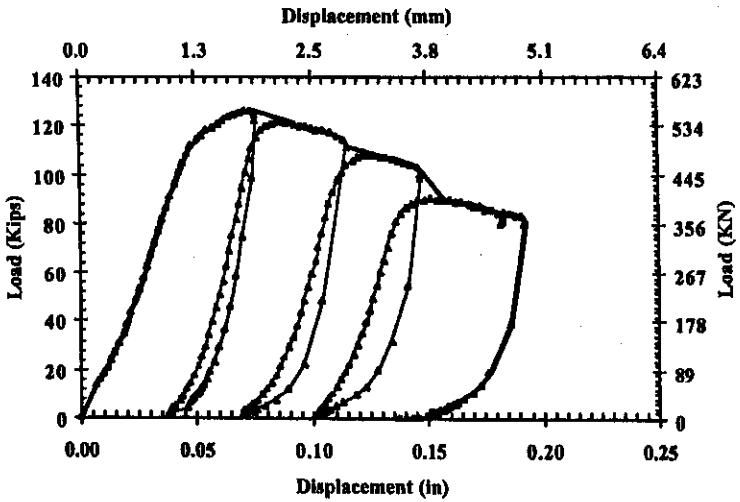

Figure 3-11: Load vs. Displacement Curve for C-N-L-1

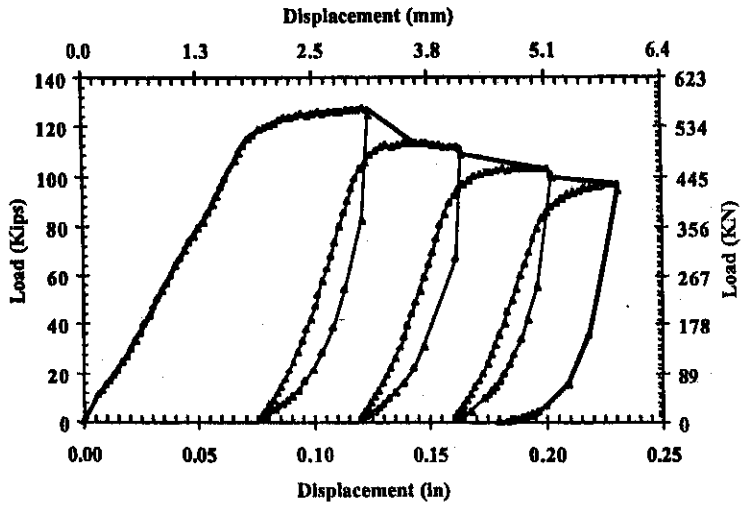

Figure 3-12: Load vs. Displacement Curve for C-N-L-2

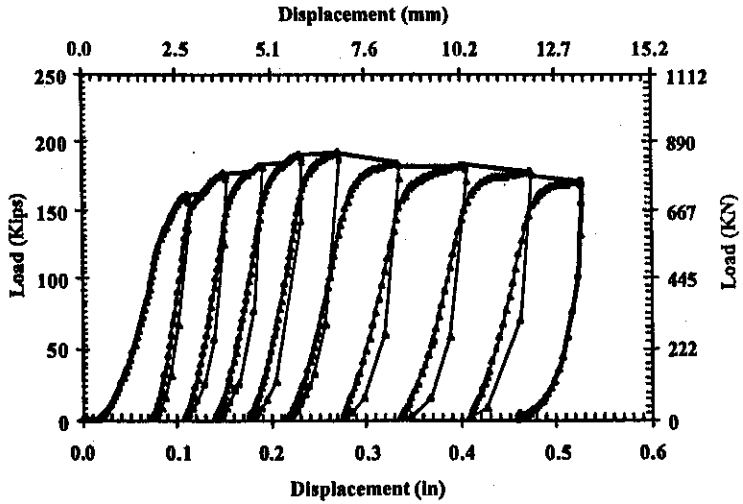

Figure 3-13: Load vs. Displacement Curve for C-S-H-2

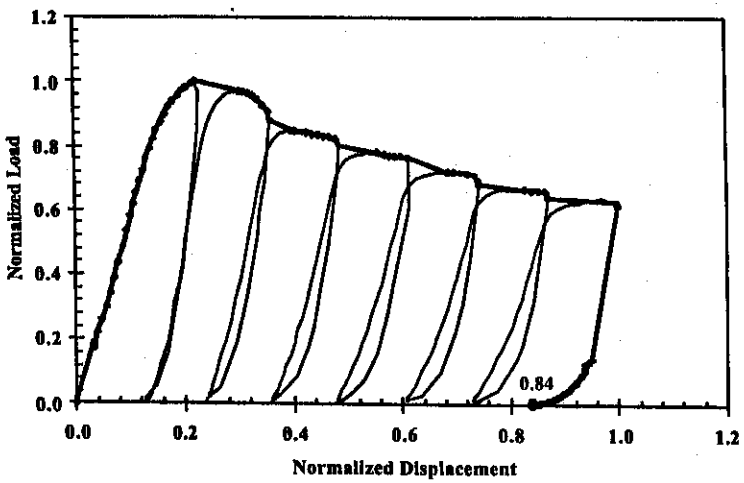

Figure 3-14: Normalized Load vs. Normalized Displacement for C-N-H-1

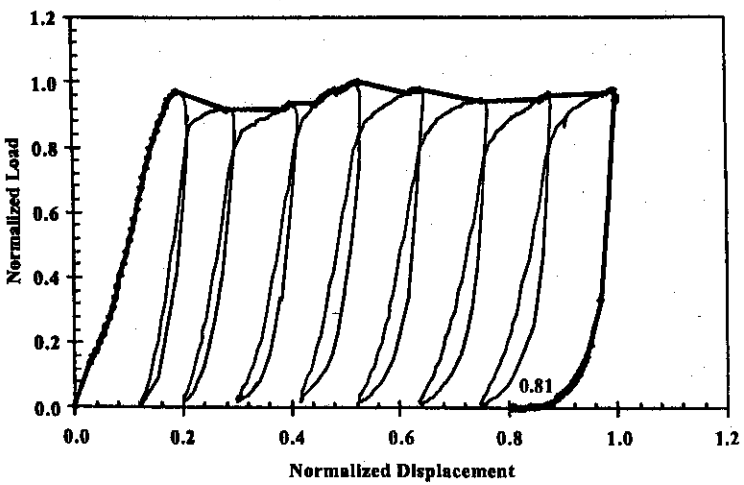

Figure 3-15: Normalized Load vs. Normalized Displacement for C-N-H-2

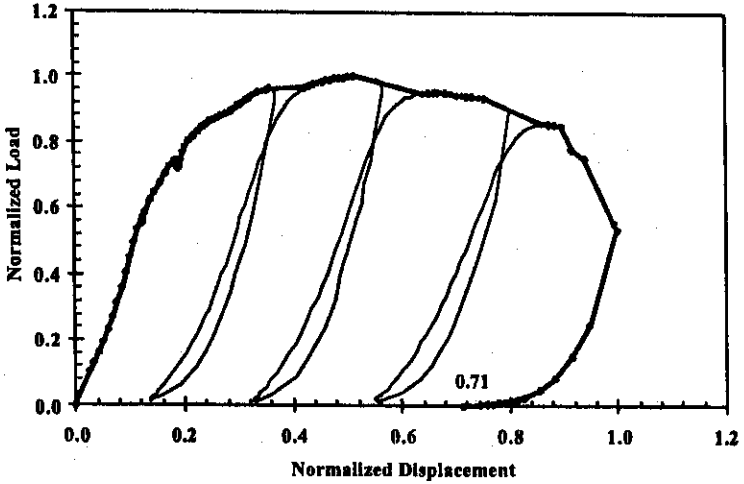

Figure 3-16: Normalized Load vs. Normalized Displacement for C-S-L-1

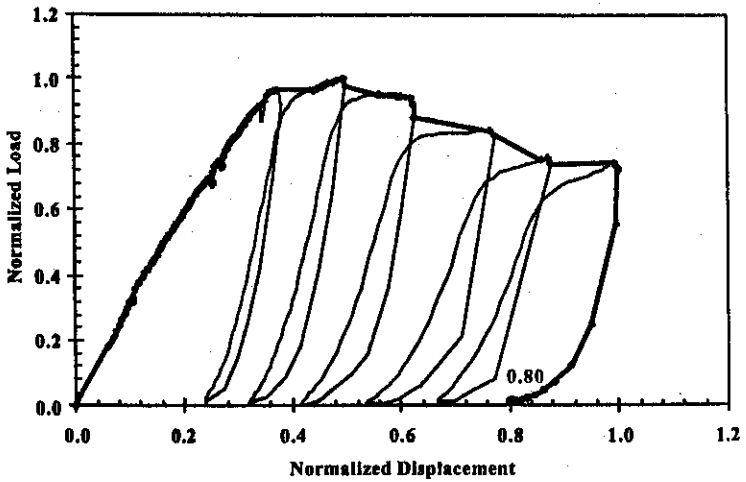

Figure 3-17: Normalized Load vs. Normalized Displacement for C-S-L-2

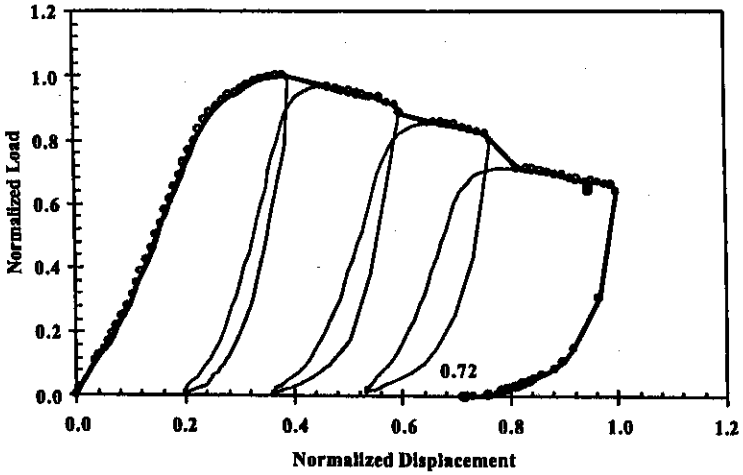

Figure 3-18: Normalized Load vs. Normalized Displacement for C-N-L-1

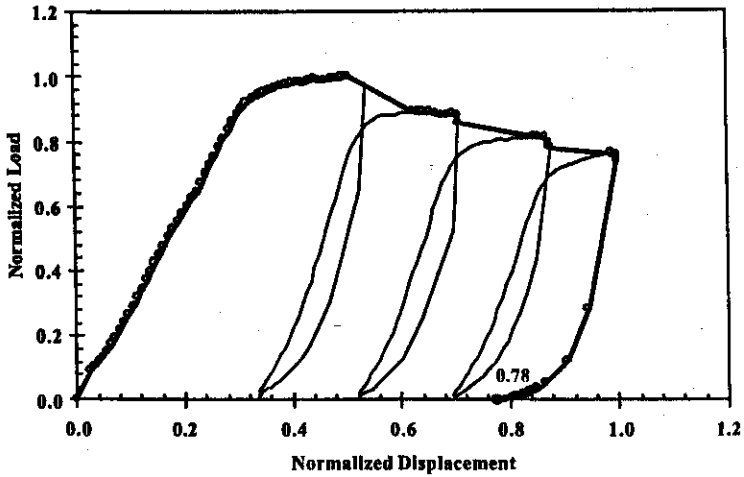

Figure 3-19: Normalized Load vs. Normalized Displacement for C-N-L-2

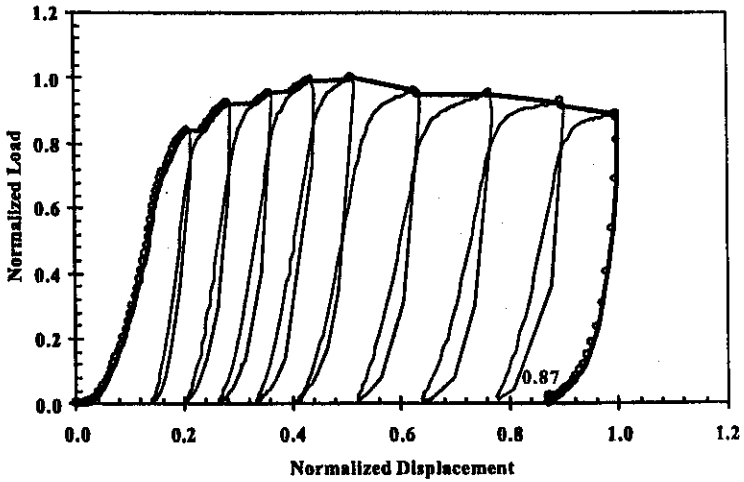

Figure 3-20: Normalized Load vs. Normalized Displacement for C-S-H-2

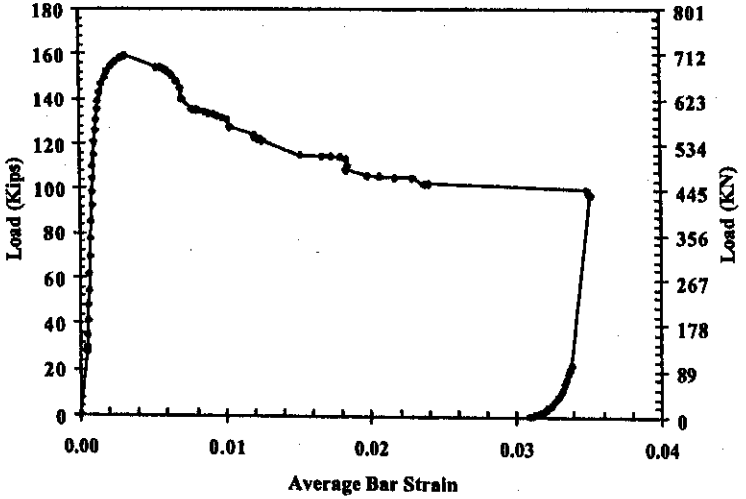

Figure 3-21: Load vs. Average Bar Strain for C-N-H-1

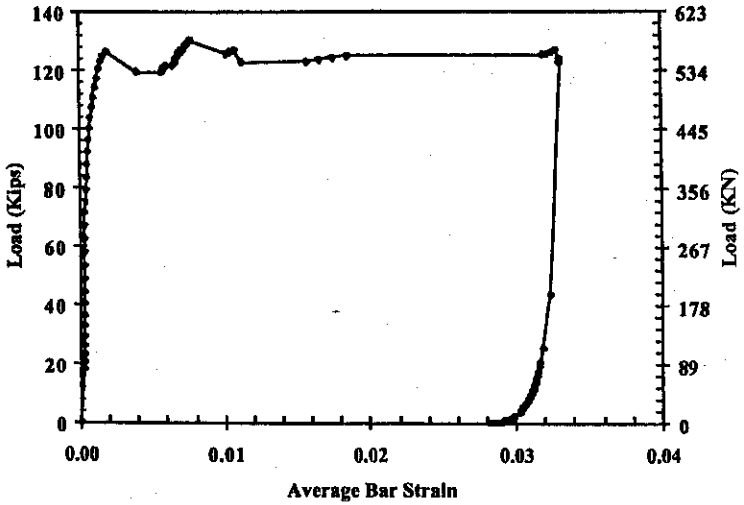

Figure 3-22: Load vs. Average Bar Strain for C-N-H-2

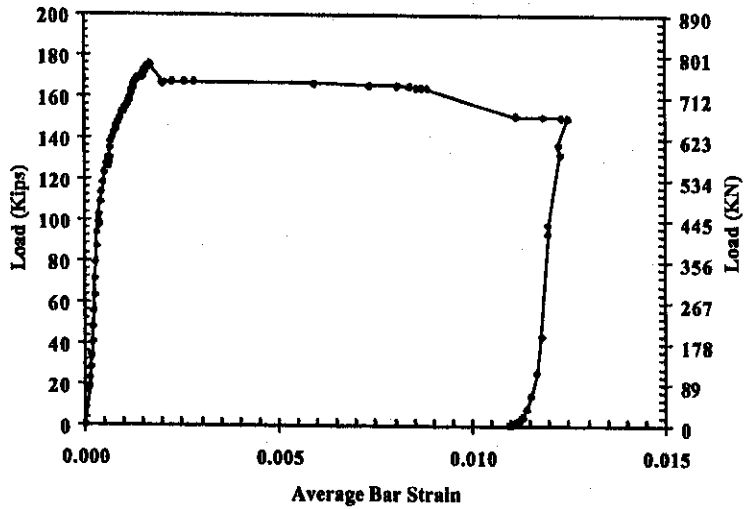

Figure 3-23: Load vs. Average Bar Strain for C-S-L-1

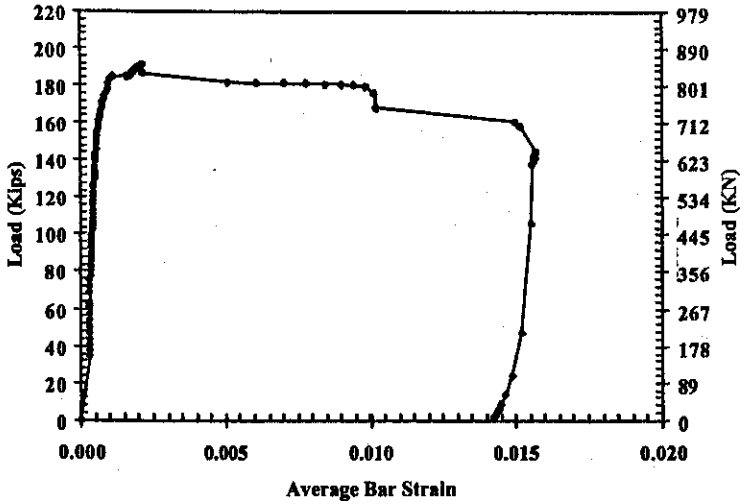

Figure 3-24: Load vs. Average Bar Strain for C-S-L-2

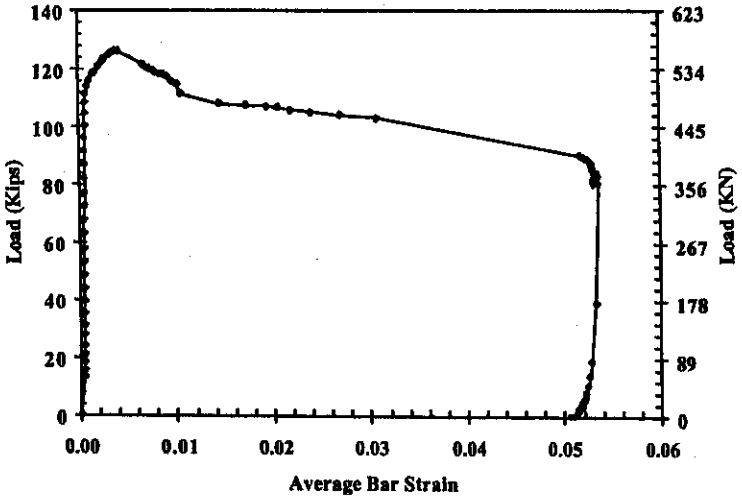

Figure 3-25: Load vs. Average Bar Strain for C-N-L-1

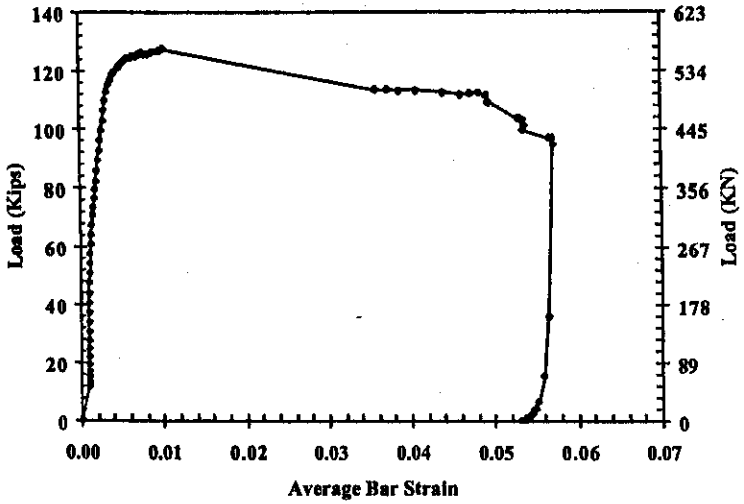

Figure 3-26: Load vs. Average Bar Strain for C-N-L-2

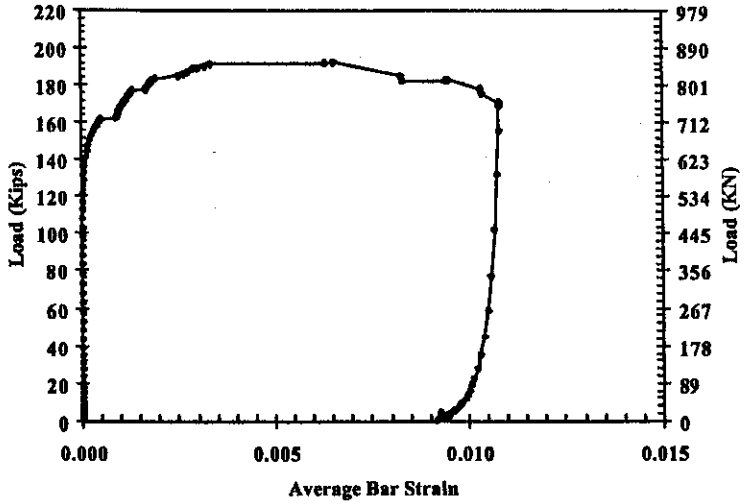

Figure 3-27: Load vs. Average Bar Strain for C-S-H-2

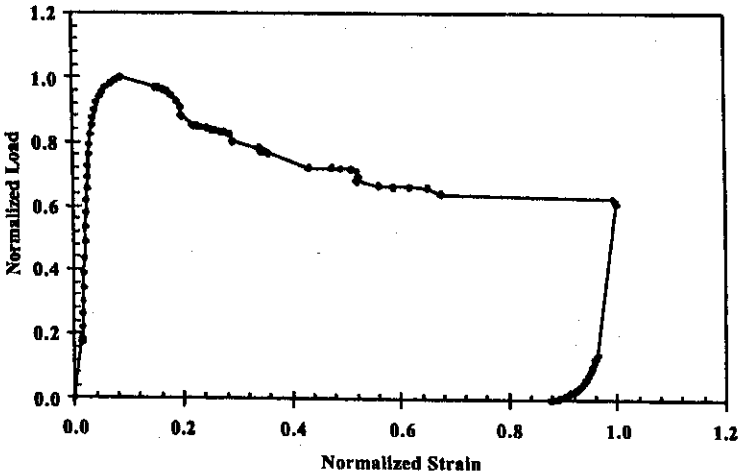

Figure 3-28: Normalized Load vs. Normalized Average Bars Strains for C-N-H-1

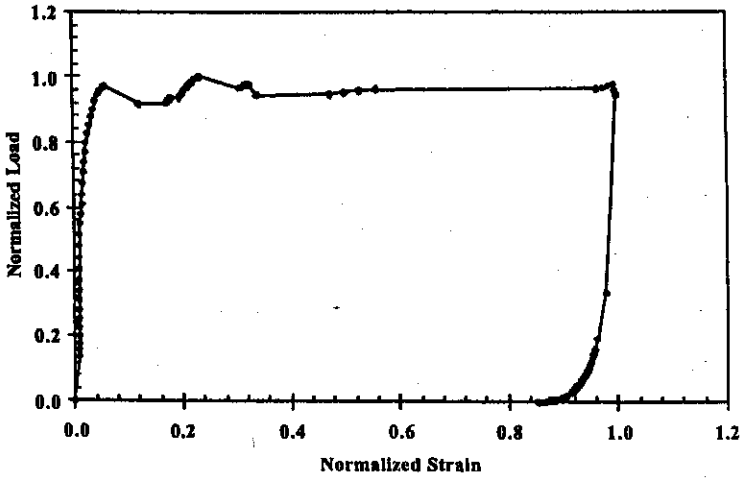

Figure 3-29: Normalized Load vs. Normalized Average Bars Strains for C-N-H-2

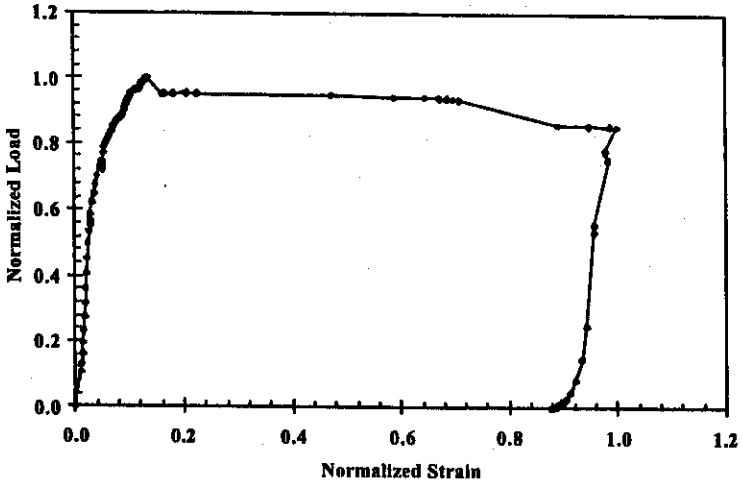

Figure 3-30: Normalized Load vs. Normalized Average Bars Strains for C-S-L-1

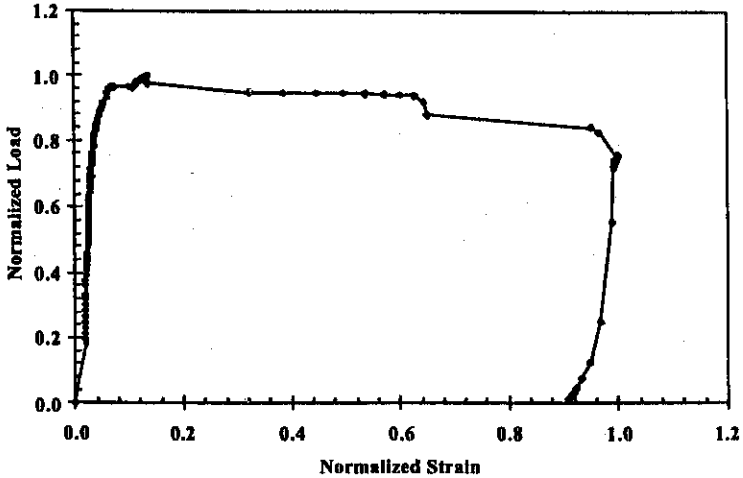

Figure 3-31: Normalized Load vs. Normalized Average Bars Strains for C-S-L-2

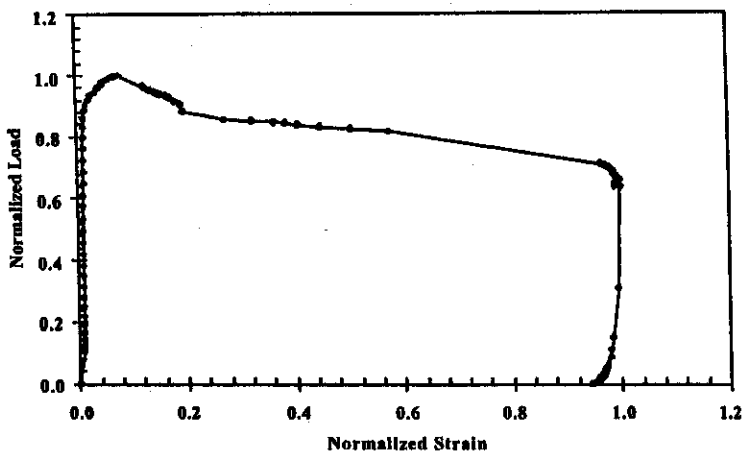

Figure 3-32: Normalized Load vs. Normalized Average Bars Strains for C-N-L-1

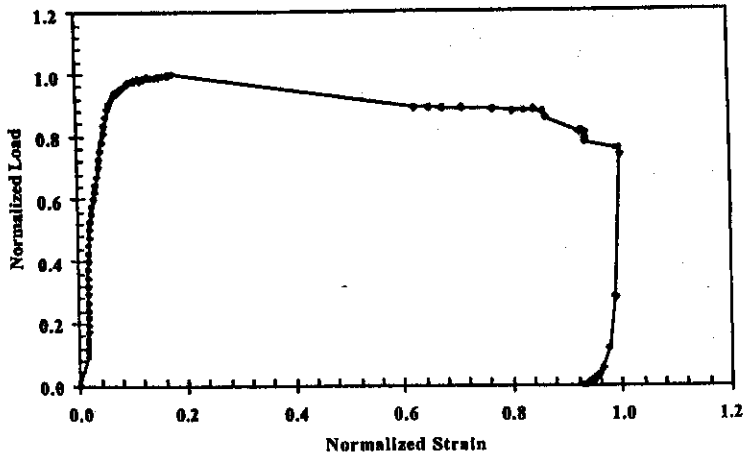

Figure 3-33: Normalized Load vs. Normalized Average Bars Strains for C-N-L-2

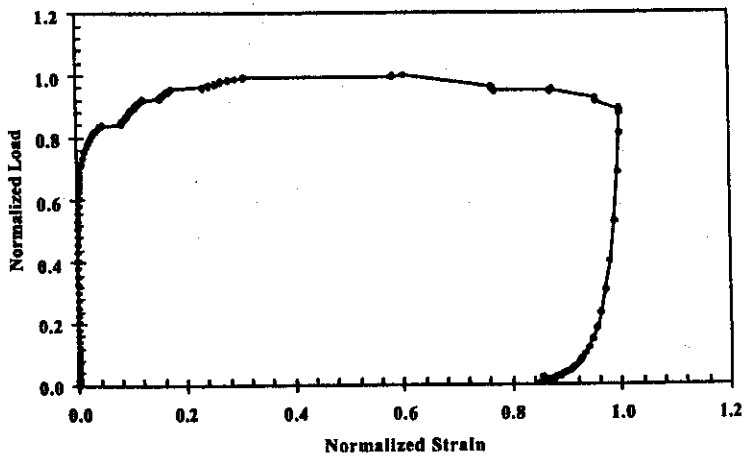

Figure 3-34: Normalized Load vs. Normalized Average Bars Strains for C-S-H-2

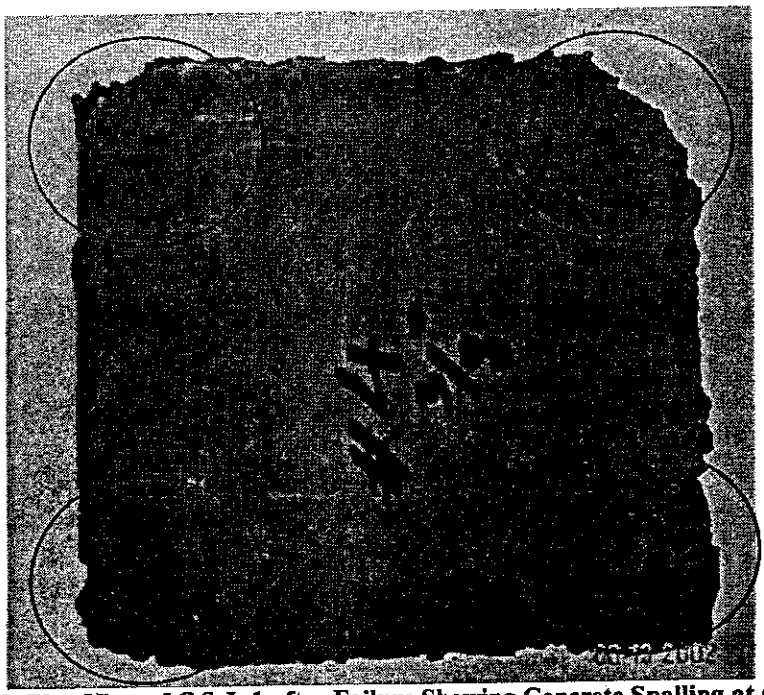

Figure 3-35: Plan View of C-S-L-1 after Failure Showing Concrete Spalling at Corners

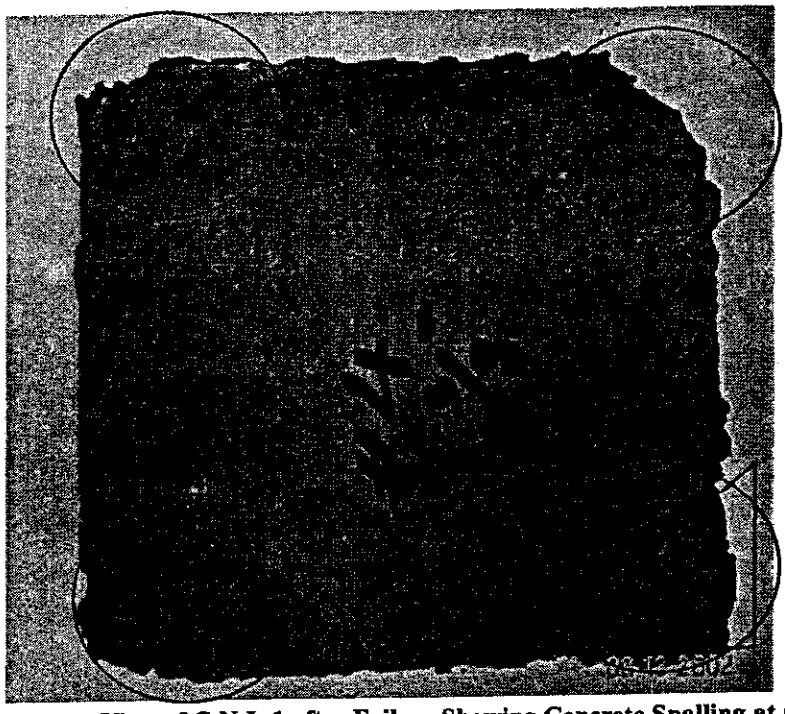

Figure 3-36: Plan View of C-N-L-1 after Failure Showing Concrete Spalling at Corners

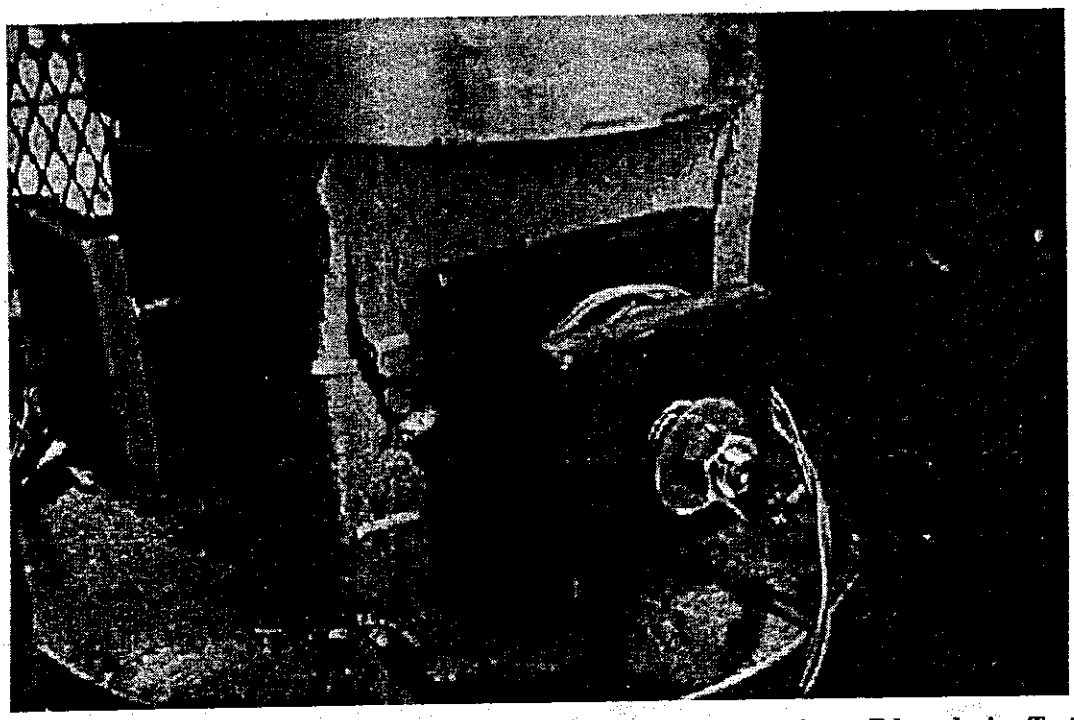

Figure 3-37: Picture Showing Early Stages of Concrete Spalling Occurring at Edges during Test

Figure 3-38: Picture Showing Final Stage of Concrete Spalling Occurring at Edges at End of Test

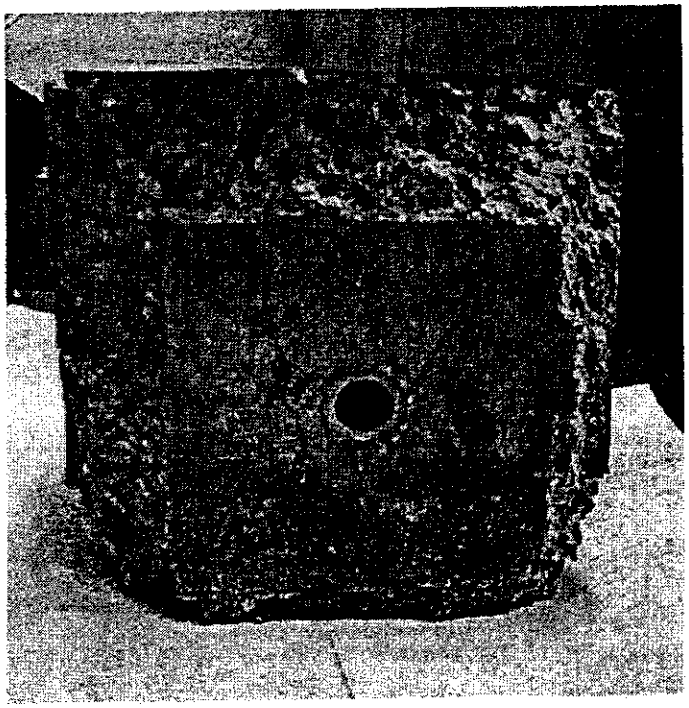

Figure 3-39: Picture Showing Spalling of Concrete at Edges

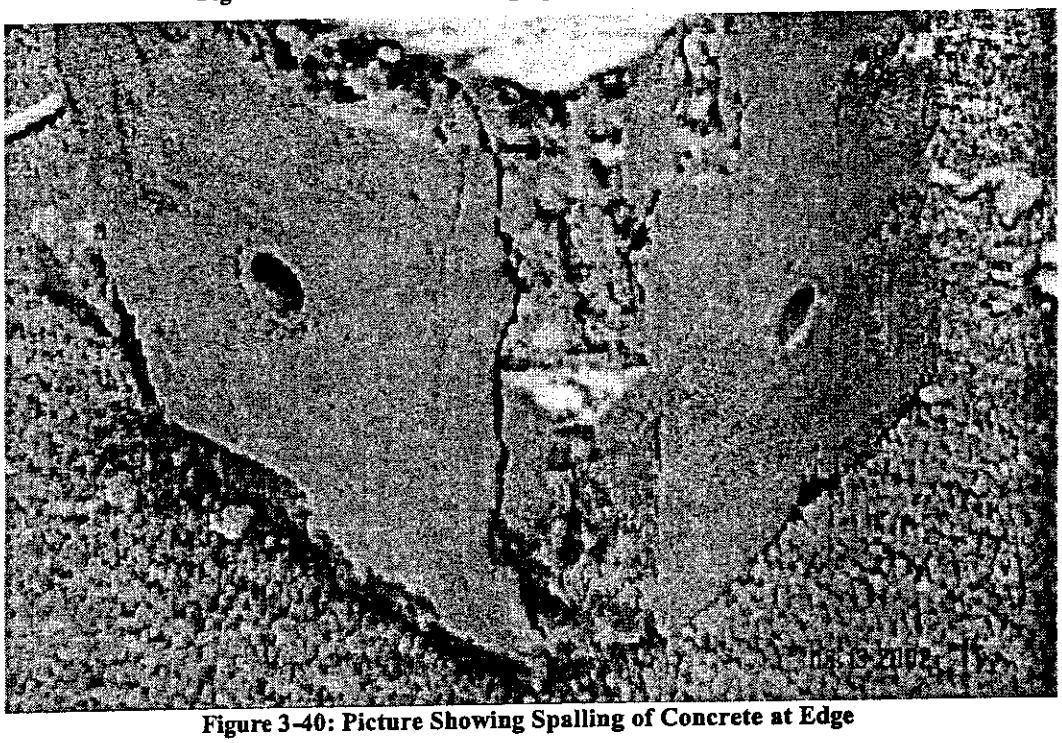

Figure 3-40: Picture Showing Spalling of Concrete at Edge

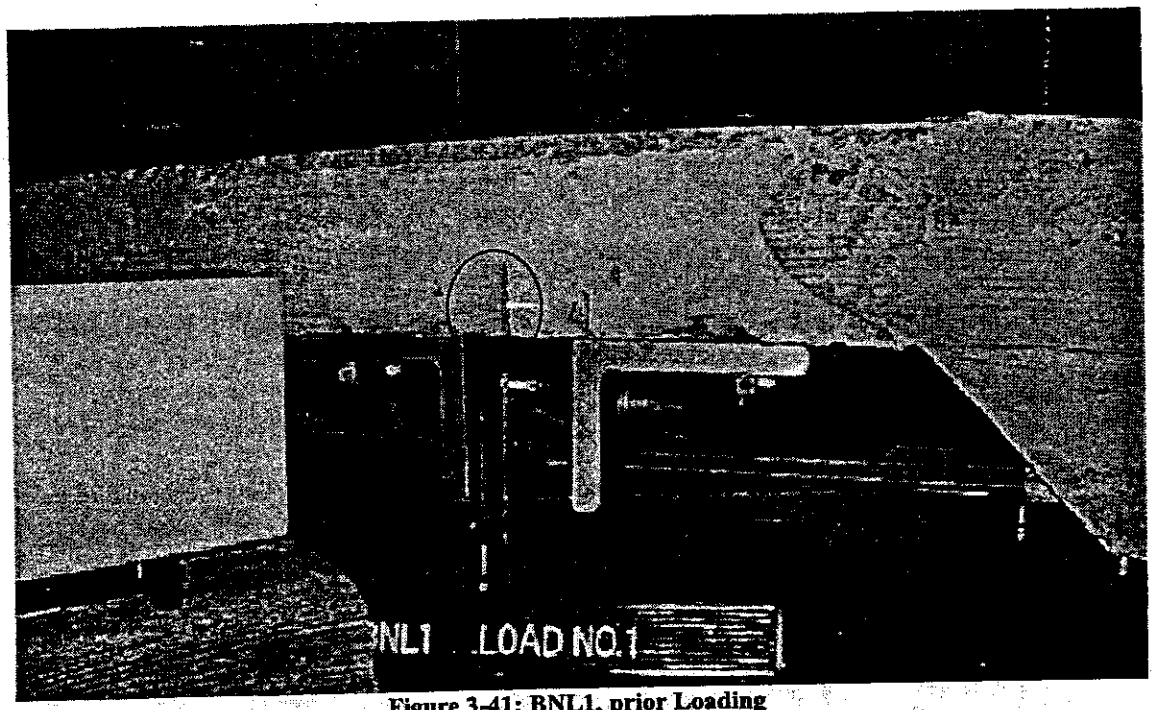

Figure 3-41: BNL1, prior Loading

Figure 3-42: BNL1, after Load Cycle 3

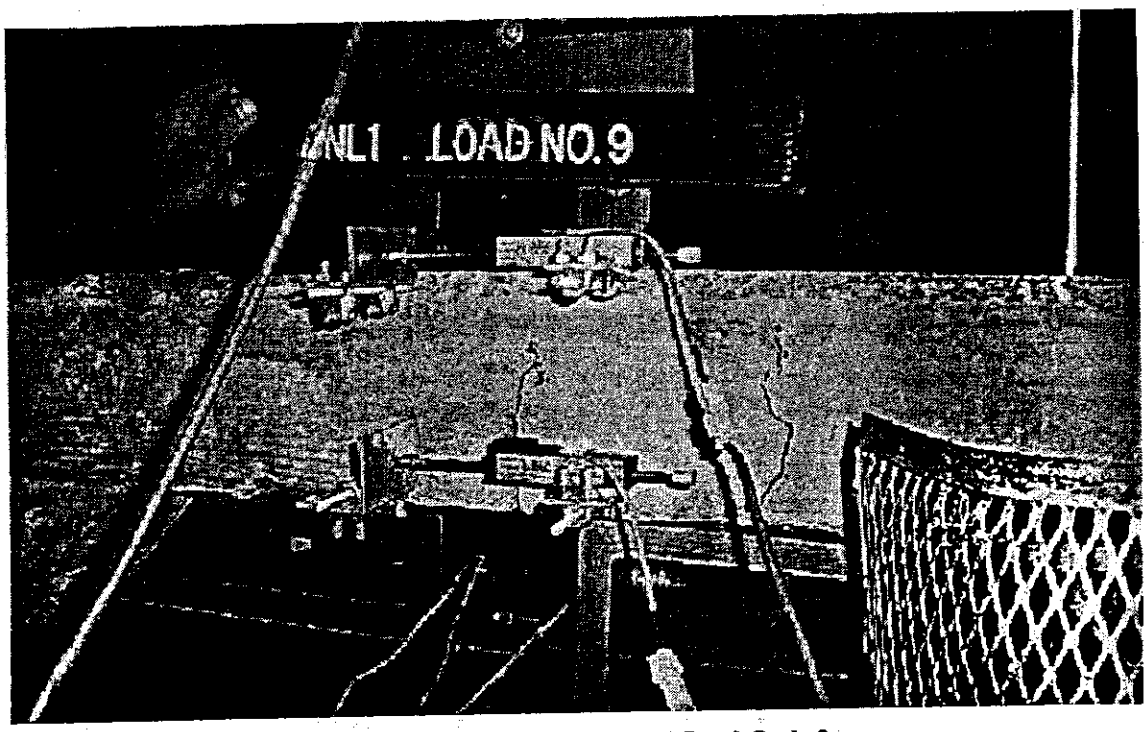

Figure 3-43: BNL1, after Final Load Cycle 9

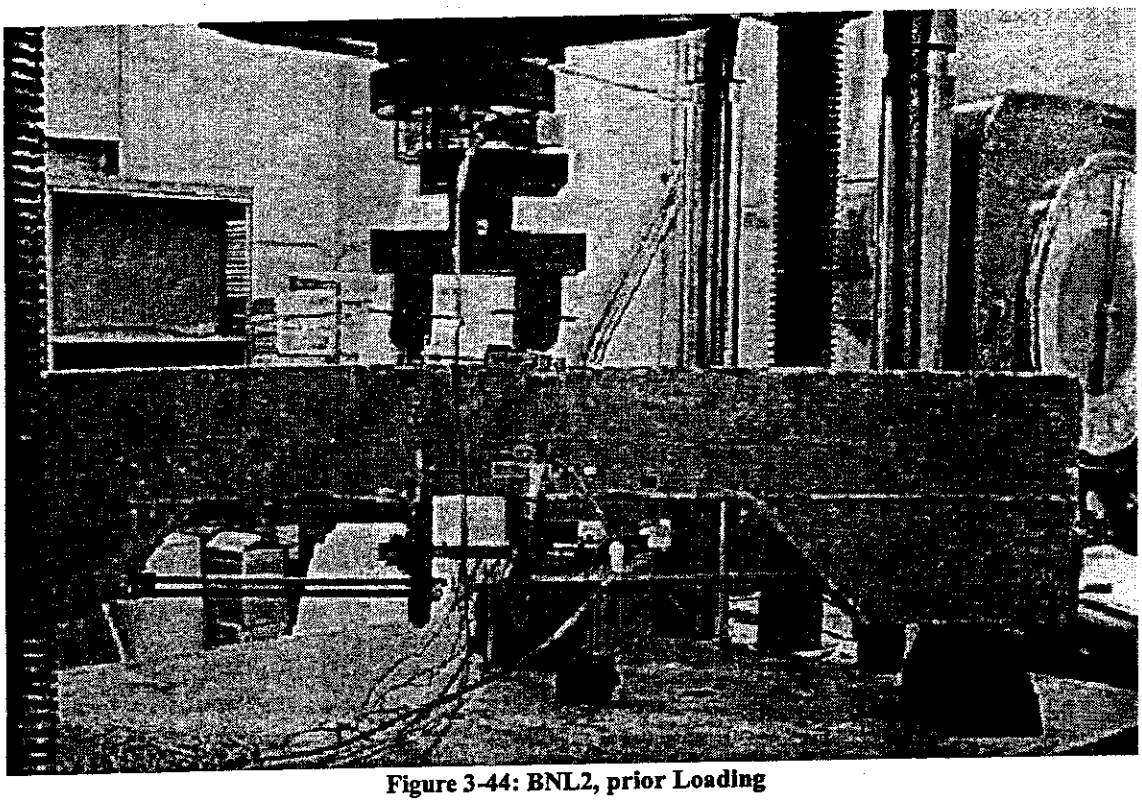

Figure 3-44: BNL2, prior Loading

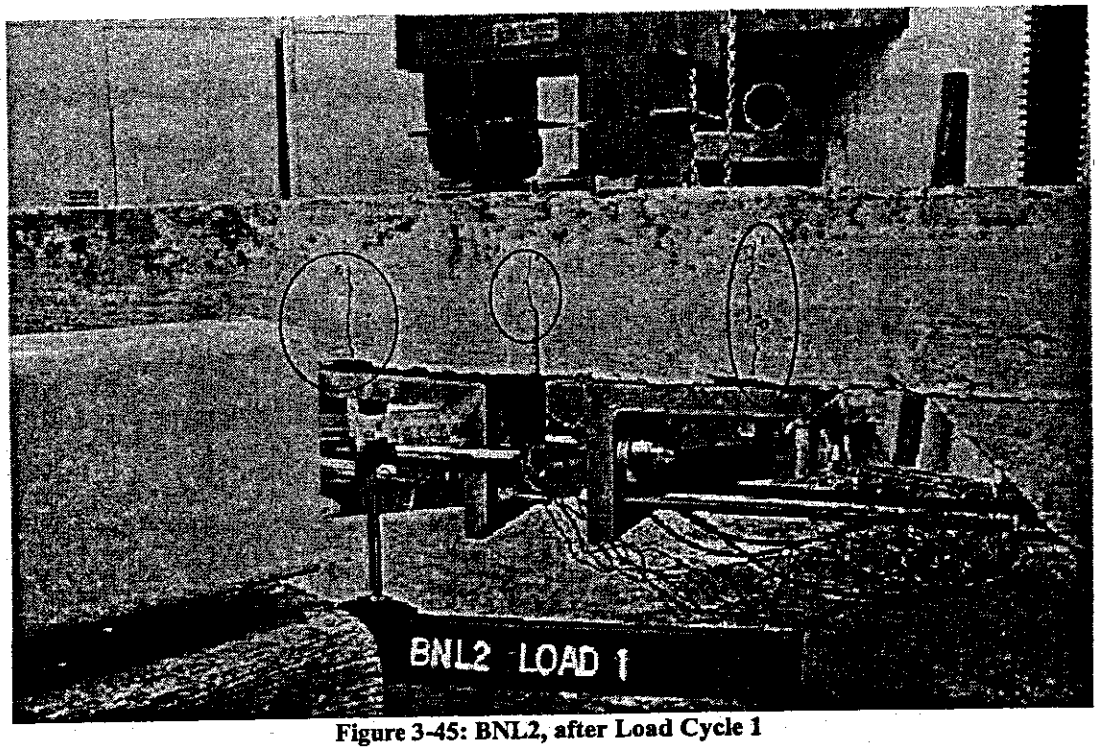

Figure 3-45: BNL2, after Load Cycle 1

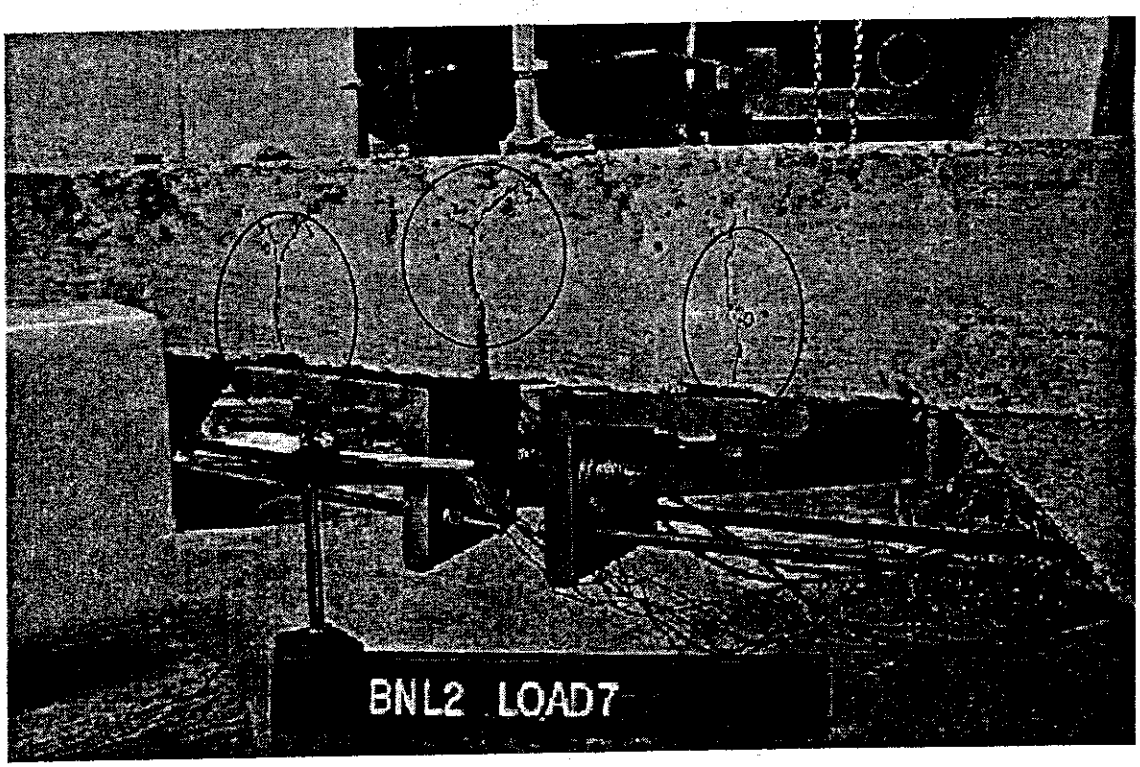

Figure 3-46: BNL2, after Final Load Cycle 7

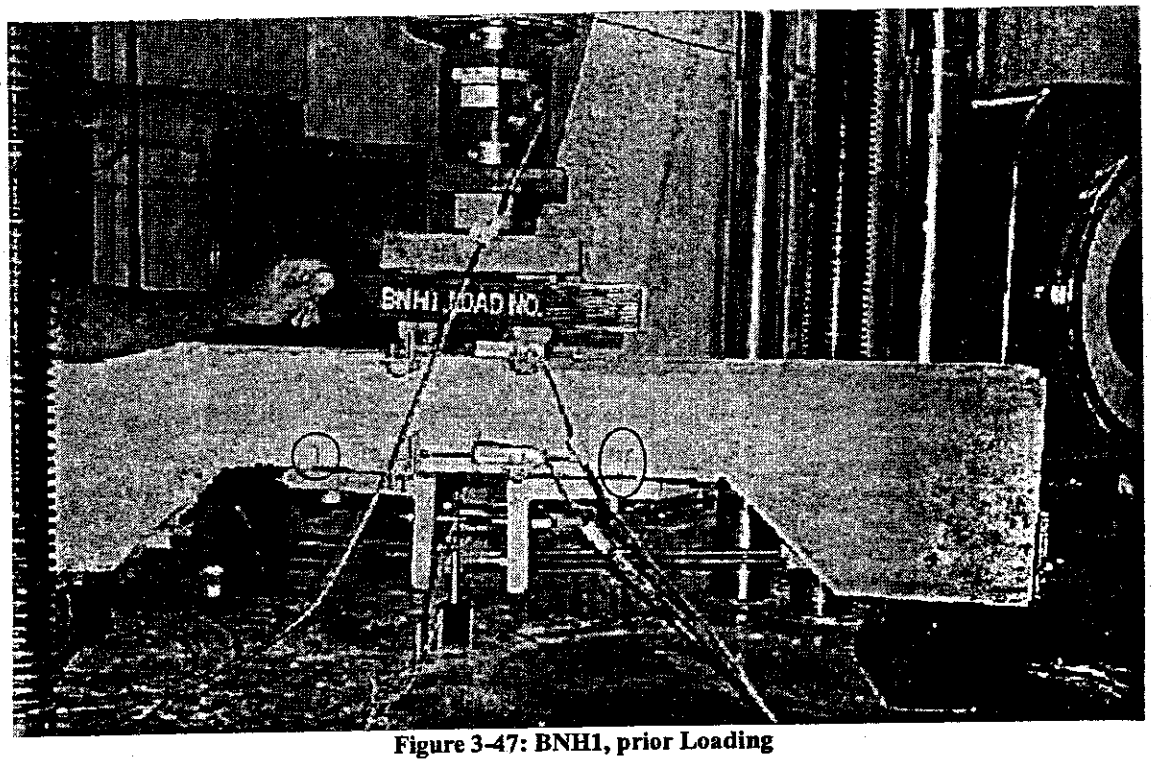

Figure 3-47: BNH1, prior Loading

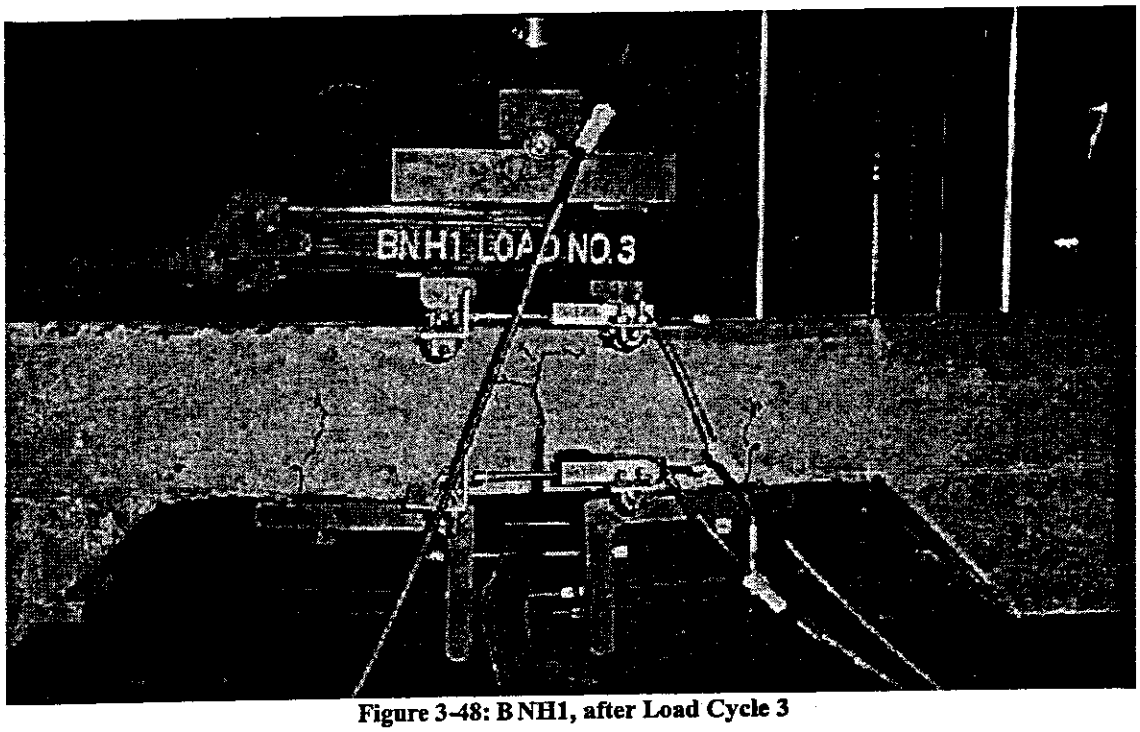

Figure 3-48: B NH1, after Load Cycle 3

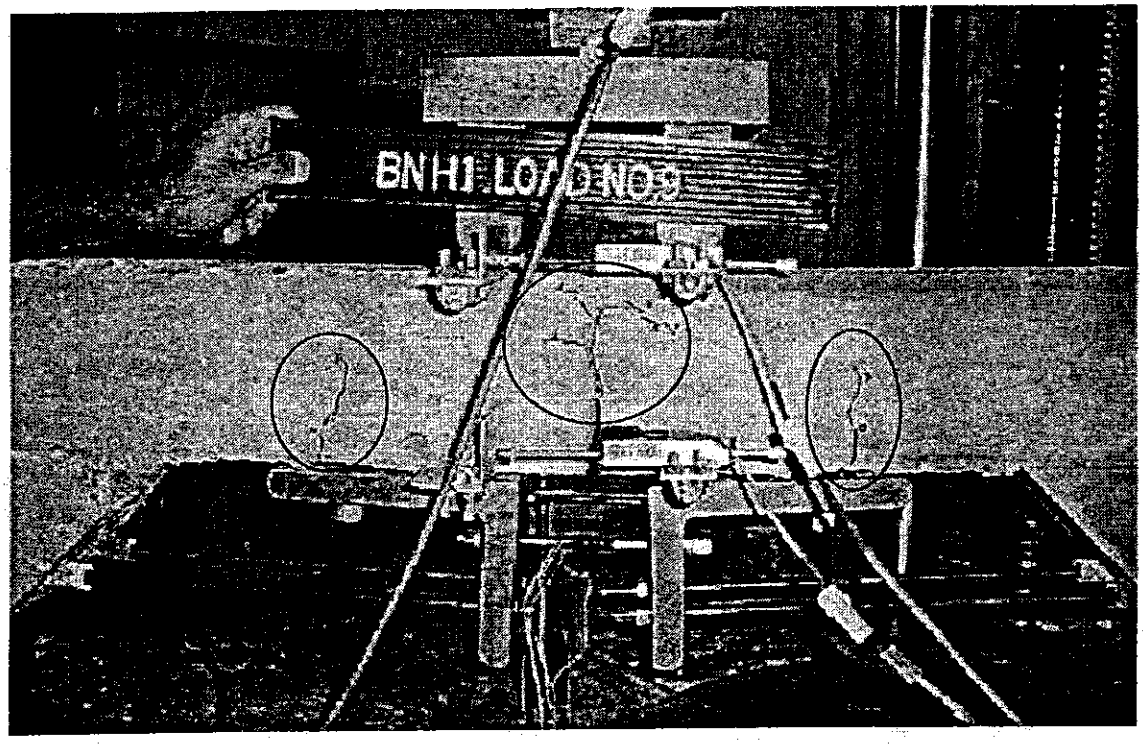

Figure 3-49: BNH1, after Final Load Cycle 9

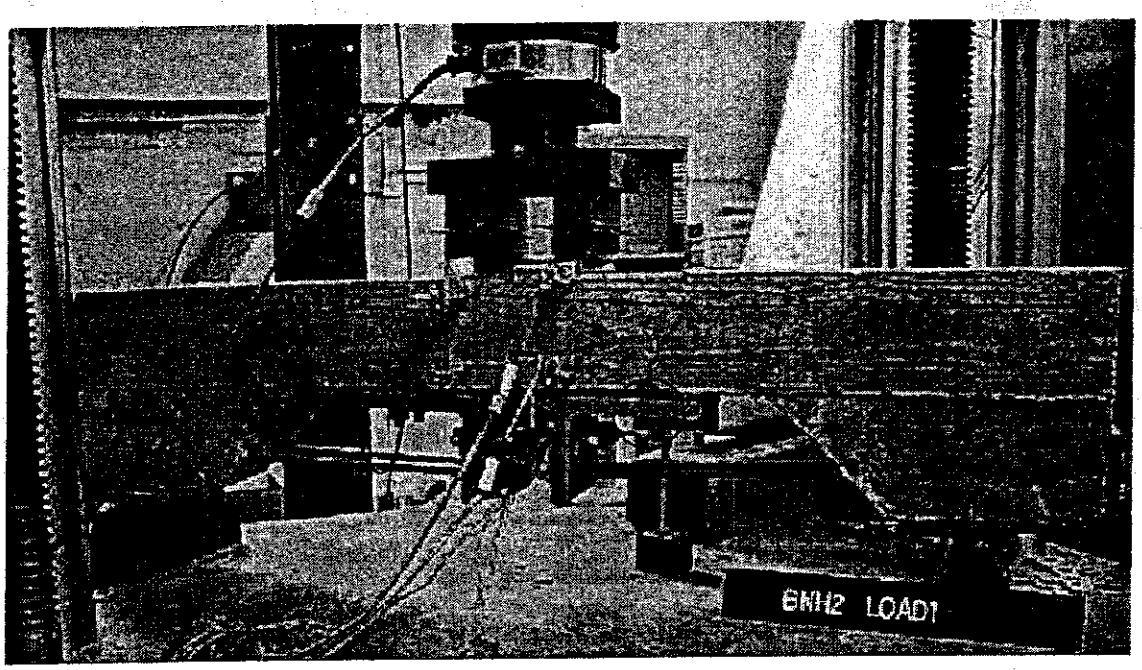

Figure 3-50: BNH2, prior Loading

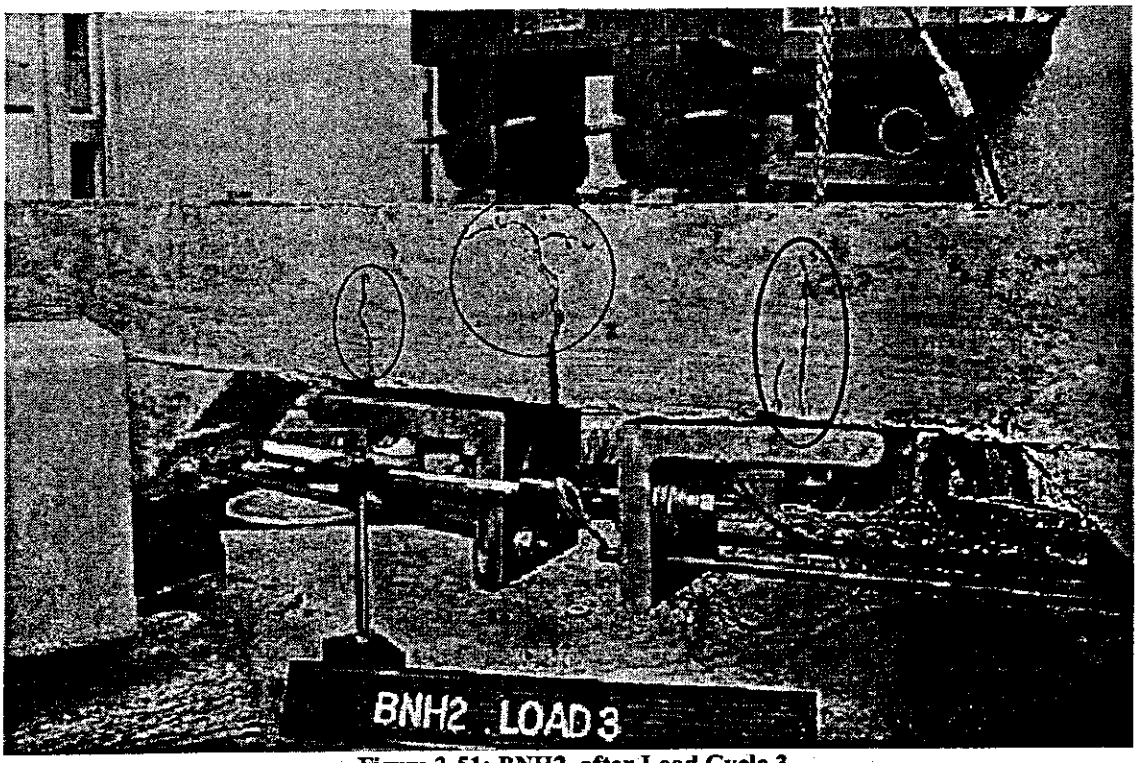

Figure 3-51: BNH2, after Load Cycle 3

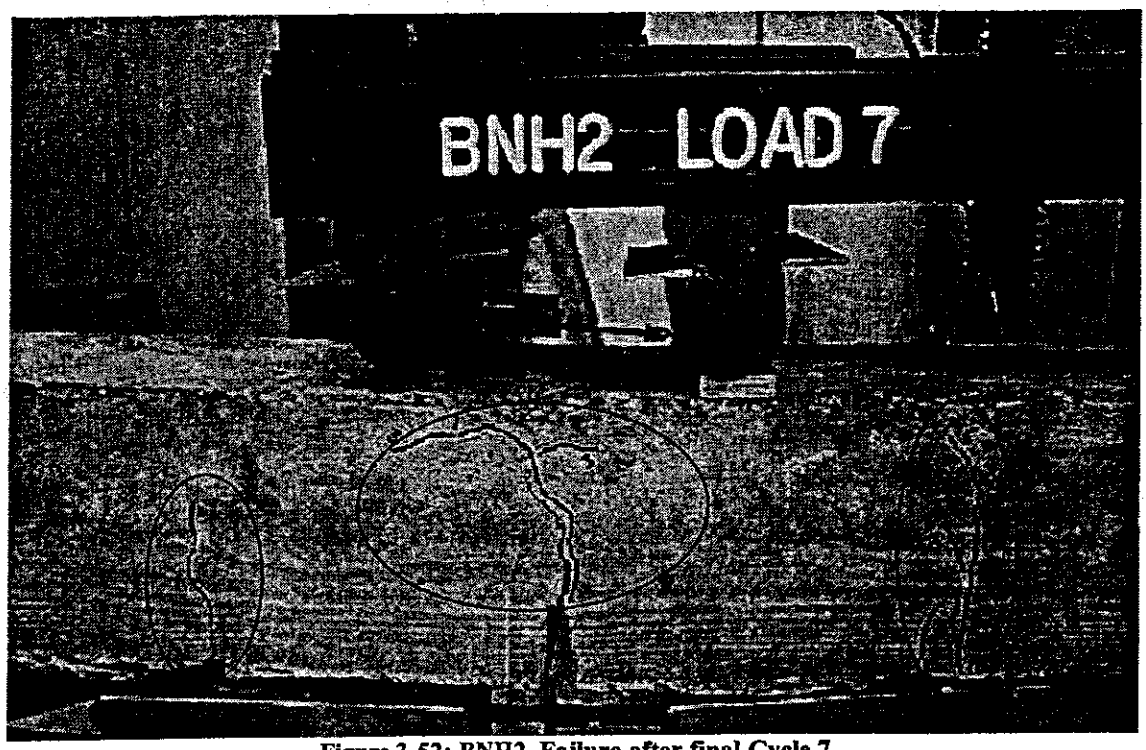

Figure 3-52: BNH2, Failure after final Cycle 7

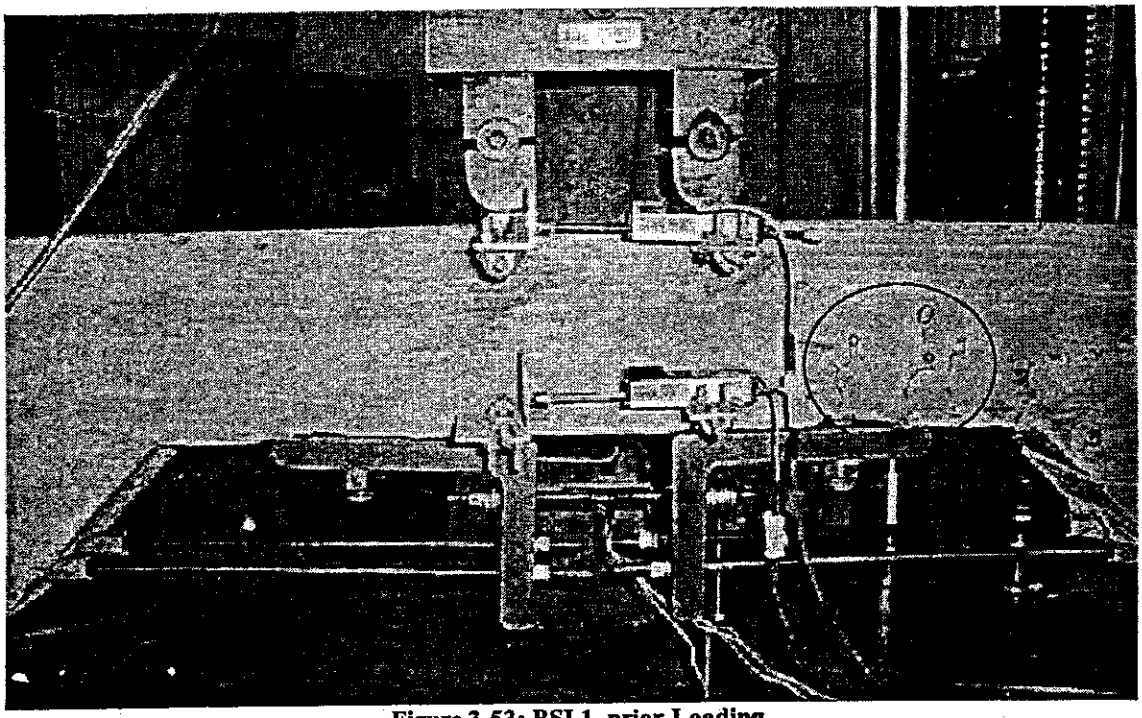

Figure 3-53: BSL1, prior Loading

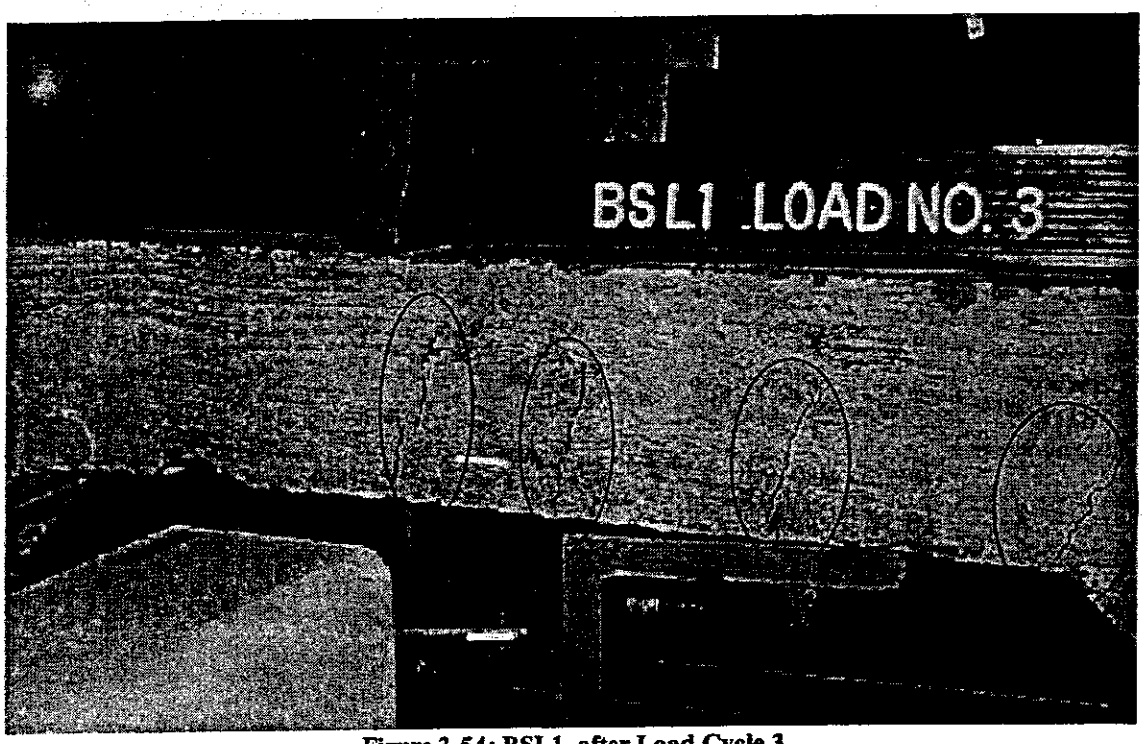

Figure 3-54: BSL1, after Load Cycle 3

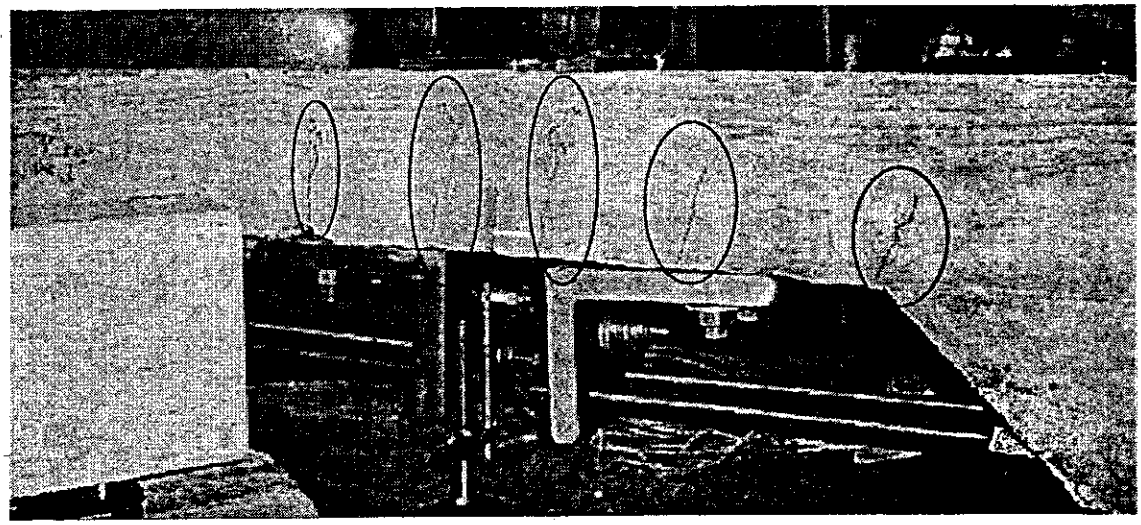

Figure 3-55: BSL1, after Final Load Cycle 9

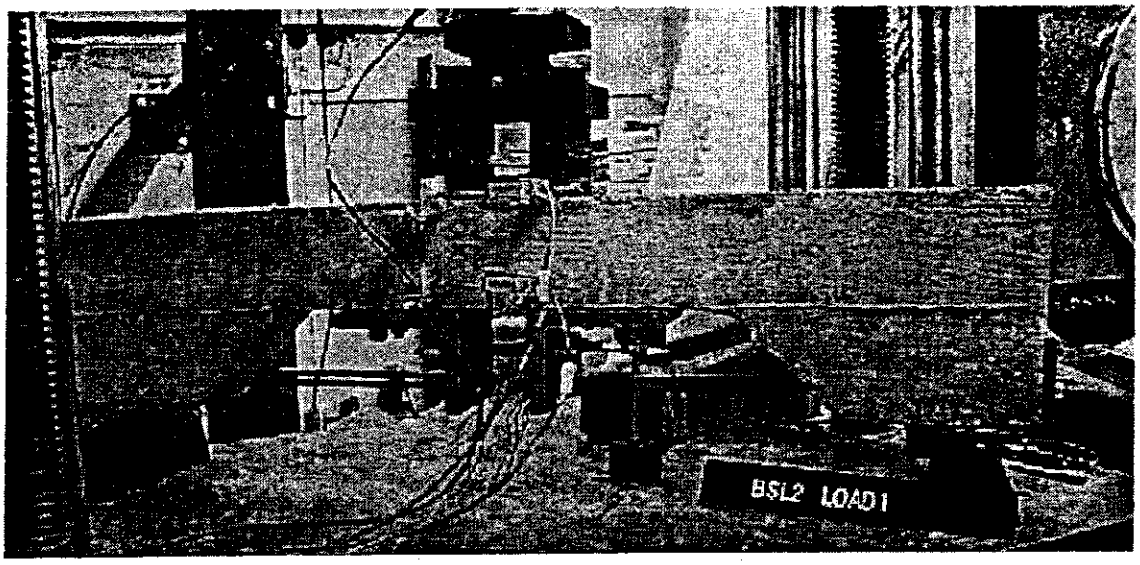

Figure 3-56: BSL2, prior Loading

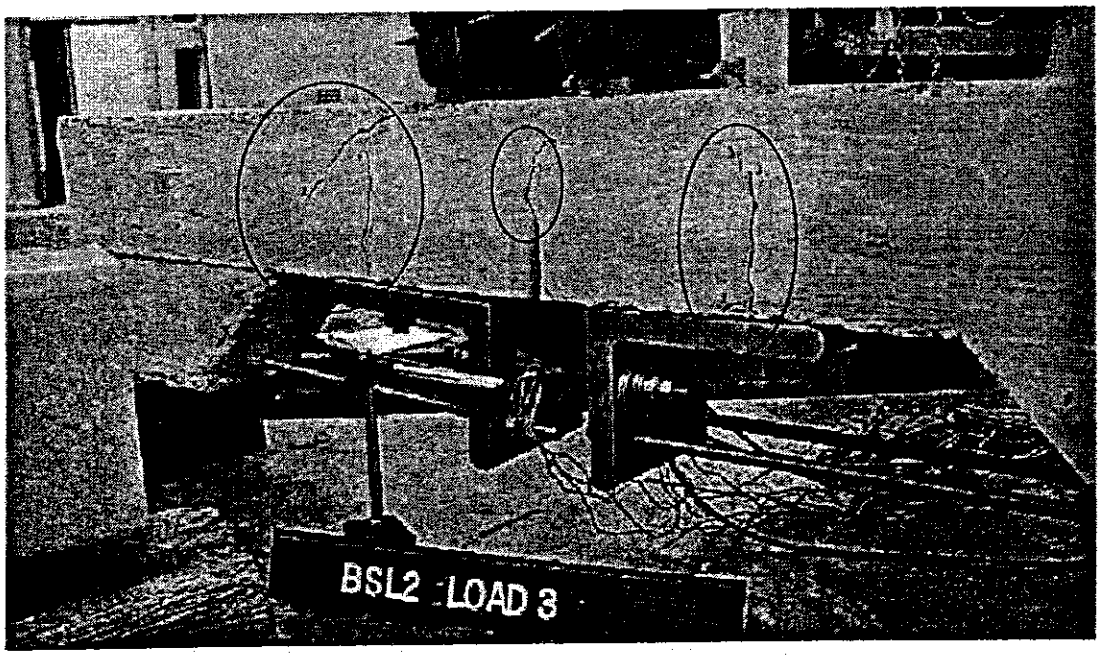

Figure 3-57: BSL2, after Load Cycle 3

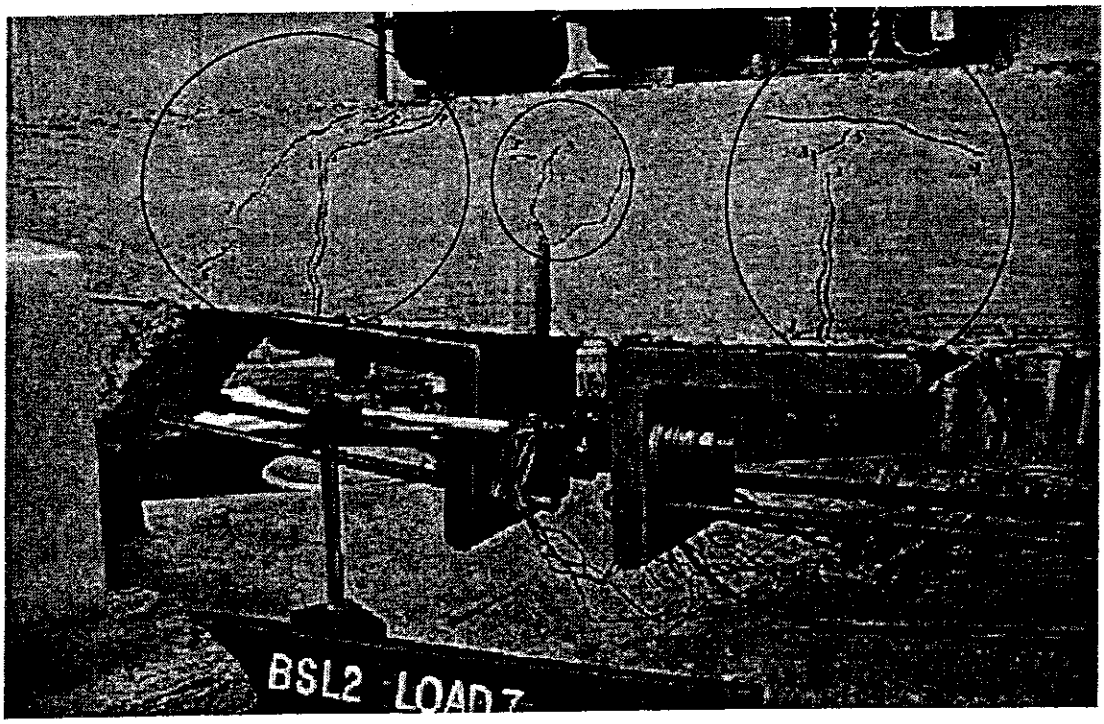

Figure 3-58: BSL2, after Final Load Cycle 7

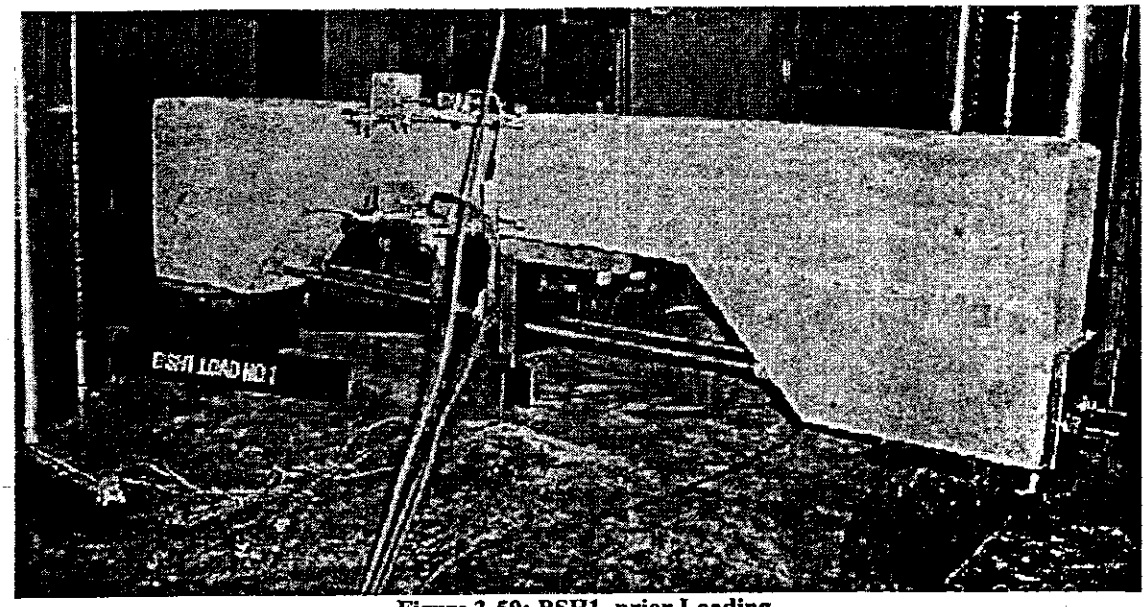

Figure 3-59: BSH1, prior Loading

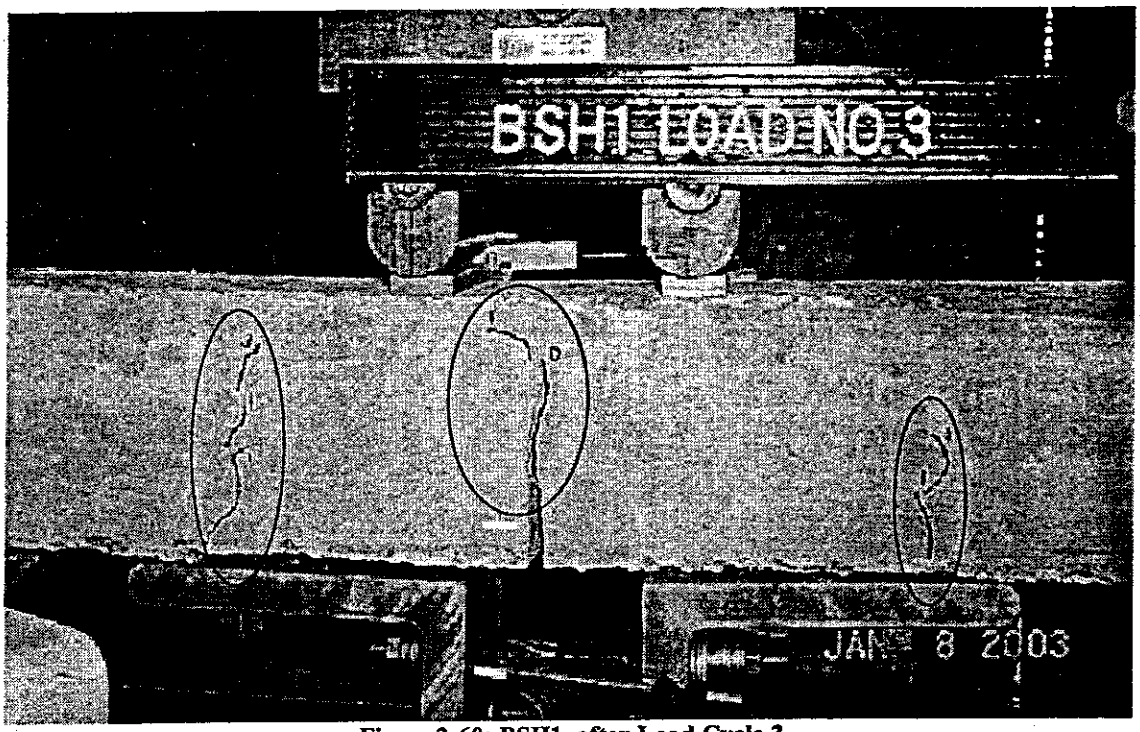

Figure 3-60: BSH1, after Load Cycle 3

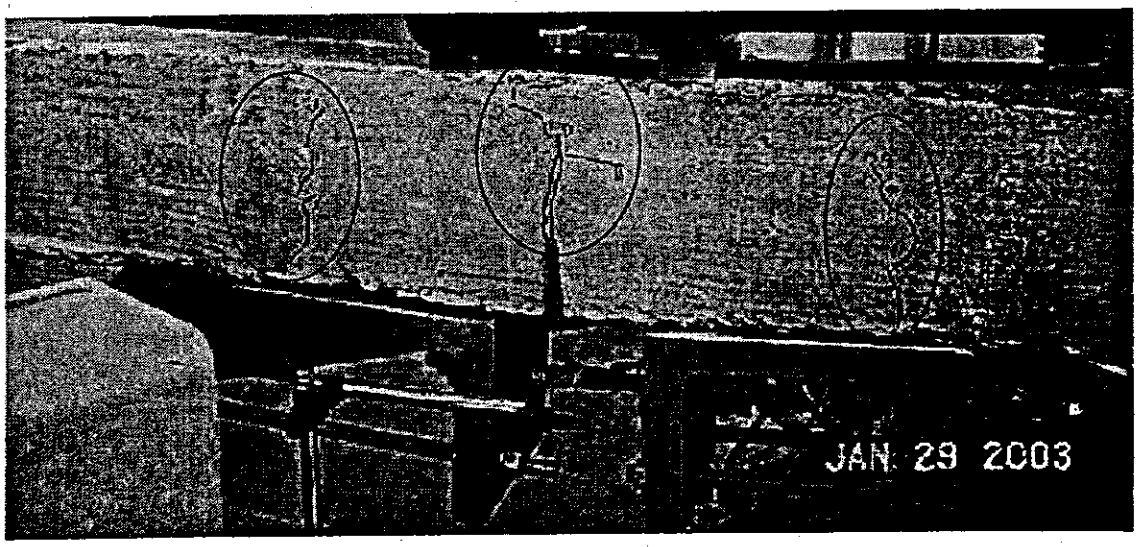

Figure 3-61: BSH1, Failure after Load Cycle 11

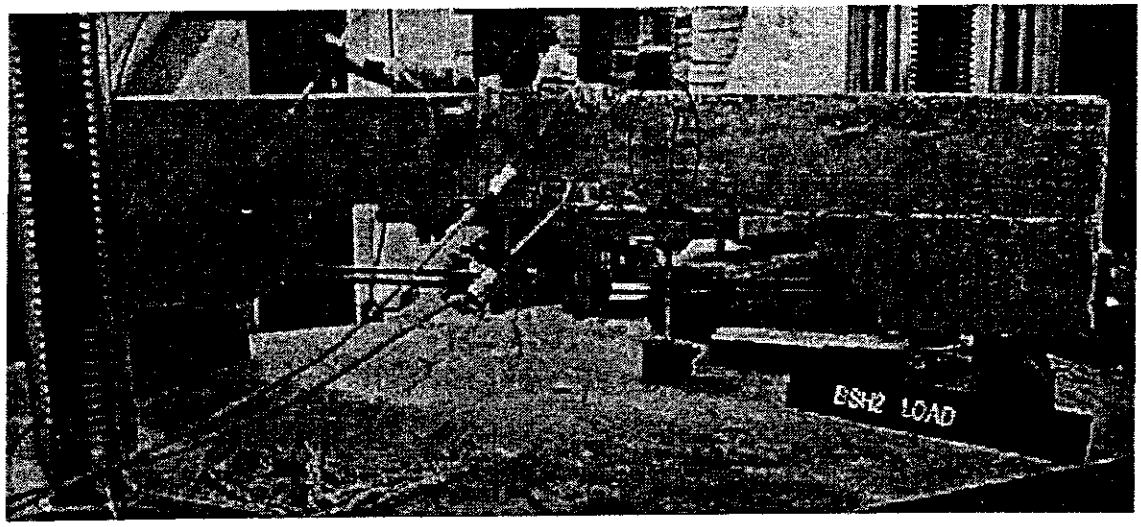

Figure 3-62: BSH2, prior Loading

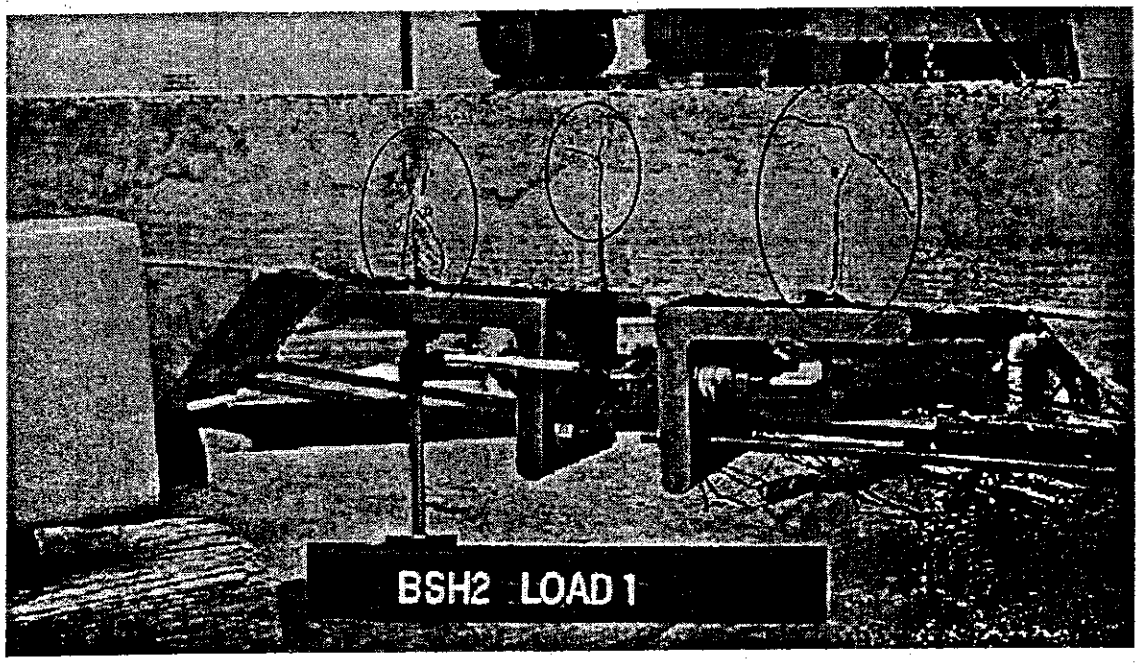

Figure 3-63: BSH2, after Load Cycle 1

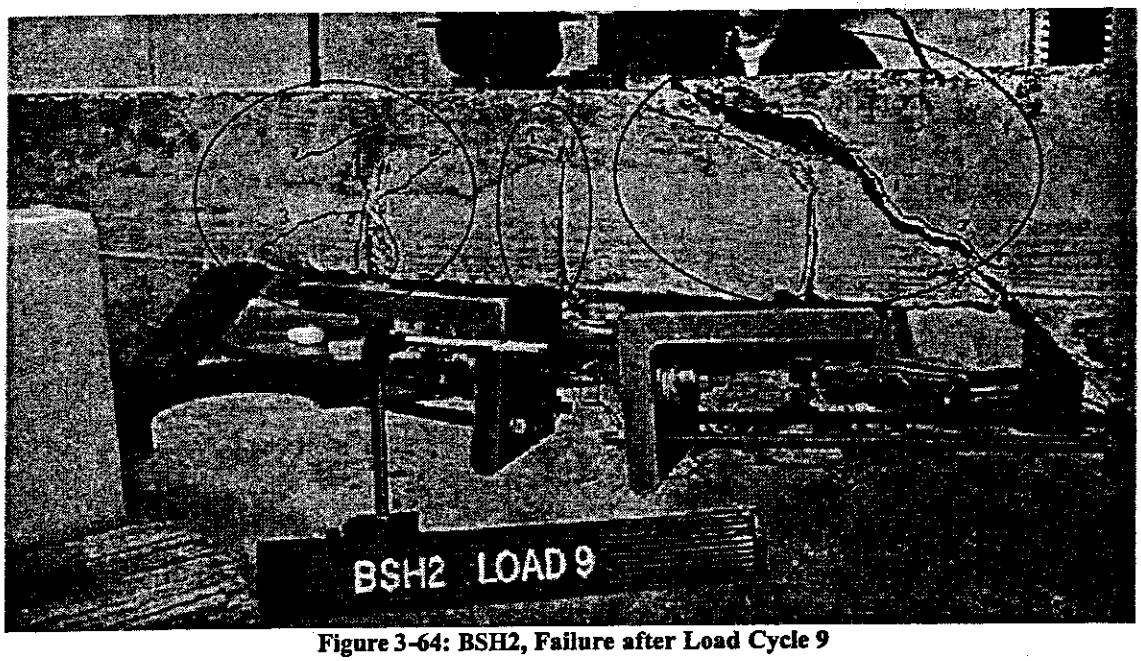

Figure 3-64: BSH2, Failure after Load Cycle 9

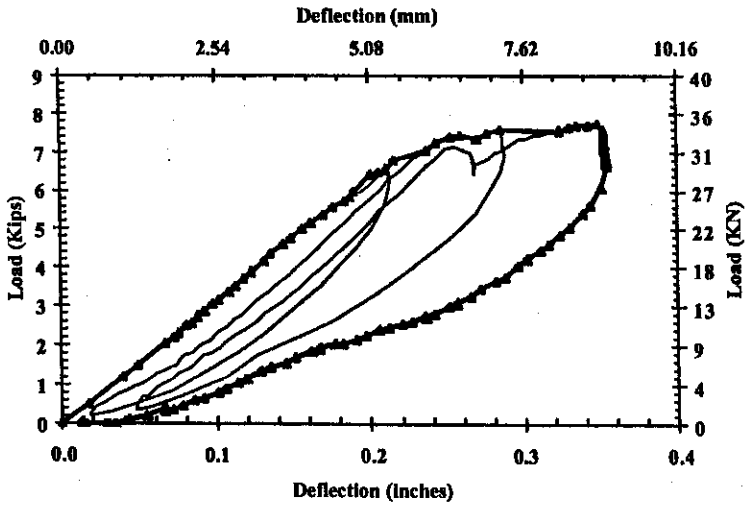

Figure 3-65: B-N-H-1 Load vs. Displacement

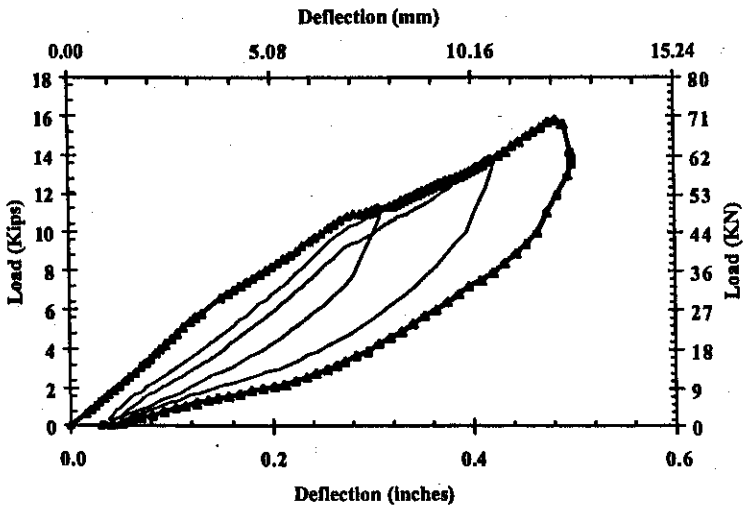

Figure 3-66: B-N-H-2 Load vs. Displacement

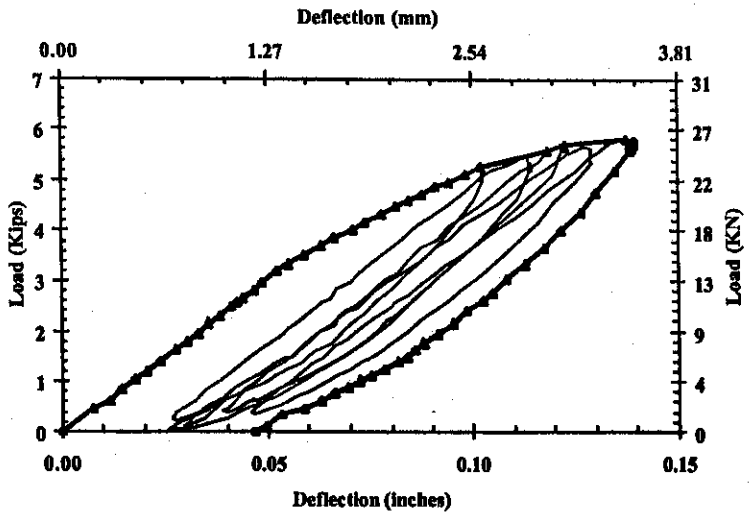

Figure 3-67: B-S-L-1 Load vs. Displacement

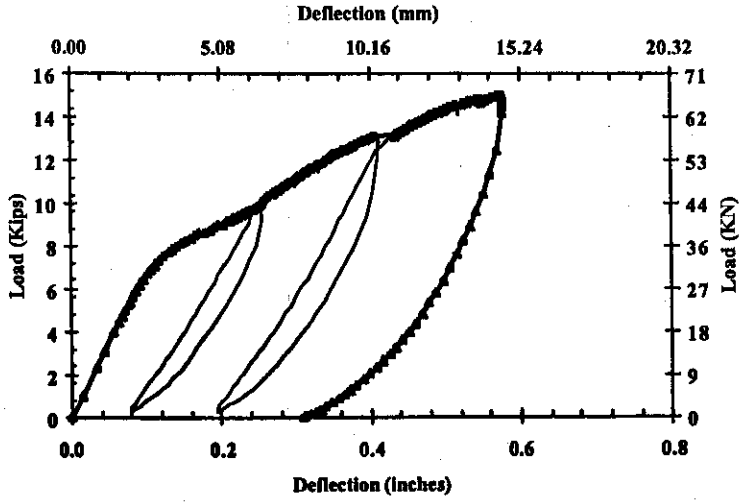

Figure 3-68: B-S-L-2 Load vs. Displacement

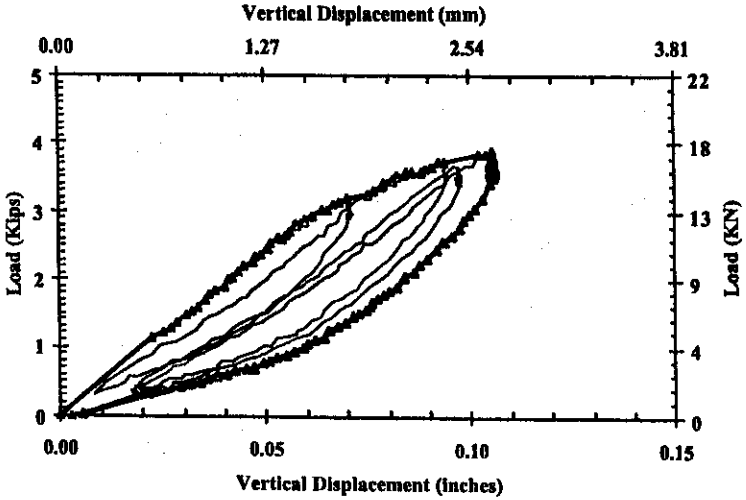

Figure 3-69: B-N-L-1 Load vs. Displacement

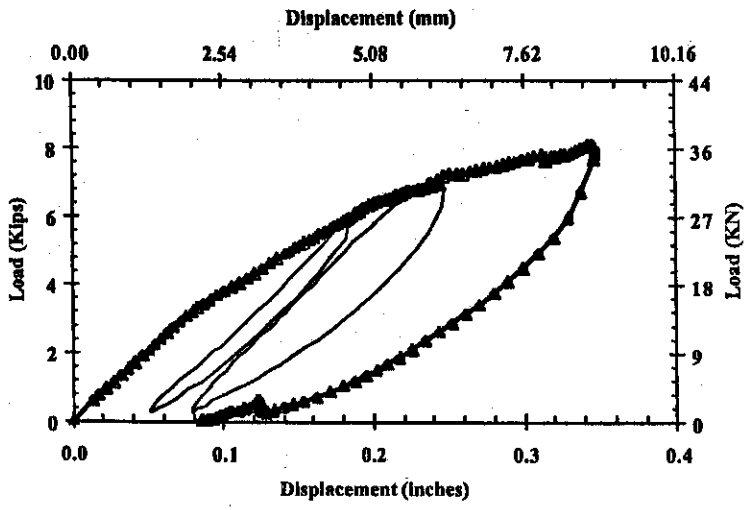

Figure 3-70: B-N-L-2 Load vs. Displacement

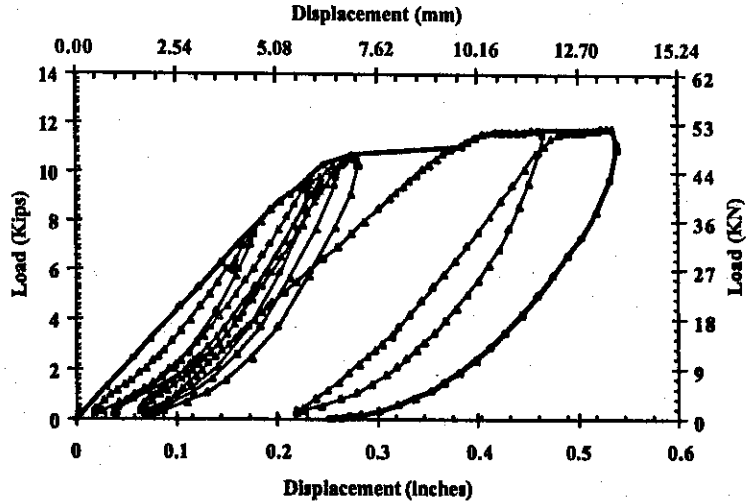

Figure 3-71: B-S-H-1 Load vs. Displacement

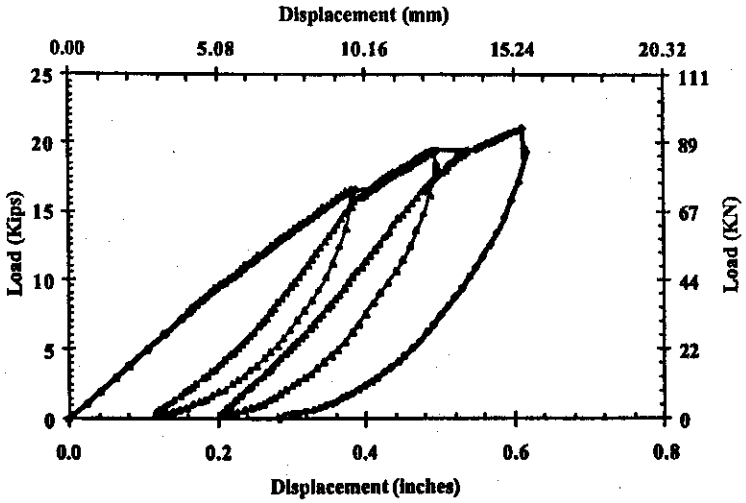

Figure 3-72: B-S-H-2 Load vs. Displacement

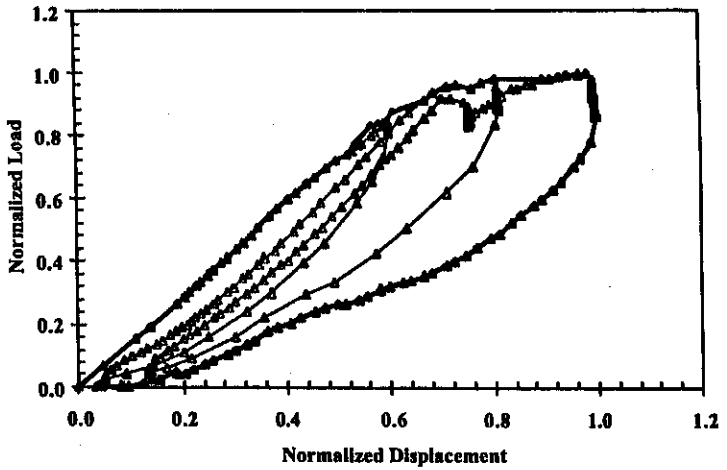

Figure 3-73: B-N-H-1 Normalized Load vs. Nor malized Displacement

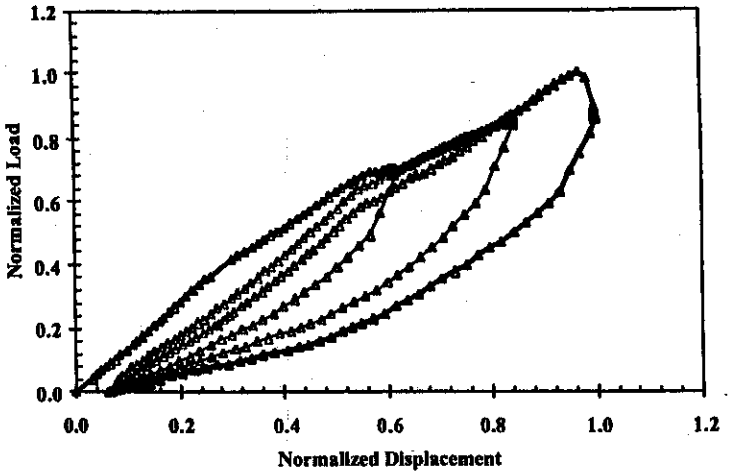

Figure 3-74: B-N-H-1 Normalized Load vs. Normalized Displacement

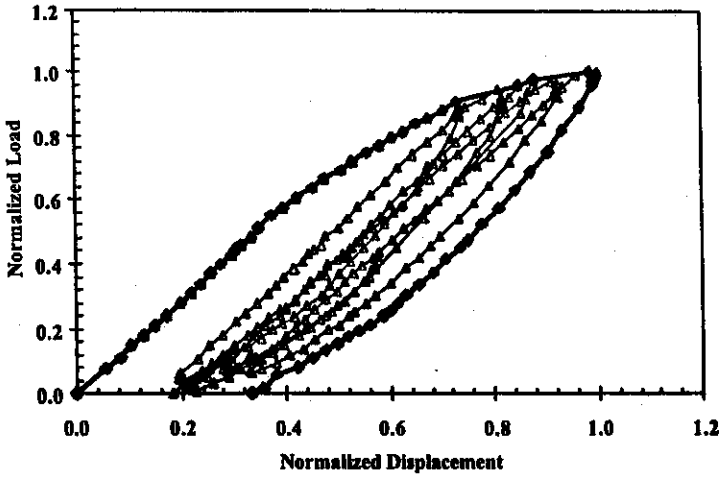

Figure 3-75: B-S-L-1 Normalized Load vs. Normalized Displacement

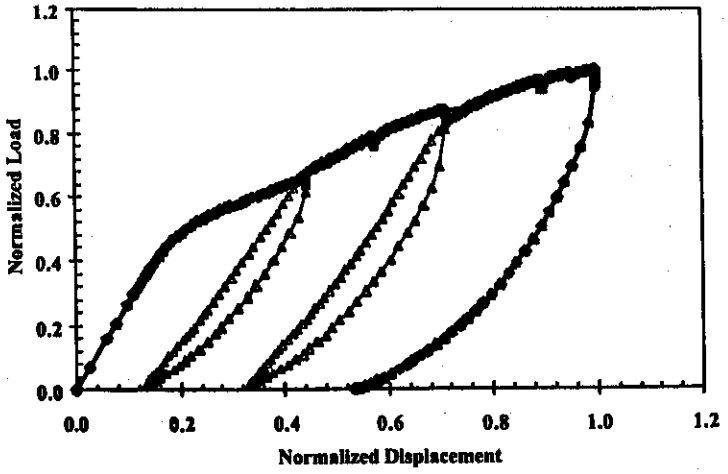

Figure 3-76: B-S-L-2 Normalized Load vs. Normalized Displacement

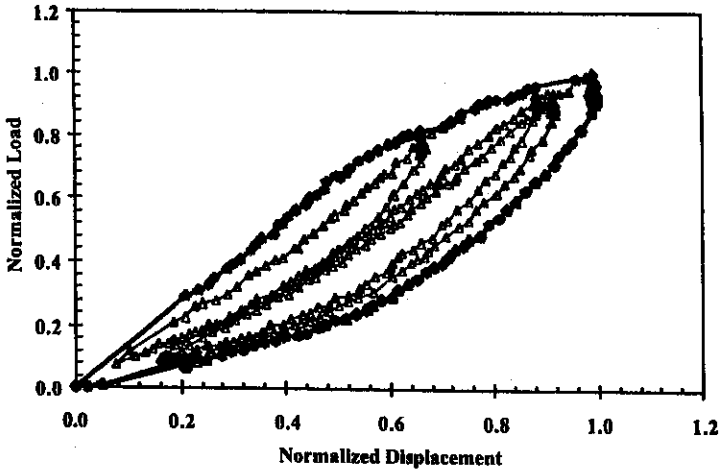

Figure 3-77: B-N-L-1 Normalized Load vs. Normalized Displacement

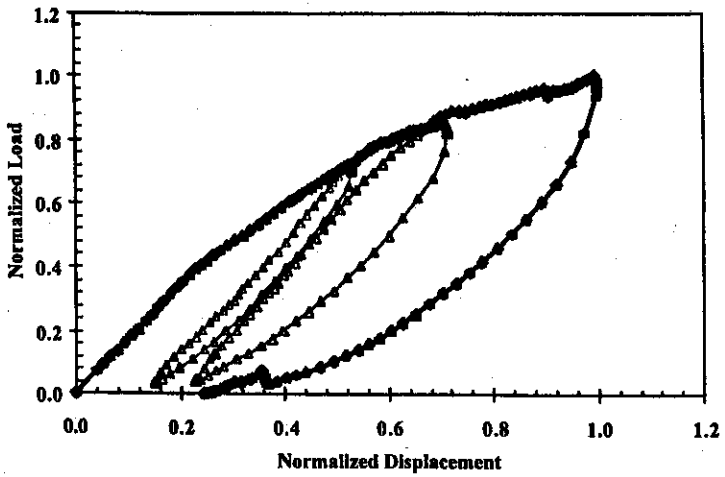

Figure 3-78: B-N-L-2 Normalized Load vs. Normalized Displacement

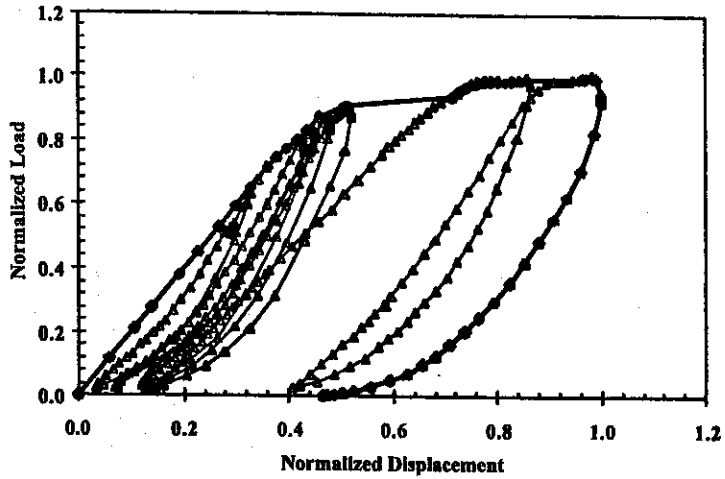

Figure 3-79: B-S-H-1 Normalized Load vs. Normalized Displacement

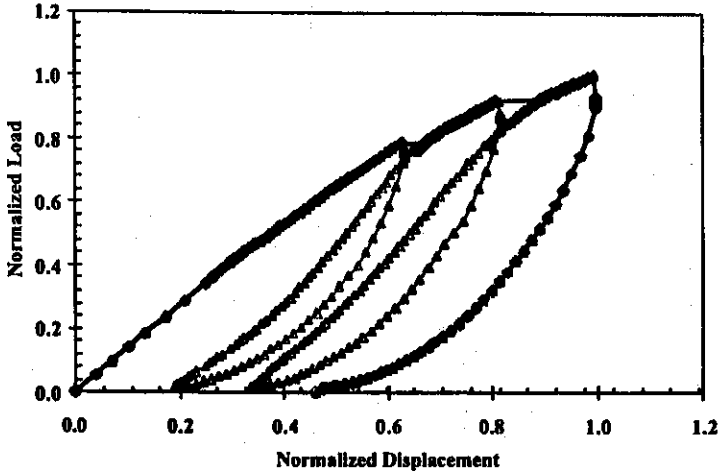

Figure 3-80: B-S-H-2 Normalized Load vs. Normalized Displacement

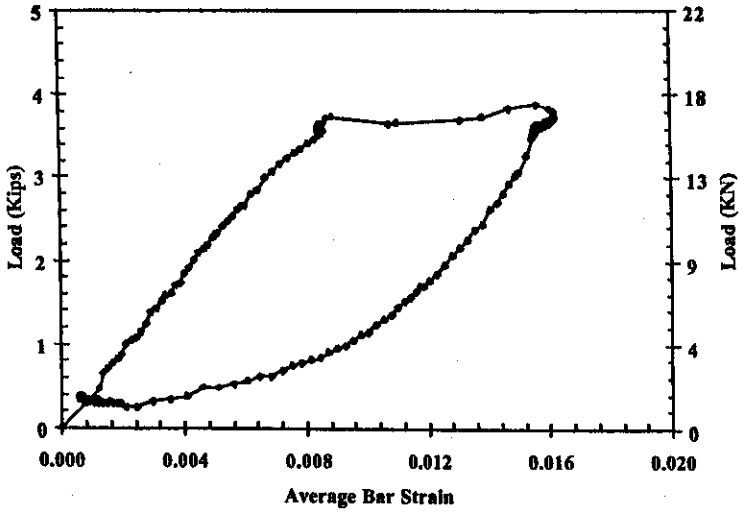

Figure 3-81: B-N-L-1, Load vs. Average Bar Strain

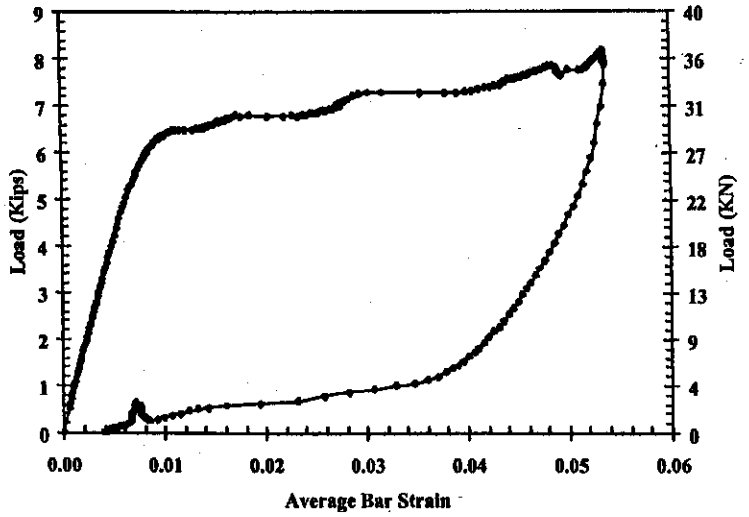

Figure 3-82: B-N-L-2, Load vs. Average Bar Strain

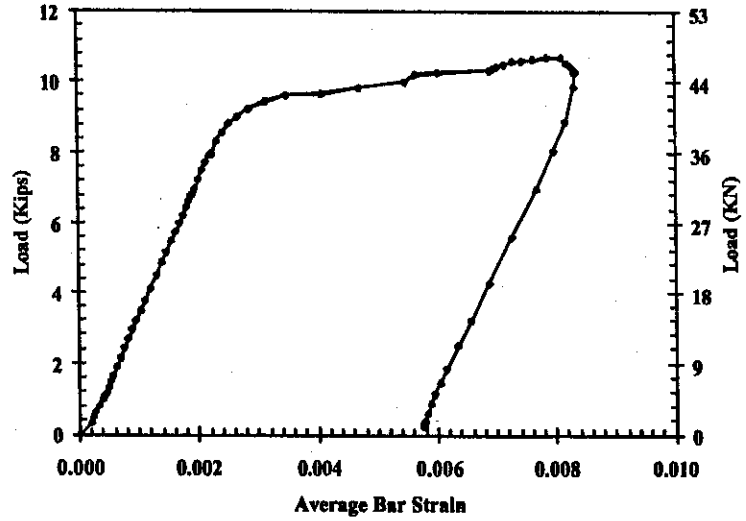

Figure 3-83: B-S-H-1, Load vs. Average Bar Strain

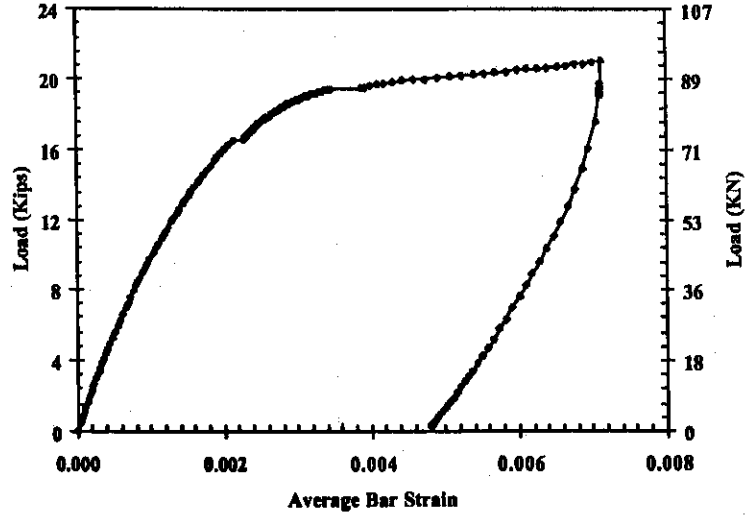

Figure 3-84: B-S-H-2, Load vs. Average Bar Strain

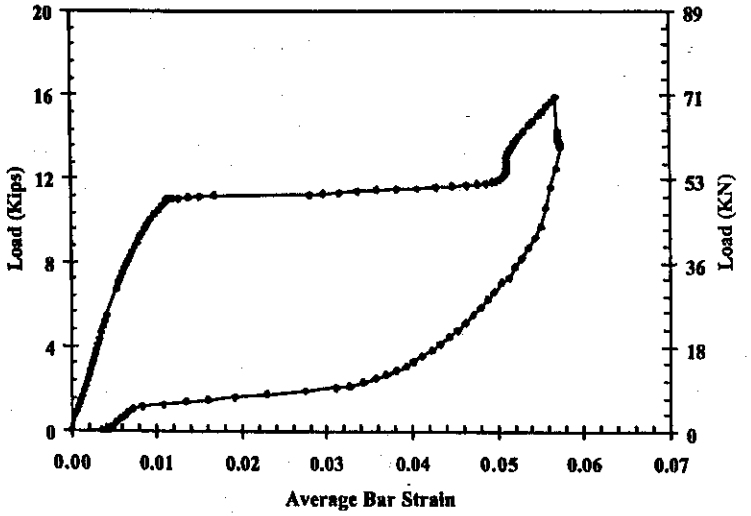

Figure 3-85: B-N-H-2, Load vs. Average Bar Strain

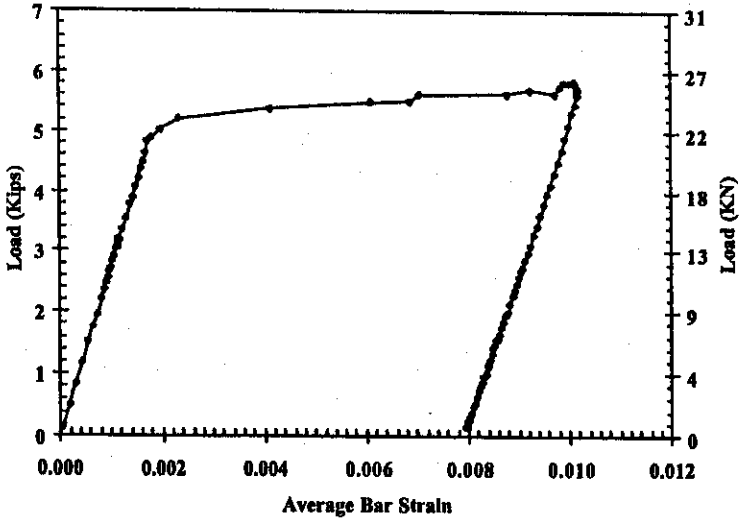

Figure 3-86: B-S-L-1, Load vs. Average Bar Strain

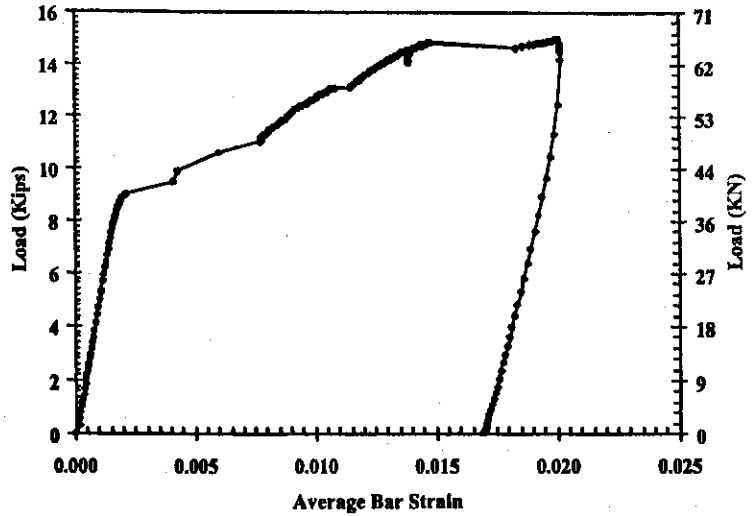

Figure 3-87: B-S-L-2, Load vs. Average Bar Strain

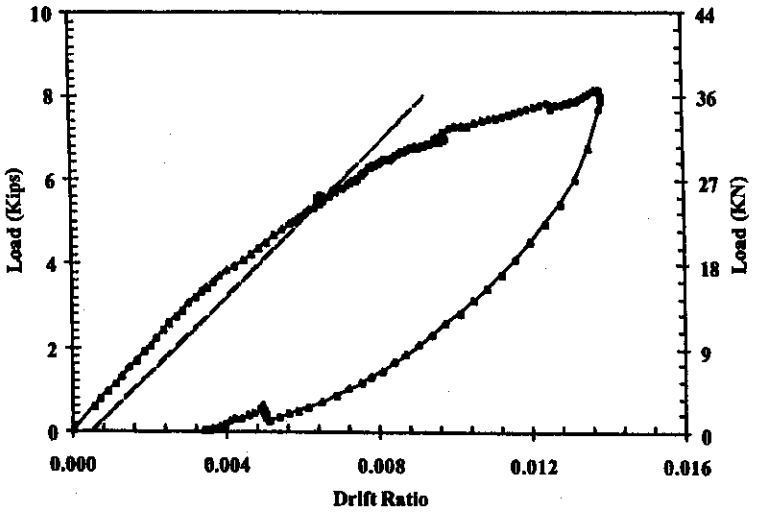

Figure 3-88: BNL2, Load vs. Drift Ratio

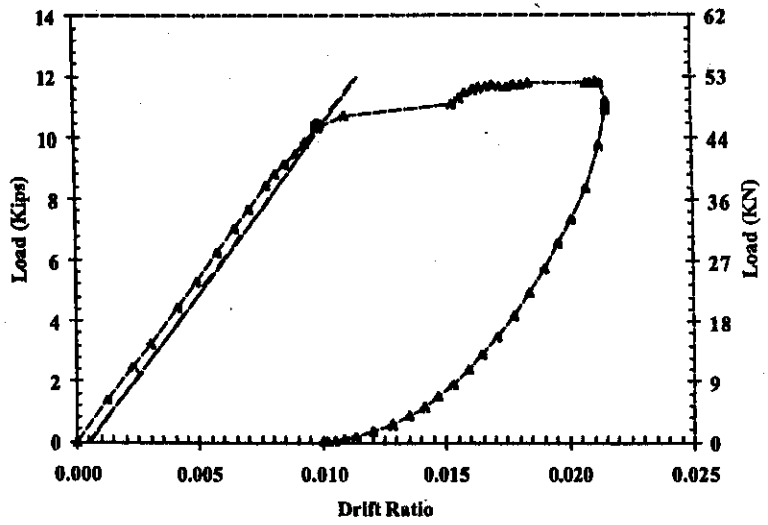

Figure 3-89: BSH1, Load vs. Drift Ratio

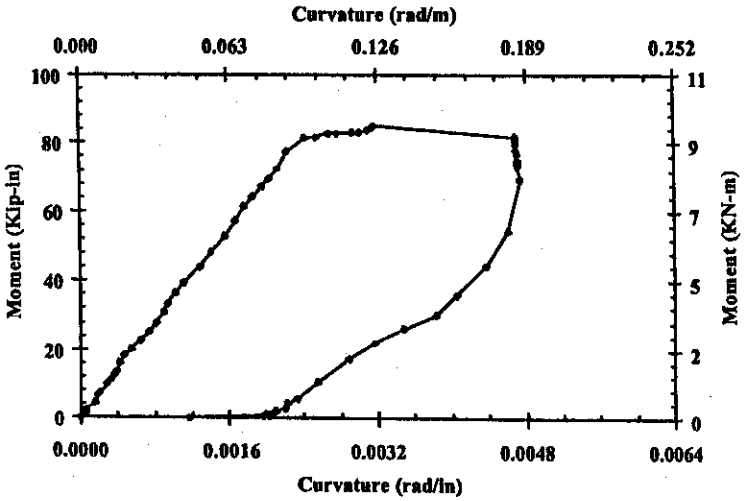

Figure 3-90: B-N-H-1, Moment vs. Curvature

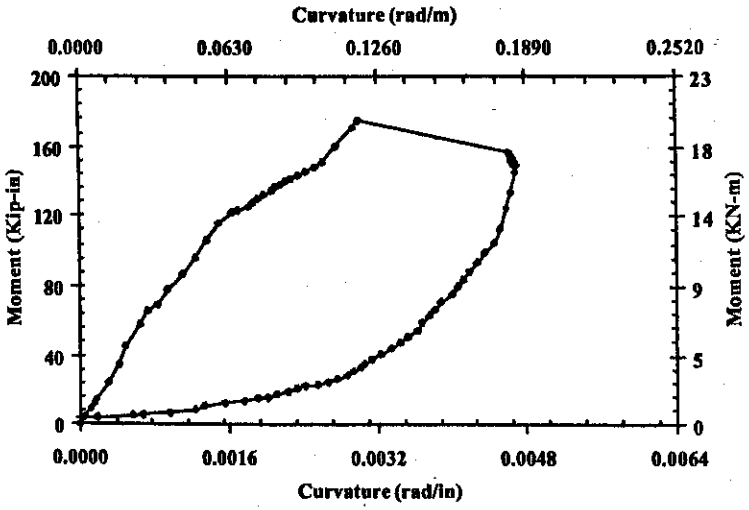

Figure 3-91: B-N-H-2, Moment vs. Curvature

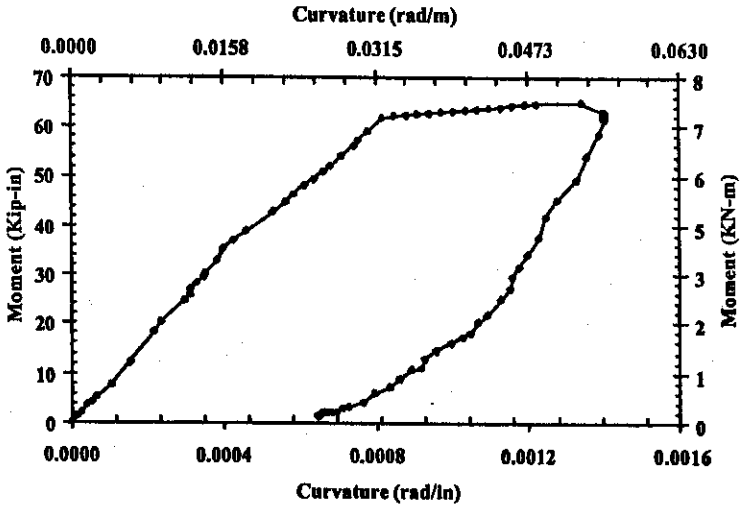

Figure 3-92: B-S-L-1, Moment vs. Curvature

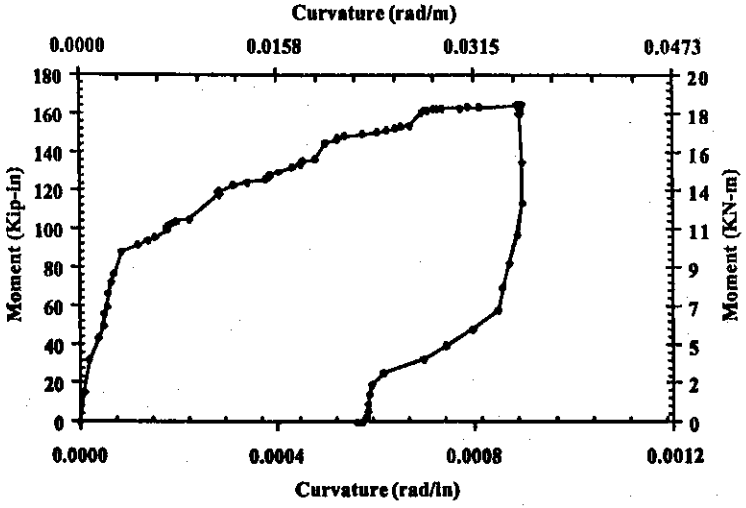

Figure 3-93: B-S-L-2, Moment vs. Curvature

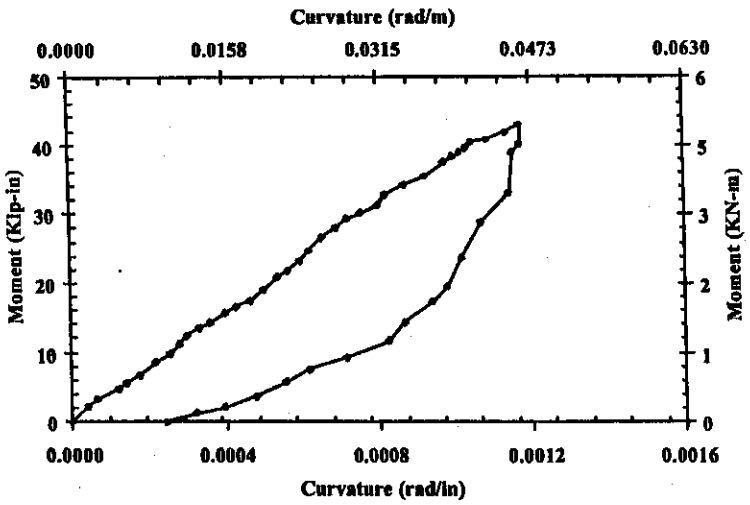

Figure 3-94: B-N-L-1, Moment vs. Curvature

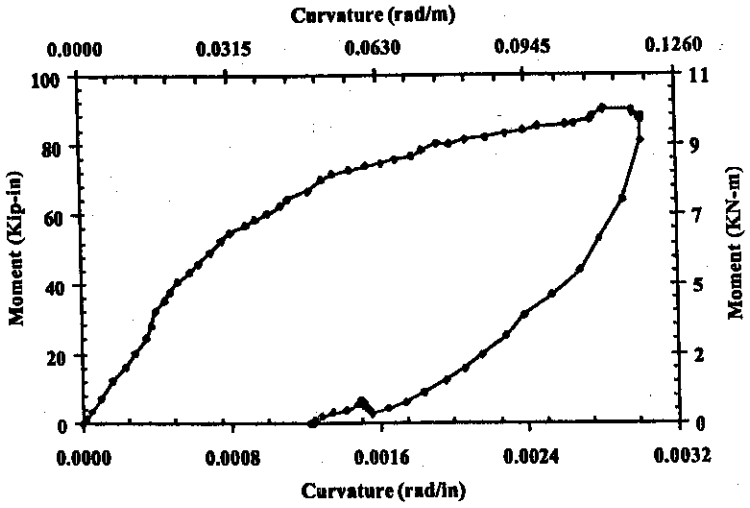

Figure 3-95: B-N-L-2, Moment vs. Curvature

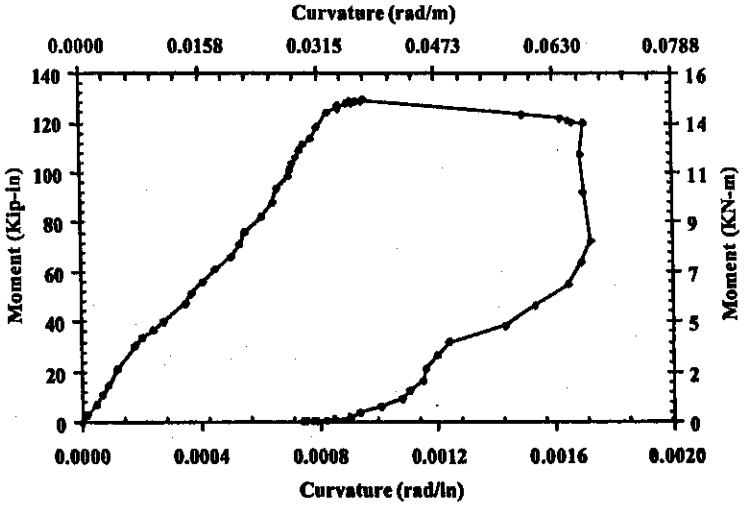

Figure 3-96: B-S-H-1, Moment vs. Curvature

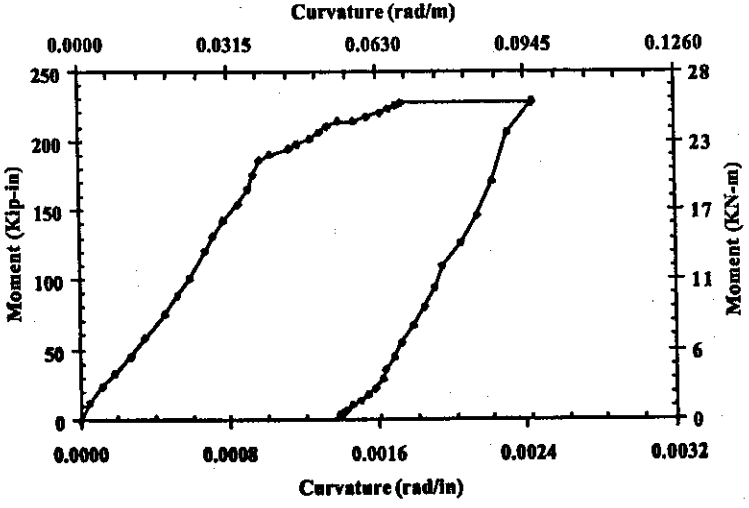

Figure 3-97: B-S-H-2, Moment vs. Curvature

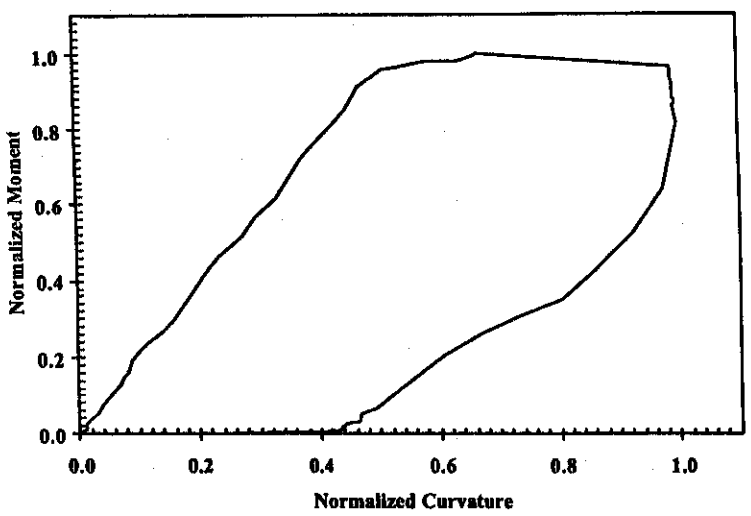

Figure 3-98: BNH1, Normalized Moment vs. Normalized Curvature

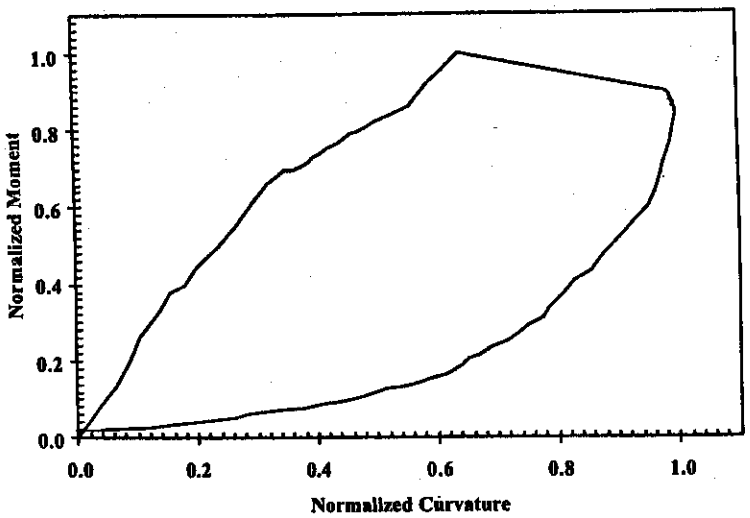

Figure 3-99: BNH2, Normalized Moment vs. Normalized Curvature

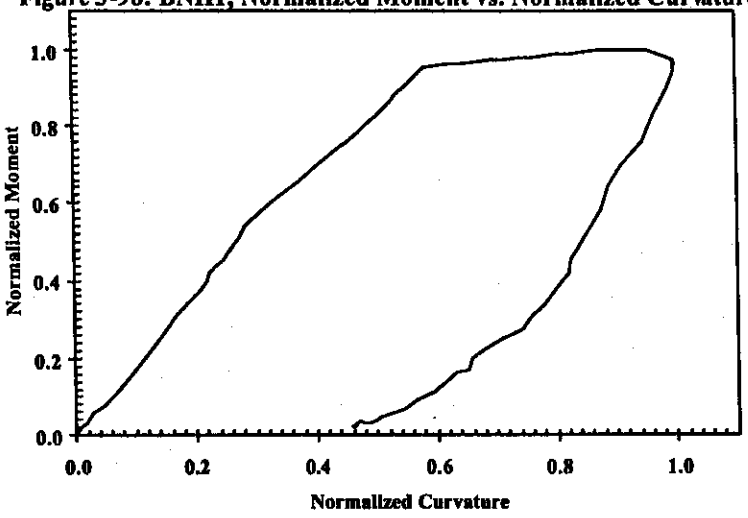

Figure 3-100: BSL1, Normalized Moment vs. Normalized Curvature

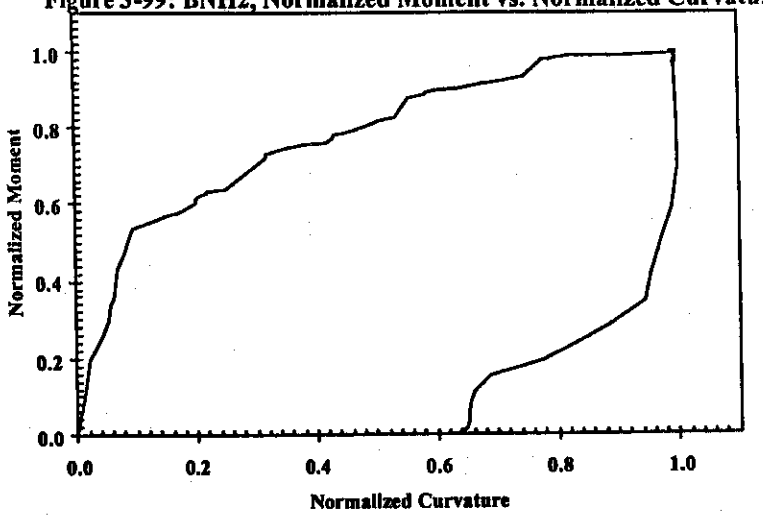

Figure 3-101: BSL2, Normalized Moment vs. Normalized Curvature

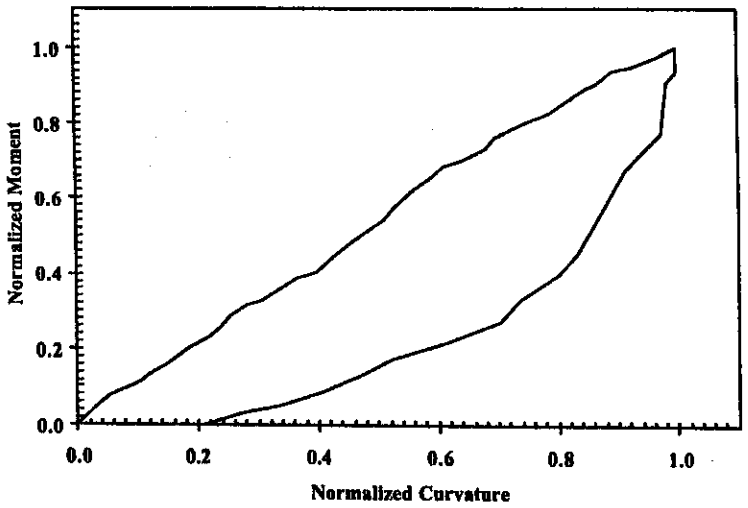

Figure 3-102: BNL1, Normalized Moment vs. Normalized Curvature

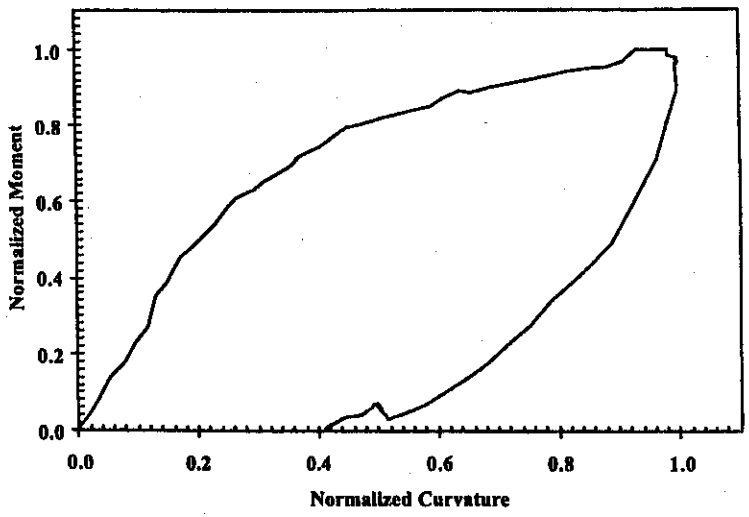

Figure 3-103: BNL2, Normalized Moment vs. Normalized Curvature

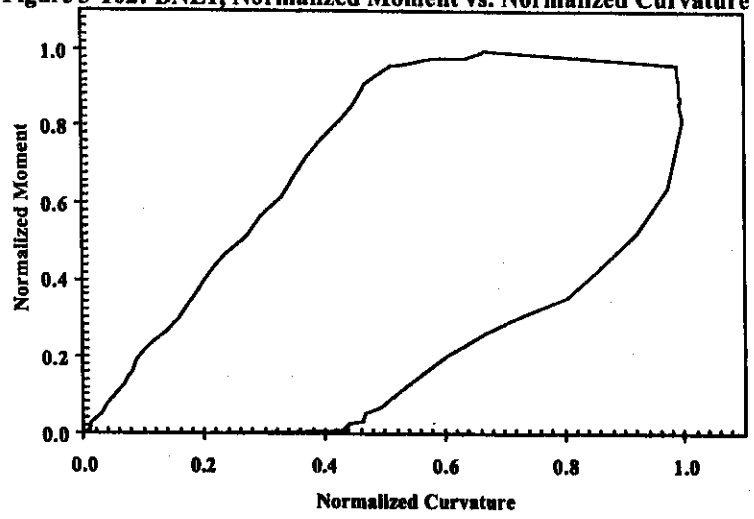

Figure 3-104: BSH1, Normalized Moment vs. Normalized Curvature

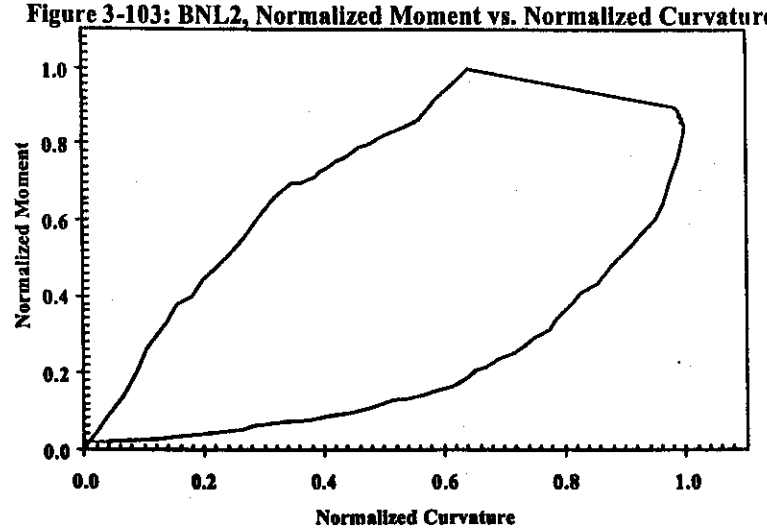

Figure 3-105: BSH2, Normalized Moment vs. Normalized Curvature

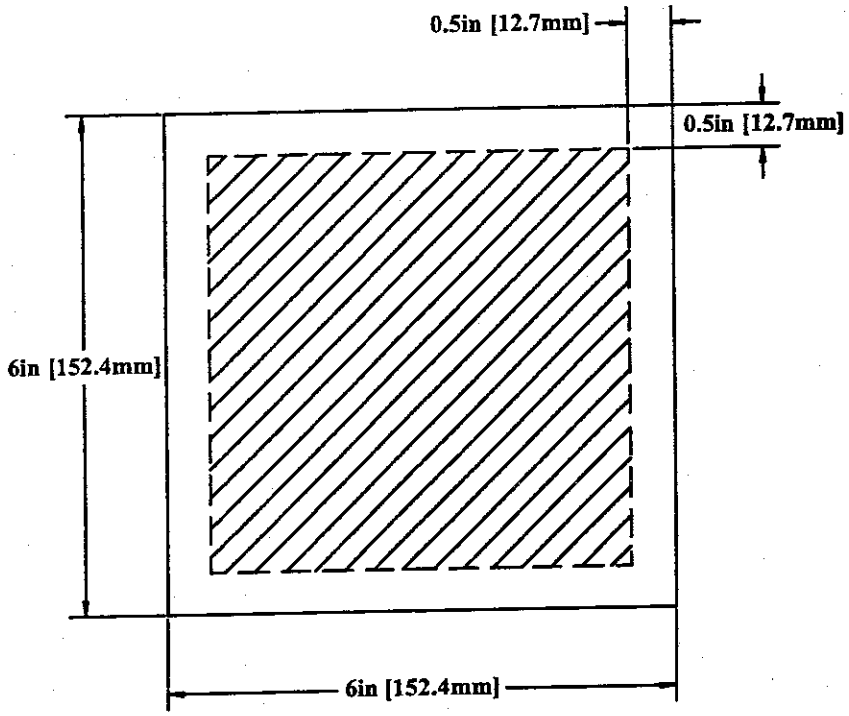

Figure 4- 1: Plan View of Confined Cube Area

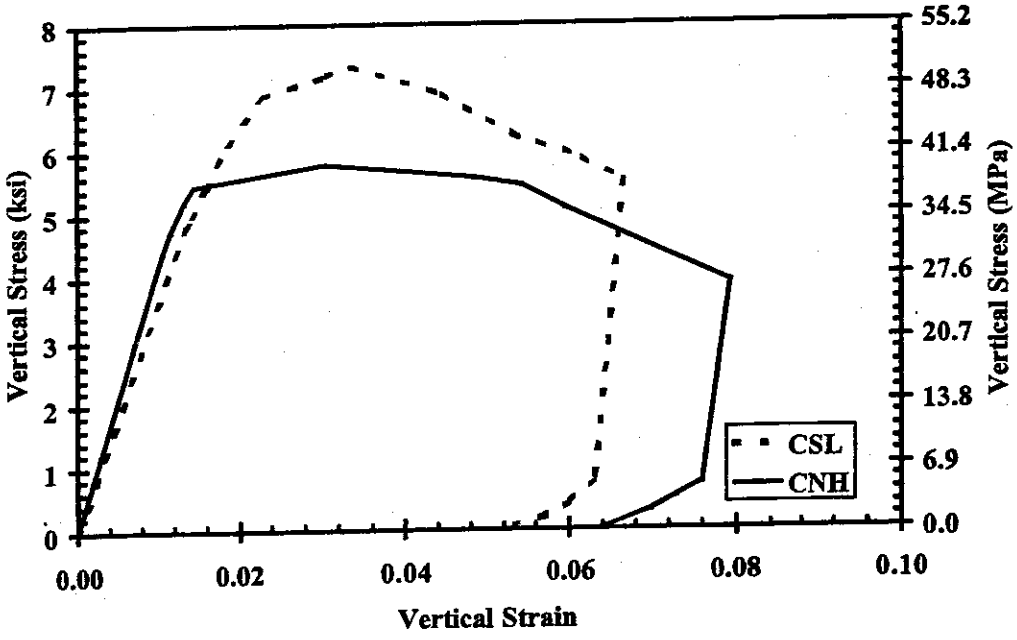

Figure 4- 2: Measured Stress-Strain Graph for C-S-L and C-N-H

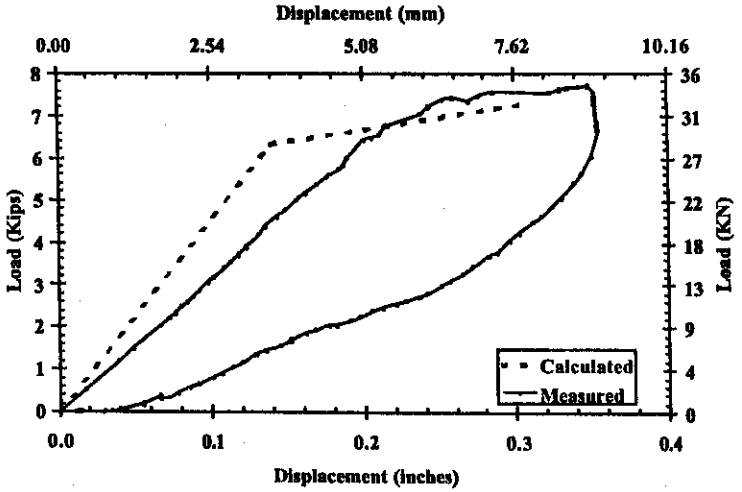

Figure 4-3: Load-Displacement, BNH1

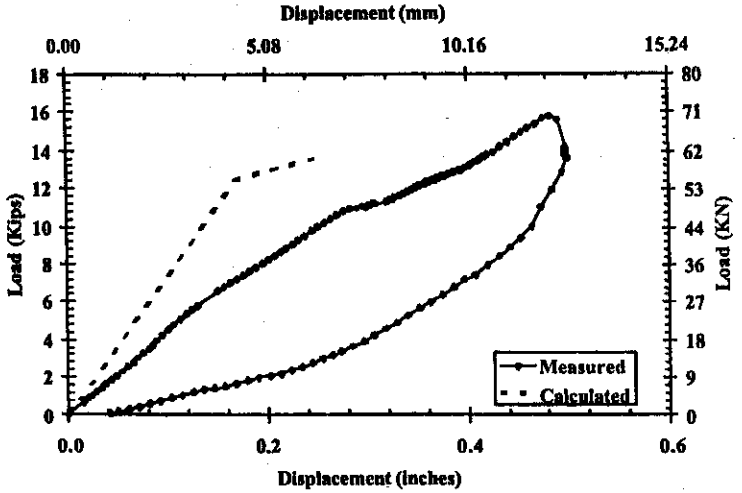

Figure 4-4: Load-Displacement, BNH2

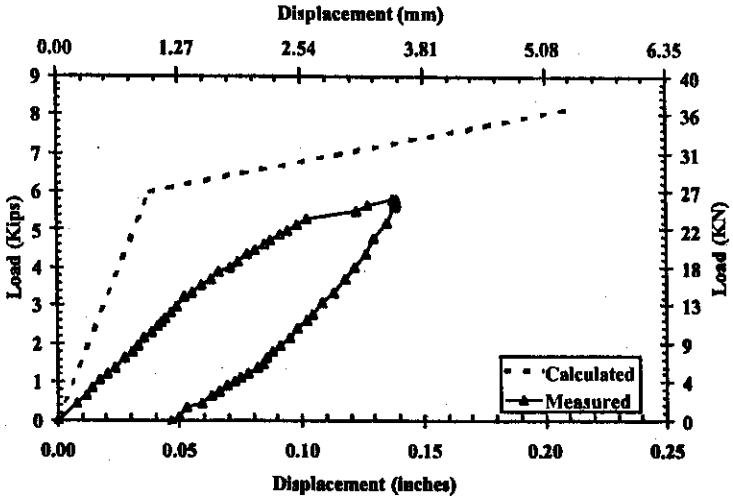

Figure 4-5: Load-Displacement, BSL1

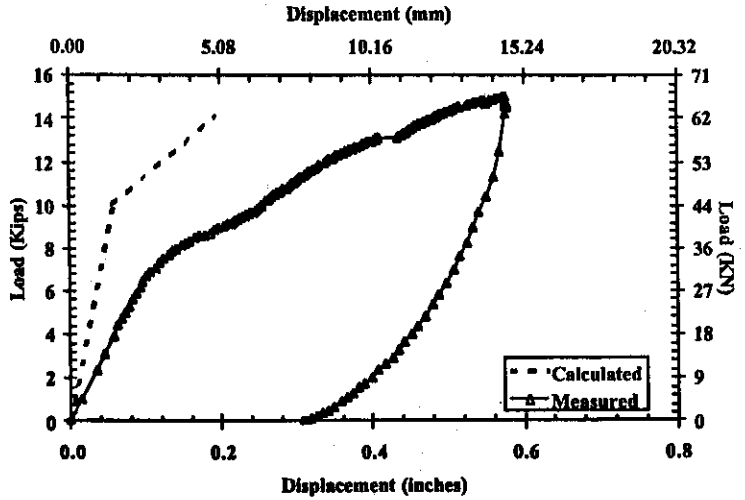

Figure 4-6: Load-Displacement, BSL2

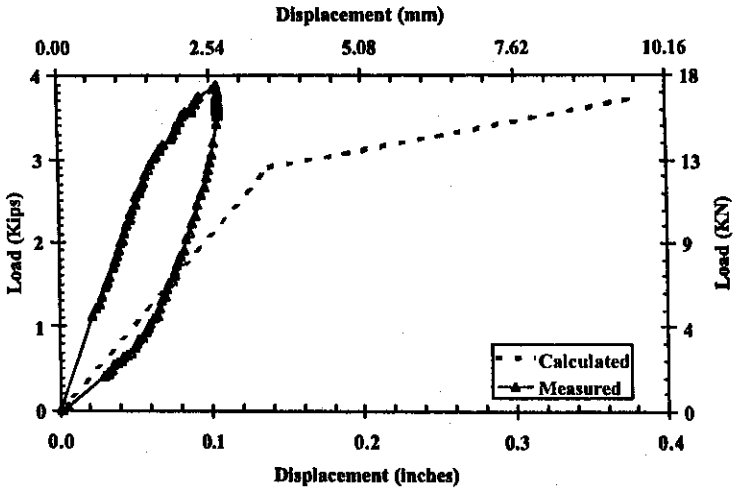

Figure 4-7: Load-Displacement, BNL1

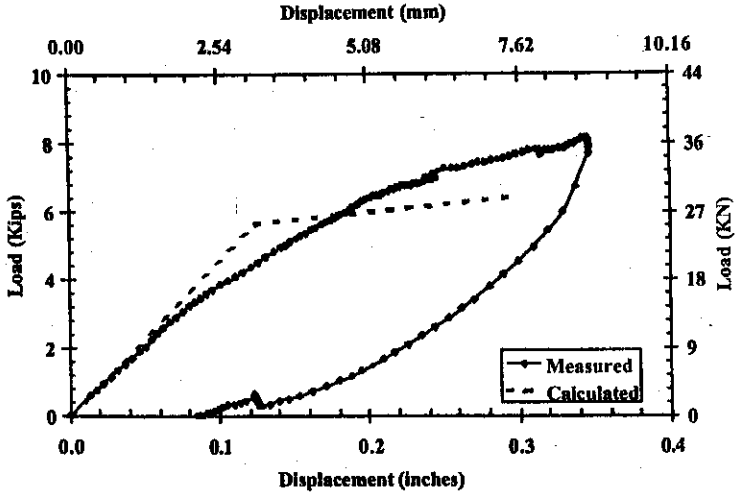

Figure 4-8: Load-Displacement, BNL2

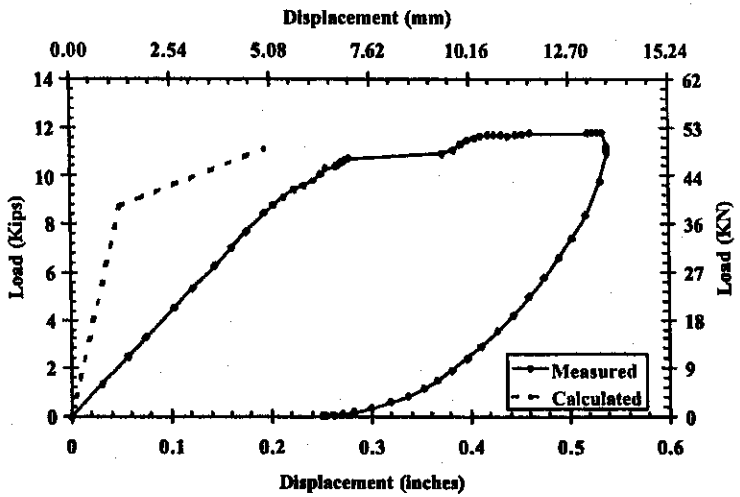

Figure 4-9: Load-Displacement, BSH1

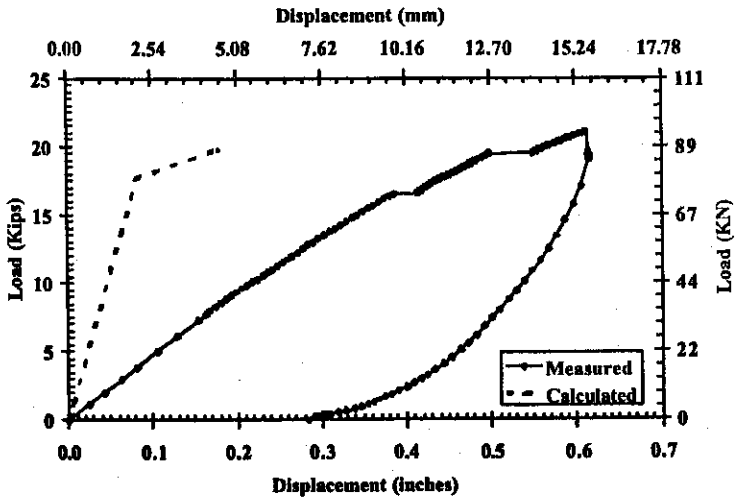

Figure 4-10: Load-Displacement, BSH2

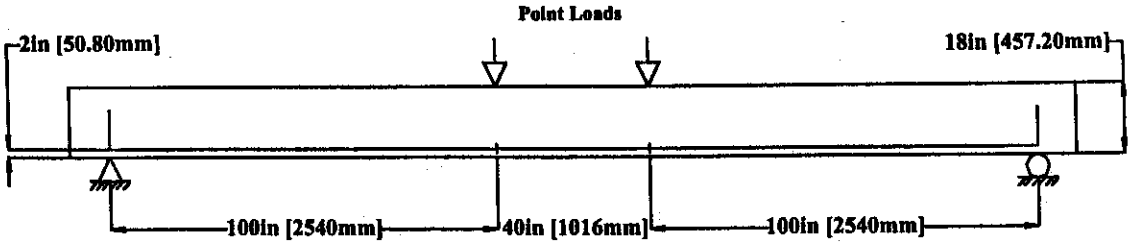

Figure 4-11: Beam Elevation

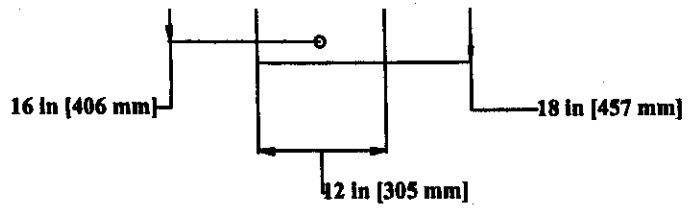

Figure 4-12: Beam Cross-Section

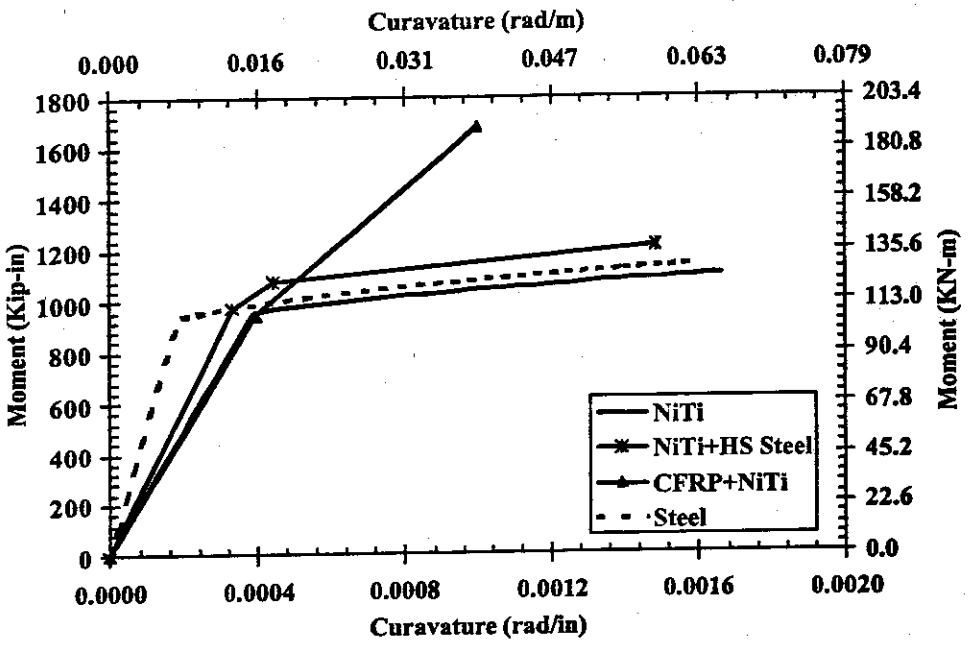

Figure 4-13: Moment-Curvature Relationship for Beam Sections

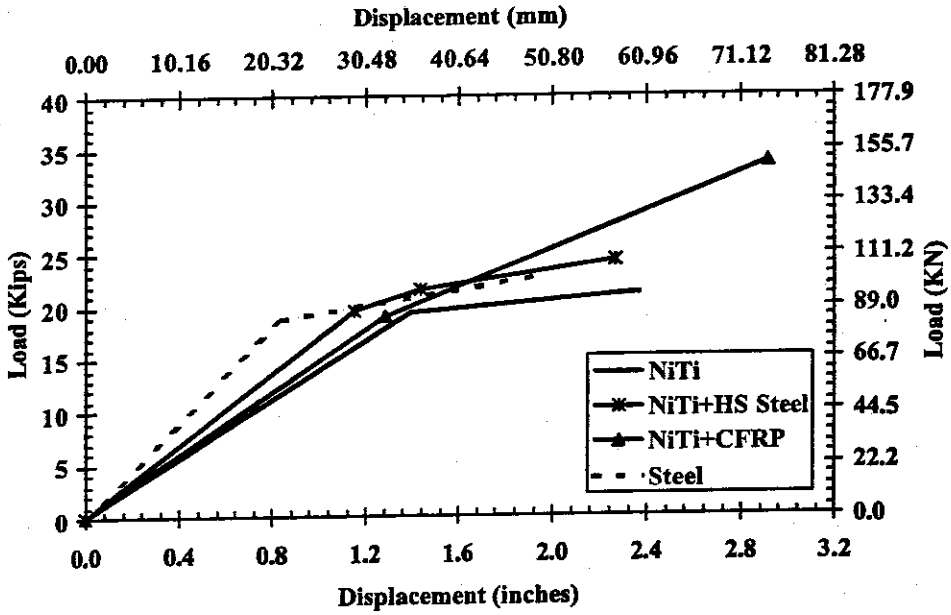

Figure 4-14: Load-Displacement Relationship for Beams

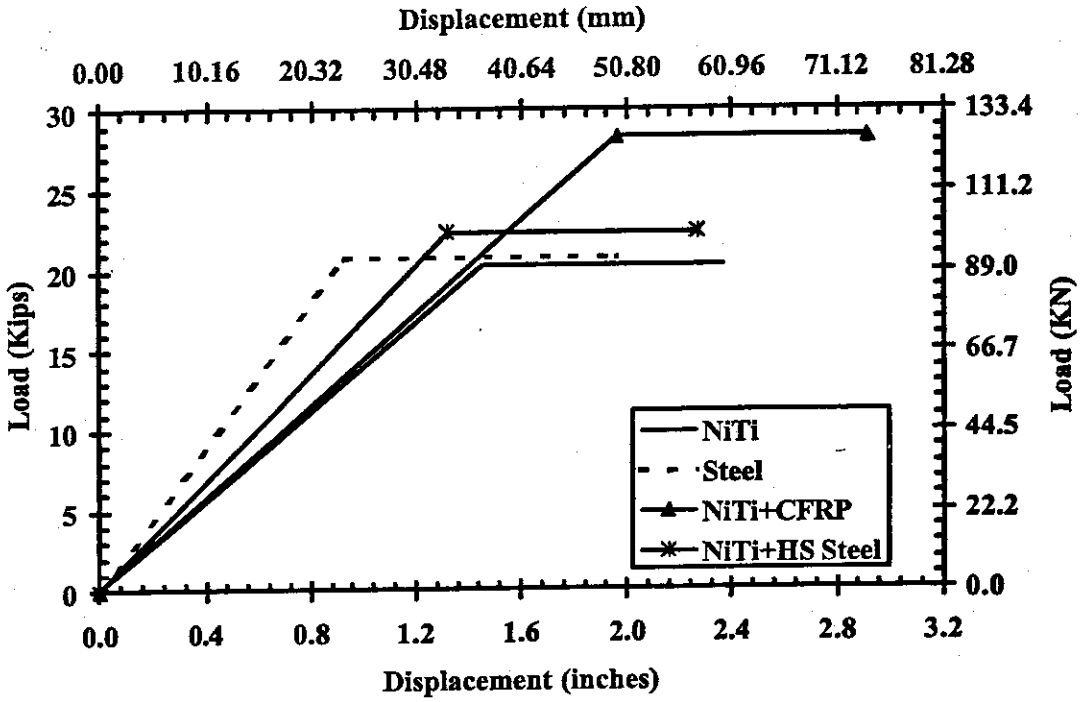

Figure 4-15: Elasto-Plastic Load-Displacement for Relationship for Beams

LIST OF CCEER PUBLICATIONS

Report No. Publication

CCEER-84-1 Saiidi, M., and R. Lawver, "User's Manual for LZAK-C64, A Computer Program to Implement the Q-Model on Commodore 64," Civil Engineering Department, Report No. CCEER-84-1, University of Nevada, Reno, January 1984.

CCEER-84-2 Douglas, B. and T. Iwasaki, "Proceedings of the First USA-Japan Bridge Engineering Workshop," held at the Public Works Research Institute, Tsukuba, Japan, Civil Engineering Department, Report No. CCEER-84-2, University of Nevada, Reno, April 1984.

CCEER-84-3 Saiidi, M., J. Hart, and B. Douglas, "Inelastic Static and Dynamic Analysis of Short R/C Bridges Subjected to Lateral Loads," Civil Engineering Department, Report No. CCEER-84-3, University of Nevada, Reno, July 1984.

CCEER-84-4 Douglas, B., "A Proposed Plan for a National Bridge Engineering Laboratory," Civil Engineering Department, Report No. CCEER-84-4, University of Nevada, Reno, December 1984.

CCEER-85-1 Norris, G. and P. Abdollaholiaee, "Laterally Loaded Pile Response: Studies with the Strain Wedge Model," Civil Engineering Department, Report No. CCEER-85-1, University of Nevada, Reno, April 1985.

CCEER-86-1 Ghusn, G. and M. Saiidi, "A Simple Hysteretic Element for Biaxial Bending of R/C in NEABS-86," Civil Engineering Department, Report No. CCEER-86-1, University of Nevada, Reno, July 1986.

CCEER-86-2 Saiidi, M., R. Lawver, and J. Hart, "User's Manual of ISADAB and SIBA, Computer Programs for Nonlinear Transverse Analysis of Highway Bridges Subjected to Static and Dynamic Lateral Loads," Civil Engineering Department, Report No. CCEER-86-2, University of Nevada, Reno, September 1986.

CCEER-87-1 Siddharthan, R., "Dynamic Effective Stress Response of Surface and Embedded Footings in Sand," Civil engineering Department, Report No. CCEER-86-2, University of Nevada, Reno, June 1987.

CCEER-87-2 Norris, G. and R. Sack, "Lateral and Rotational Stiffness of Pile Groups for Seismic Analysis of Highway Bridges," Civil Engineering Department, Report No. CCEER-87-2, University of Nevada, Reno, June 1987.

CCEER-88-1 Orie, J. and M. Saiidi, "A Preliminary Study of One-Way Reinforced Concrete Pier Hinges Subjected to Shear and Flexure," Civil Engineering Department, Report No. CCEER-88-1, University of Nevada, Reno, January 1988.

CCEER-88-2 Orie, D., M. Saiidi, and B. Douglas, "A Micro-CAD System for Seismic Design of Regular Highway Bridges," Civil Engineering Department, Report No. CCEER-88-2, University of Nevada, Reno, June 1988.

CCEER-88-3 Orie, D. and M. Saiidi, "User's Manual for Micro-SARB, a Microcomputer Program for Seismic Analysis of Regular Highway Bridges," Civil Engineering Department, Report No. CCEER-88-3, University of Nevada, Reno, October 1988.

CCEER-89-1 Douglas, B., M. Saiidi, R. Hayes, and G. Holcomb, "A Comprehensive Study of the Loads and Pressures Exerted on Wall Forms by the Placement of Concrete," Civil Engineering Department, Report No. CCEER-89-1, University of Nevada, Reno, February 1989.

CCEER-89-2 Richardson, J. and B. Douglas, "Dynamic Response Analysis of the Dominion Road Bridge Test Data," Civil Engineering Department, Report No. CCEER-89-2, University of Nevada, Reno, March 1989.

CCEER-89-2 Vrontinos, S., M. Saiidi, and B. Douglas, "A Simple Model to Predict the Ultimate Response of R/C Beams with Concrete Overlays," Civil Engineering Department, Report NO. CCEER-89-2, University of Nevada, Reno, June 1989.

CCEER-89-3 Ebrahimpour, A. and P. Jagadish, "Statistical Modeling of Bridge Traffic Loads - A Case Study," Civil Engineering Department, Report No. CCEER-89-3, University of Nevada, Reno, December 1989.

CCEER-89-4 Shields, J. and M. Saiidi, "Direct Field Measurement of Prestress Losses in Box Girder Bridges," Civil Engineering Department, Report No. CCEER-89-4, University of Nevada, Reno, December 1989.

CCEER-90-1 Saiidi, M., E. Maragakis, G. Ghusn, Y. Jiang, and D. Schwartz, "Survey and Evaluation of Nevada's Transportation Infrastructure, Task 7.2 - Highway Bridges, Final Report," Civil Engineering Department, Report No. CCEER 90-1, University of Nevada, Reno, October 1990.

CCEER-90-2 Abdel-Ghaffar, S., E. Maragakis, and M. Saiidi, "Analysis of the Response of Reinforced Concrete Structures During the Whittier Earthquake 1987,"

Civil Engineering Department, Report No. CCEER 90-2, University of Nevada, Reno, October 1990.

CCEER-91-1 Saiidi, M., E. Hwang, E. Maragakis, and B. Douglas, "Dynamic Testing and the Analysis of the Flamingo Road Interchange," Civil Engineering Department, Report No. CCEER-91-1, University of Nevada, Reno, February 1991.

CCEER-91-2 Norris, G., R. Siddharthan, Z. Zafir, S. Abdel-Ghaffar, and P. Gowda, "Soil-Foundation-Structure Behavior at the Oakland Outer Harbor Wharf," Civil Engineering Department, Report No. CCEER-91-2, University of Nevada, Reno, July 1991.

CCEER-91-3 Norris, G., "Seismic Lateral and Rotational Pile Foundation Stiffnesses at Cypress," Civil Engineering Department, Report No. CCEER-91-3, University of Nevada, Reno, August 1991.

CCEER-91-4 O'Connor, D. and M. Saiidi, "A Study of Protective Overlays for Highway Bridge Decks in Nevada, with Emphasis on Polyester-Styrene Polymer Concrete," Civil Engineering Department, Report No. CCEER-91-4, University of Nevada, Reno, October 1991.

CCEER-91-5 O'Connor, D.N. and M. Saiidi, "Laboratory Studies of Polyester-Styrene Polymer Concrete Engineering Properties," Civil Engineering Department, Report No. CCEER-91-5, University of Nevada, Reno, November 1991.

CCEER-92-1 Straw, D.L. and M. Saiidi, "Scale Model Testing of One-Way Reinforced Concrete Pier Hinges Subject to Combined Axial Force, Shear and Flexure," edited by D.N. O'Connor, Civil Engineering Department, Report No. CCEER-92-1, University of Nevada, Reno, March 1992.

CCEER-92-2 Wehbe, N., M. Saiidi, and F. Gordaninejad, "Basic Behavior of Composite Sections Made of Concrete Slabs and Graphite Epoxy Beams," Civil Engineering Department, Report No. CCEER-92-2, University of Nevada, Reno, August 1992.

CCEER-92-3 Saiidi, M. and E. Hutchens, "A Study of Prestress Changes in A Post-Tensioned Bridge During the First 30 Months," Civil Engineering Department, Report No. CCEER-92-3, University of Nevada, Reno, April 1992.

CCEER-92-4 Saiidi, M., B. Douglas, S. Feng, E. Hwang, and E. Maragakis, "Effects of Axial Force on Frequency of Prestressed Concrete Bridges," Civil Engineering Department, Report No. CCEER-92-4, University of Nevada,

Reno, August 1992.

CCEER-92-5 Siddharthan, R., and Z. Zafir, "Response of Layered Deposits to Traveling Surface Pressure Waves," Civil Engineering Department, Report No. CCEER-92-5, University of Nevada, Reno, September 1992.

CCEER-92-6 Norris, G., and Z. Zafir, "Liquefaction and Residual Strength of Loose Sands from Drained Triaxial Tests," Civil Engineering Department, Report No. CCEER-92-6, University of Nevada, Reno, September 1992.

CCEER-92-7 Douglas, B., "Some Thoughts Regarding the Improvement of the University of Nevada, Reno's National Academic Standing," Civil Engineering Department, Report No. CCEER-92-7, University of Nevada, Reno, September 1992.

CCEER-92-8 Saiidi, M., E. Maragakis, and S. Feng, "An Evaluation of the Current Caltrans Seismic Restrainer Design Method," Civil Engineering Department, Report No. CCEER-92-8, University of Nevada, Reno, October 1992.

CCEER-92-9 O'Connor, D., M. Saiidi, and E. Maragakis, "Effect of Hinge Restrainers on the Response of the Madrone Drive Undercrossing During the Loma Prieta Earthquake," Civil Engineering Department, Report No. CCEER-92-9, University of Nevada, Reno, February 1993.

CCEER-92-10 O'Connor, D., and M. Saiidi, "Laboratory Studies of Polyester Concrete: Compressive Strength at Elevated Temperatures and Following Temperature Cycling, Bond Strength to Portland Cement Concrete, and Modulus of Elasticity," Civil Engineering Department, Report No. CCEER-92-10, University of Nevada, Reno, February 1993.

CCEER-92-11 Wehbe, N., M. Saiidi, and D. O'Connor, "Economic Impact of Passage of Spent Fuel Traffic on Two Bridges in Northeast Nevada," Civil Engineering Department, Report No. CCEER-92-11, University of Nevada, Reno, December 1992.

CCEER-93-1 Jiang, Y., and M. Saiidi, "Behavior, Design, and Retrofit of Reinforced Concrete One-way Bridge Column Hinges," edited by D. O'Connor, Civil Engineering Department, Report No. CCEER-93-1, University of Nevada, Reno, March 1993.

CCEER-93-2 Abdel-Ghaffar, S., E. Maragakis, and M. Saiidi, "Evaluation of the Response of the Aptos Creek Bridge During the 1989 Loma Prieta Earthquake," Civil Engineering Department, Report No. CCEER-93-2,

University of Nevada, Reno, June 1993.

CCEER-93-3 Sanders, D.H., B.M. Douglas, and T.L. Martin, "Seismic Retrofit Prioritization of Nevada Bridges," Civil Engineering Department, Report No. CCEER-93-3, University of Nevada, Reno, July 1993.

CCEER-93-4 Abdel-Ghaffar, S., E. Maragakis, and M. Saiidi, "Performance of Hinge Restrainers in the Huntington Avenue Overhead During the 1989 Loma Prieta Earthquake," Civil Engineering Department, Report No. CCEER-93-4, University of Nevada, Reno, June 1993 (in final preparation).

CCEER-93-5 Maragakis, E., M. Saiidi, S. Feng, and L. Flournoy, "Effects of Hinge Restrainers on the Response of the San Gregorio Bridge During the Loma Prieta Earthquake," (in final preparation) Civil Engineering Department, Report No. CCEER-93-5, University of Nevada, Reno.

CCEER-93-6 Saiidi, M., E. Maragakis, S. Abdel-Ghaffar, S. Feng, and D. O'Connor, "Response of Bridge Hinge Restrainers During Earthquakes -Field Performance, Analysis, and Design," Civil Engineering Department, Report No. CCEER-93-6, University of Nevada, Reno, May 1993.

CCEER-93-7 Wehbe, N., Saiidi, M., Maragakis, E., and Sanders, D., "Adequacy of Three Highway Structures in Southern Nevada for Spent Fuel Transportion, Civil Engineering Department, Report No. CCEER-93-7, University of Nevada, Reno, August 1993.

CCEER-93-8 Roybal, J., Sanders, D.H., and Maragakis, E., "Vulnerability Assessment of Masonry in the Reno-Carson City Urban Corridor," Civil Engineering Department, Report No. CCEER-93-8, University of Nevada, Reno, May 1993.

CCEER-93-9 Zafir, Z. and Siddharthan, R., "MOVLOAD: A Program to Determine the Behavior of Nonlinear Horizontally Layered Medium Under Moving Load," Civil Engineering Department, Report No. CCEER-93-9, University of Nevada, Reno, August 1993.

CCEER-93-10 O'Connor, D.N., Saiidi, M., and Maragakis, E.A., "A Study of Bridge Column Seismic Damage Susceptibility at the Interstate 80/U.S. 395 Interchange in Reno, Nevada," Civil Engineering Department, Report No. CCEER-93-10, University of Nevada, Reno, October 1993.

CCEER-94-1 Maragakis, E., B. Douglas, and E. Abdelwahed, "Preliminary Dynamic Analysis of a Railroad Bridge," Report CCEER-94-1, January 1994.

CCEER-94-2 Douglas, B.M., Maragakis, E.A., and Feng, S., "Stiffness Evaluation of Pile Foundation of Cazenovia Creek Overpass," Civil Engineering Department, Report No. CCEER-94-2, University of Nevada, Reno, March 1994.

CCEER-94-3 Douglas, B.M., Maragakis, E.A., and Feng, S., "Summary of Pretest Analysis of Cazenovia Creek Bridge," Civil Engineering Department, Report No. CCEER-94-3, University of Nevada, Reno, April 1994.

CCEER-94-4 Norris, G.M. and Madhu, R., "Liquefaction and Residual Strength of Sands from Drained Triaxial Tests, Report 2," Civil Engineering Department, CCEER-94-4, University of Nevada, Reno, August 1994.

CCEER-94-5 Saiidi, M., Hutchens, E., and Gardella, D., "Prestress Losses in a Post-Tensioned R/C Box Girder Bridge in Southern Nevada," Civil Engineering Department, CCEER-94-5, University of Nevada, Reno, August 1994.

CCEER-95-1 Siddharthan, R., El-Gamal, M., and Maragakis, E.A., "Nonlinear Bridge Abutment , Verification, and Design Curves," Civil Engineering Department, CCEER-95-1, University of Nevada, Reno, January 1995.

CCEER-95-2 Norris, G.M., Madhu, R., Valceschini, R., and Ashour, M., "Liquefaction and Residual Strength of Loose Sands from Drained Triaxial Tests," Report 2, Civil Engineering Department, Report No. CCEER-95-2, University of Nevada, Reno, February 1995.

CCEER-95-3 Wehbe, N., Saiidi, M., Sanders, D., and Douglas, B., "Ductility of Rectangular Reinforced Concrete Bridge Columns with Moderate Confinement,"Civil Engineering Department, Report No. CCEER-95-3, University of Nevada, Reno, July 1995.

CCEER-95-4 Martin, T., Saiidi, M., and Sanders, D., "Seismic Retrofit of Column-Pier Cap Connections in Bridges in Northern Nevada," Civil Engineering Department, Report No. CCEER-95-4, University of Nevada, Reno, August 1995.

CCEER-95-5 Darwish, I., Saiidi, M., and Sanders, D., "Experimental Study of Seismic Susceptibility Column-Footing Connections," Civil Engineering Department, Report No. CCEER-95-5, University of Nevada, Reno, September 1995.

CCEER-95-6 Griffin, G., Saiidi, M., and Maragakis, E., "Nonlinear Seismic Response of Isolated Bridges and Effects of Pier Ductility Demand," Civil Engineering Department, Report No. CCEER-95-6, University of Nevada, Reno,

November 1995.

CCEER-95-7 Acharya, S., Saiidi, M., and Sanders, D., "Seismic Retrofit of Bridge Footings and Column-Footing Connections," Report for the Nevada Department of Transportation, Civil Engineering Department, Report No. CCEER-95-7, University of Nevada, Reno, November 1995.

CCEER-95-8 Maragakis, E., Douglas, B., and Sandirasegaram, U., "Full-Scale Field Resonance Tests of a Railway Bridge," A Report to the Association of American Railroads, Civil Engineering Department, Report No. CCEER-95-8, University of Nevada, Reno, December 1995.

CCEER-95-9 Douglas, B., Maragakis, E., and Feng, S., "System Identification Studies on Cazenovia Creek Overpass," Report for the National Center for Earthquake Engineering Research, Civil Engineering Department, Report No. CCEER-95-9, University of Nevada, Reno, October 1995.

CCEER-96-1 El-Gamal, M.E. and Siddharthan, R.V., "Programs to Computer Translational Stiffness of Seat-Type Bridge Abutment," Civil Engineering Department, Report No. CCEER-96-1, University of Nevada, Reno, March 1996.

CCEER-96-2 Labia, Y., Saiidi, M., and Douglas, B., "Evaluation and Repair of Full-Scale Prestressed Concrete Box Girders," A Report to the National Science Foundation, Research Grant CMS-9201908, Civil Engineering Department, Report No. CCEER-96-2, University of Nevada, Reno, May 1996.

CCEER-96-3 Darwish, I., Saiidi, M., and Sanders, D., "Seismic Retrofit of R/C Oblong Tapered Bridge Columns with Inadequate Bar Anchorage in Columns and Footings," A Report to the Nevada Department of Transportation, Civil Engineering Department, Report No. CCEER-96-3, University of Nevada, Reno, May 1996.

CCEER-96-4 Ashour, M., Pilling, P., Norris, G., and Perez, H., "The Prediction of Lateral Load Behavior of Single Piles and Pile Groups Using the Strain Wedge Model," A Report to the California Department of Transportation, Civil Engineering Department, Report No. CCEER-96-4, University of Nevada, Reno, June, 1996.

CCEER-97-1-A Rimal, P. and Itani, A. "Sensitivity Analysis of Fatigue Evaluations of Steel Bridges", Center for Earthquake Research, Department of Civil Engineering, University of Nevada, Reno, Nevada Report No. CCEER-97-1-A, September, 1997.

CCEER-97-1-B Maragakis, E., Douglas, B., and Sandirasegaram, U. "Full-Scale Field Resonance Tests of a Railway Bridge," A Report to the Association of American Railroads, Civil Engineering Department, University of Nevada, Reno, May, 1996.

CCEER-97-2 Wehbe, N., Saiidi, M., and D. Sanders, "Effect of Confinement and Flares on the Seismic Performance of Reinforced Concrete Bridge Columns," Civil Engineering Department, Report No. CCEER-97-2, University of Nevada, Reno, September 1997.

CCEER-97-3 Darwish, I., M. Saiidi, G. Norris, and E. Maragakis, "Determination of In-Situ Footing Stiffness Using Full-Scale Dynamic Field Testing," A Report to the Nevada Department of Transportation, Structural Design Division, Carson City, Nevada, Report No. CCEER-97-3, University of Nevada, Reno, October 1997.

CCEER-97-4 Wehbe, N., and M. Saiidi, "User's manual for RCMC v. 1.2 : A Computer Program for Moment-Curvature Analysis of Confined and Unconfined Reinforced Concrete Sections," Center for Civil Engineering Earthquake Research, Department of Civil Engineering, University of Nevada, Reno, Nevada, Report No. CCEER-97-4, November, 1997.

CCEER-97-5 Isakovic, T., M. Saiidi, and A. Itani, "Influence of new Bridge Configurations on Seismic Performance," Department of Civil Engineering, University of Nevada, Reno, Report No. CCEER-97-5, September, 1997.

CCEER-98-1 Itani, A., Vesco, T. and Dietrich, A., "Cyclic Behavior of "as Built" Laced Members With End Gusset Plates on the San Francisco Bay Bridge" Center for Civil Engineering Earthquake Research, Department of Civil Engineering, University of Nevada, Reno, Nevada Report No. CCEER-98-1, March, 1998.

CCEER-98-2 G. Norris and M. Ashour, "Liqueficiation and Undraned response evaluation of Sands from Drained Formulation." Center for Civil Engineering Earthquake Research, Department of Civil Engineering, University of Nevada, Reno, Nevada, Report No. CCEER-98-2, May, 1998.

CCEER-98-3 Qingbin, Chen, B. M. Douglas, E. Maragakis, and I. G. Buckle, "Extraction of Nonlinear Hysteretic Properties of Seismically Isolated Bridges from Quick-Release Field Tests", Center for Civil Engineering Earthquake Research, Department of Civil Engineering, University of Nevada, Reno, Nevada, Report No. CCEER-98-3, June, 1998.

CCEER-98-4 Maragakis, E., B. M. Douglas, and C. Qingbin, "Full-Scale Field Capacity

Tests of a Railway Bridge", Center for Civil Engineering Earthquake Research, Department of Civil Engineering, University of Nevada, Reno, Nevada, Report No. CCEER-98-4, June, 1998.

CCEER-98-5 Itani, A., Douglas, B., and Woodgate, J., "Cyclic Behavior of Richmond-San Rafael Retrofitted Tower Leg". Center for Civil Engineering Earthquake Research, Department of Civil Engineering, University of Nevada, Reno. Report No. CCEER-98-5, June 1998

CCEER-98-6 Moore, R., Saiidi, M., and Itani, A., "Seismic Behavior of New Bridges with Skew and Curvature". Center for Civil Engineering Earthquake Research, Department of Civil Engineering, University of Nevada, Reno. Report No. CCEER-98-6, October, 1998.

CCEER-98-7 Itani, A and Dietrich, A, "Cyclic Behavior of Double Gusset Plate Connections", Center for Civil Engineering Earthquake Research, Department of Civil Engineering, University of Nevada, Reno, Nevada, Report No. CCEER-98-5, December, 1998.

CCEER-99-1 Caywood, C., M. Saiidi, and D. Sanders, " Seismic Retrofit of Flared Bridge Columns With Steel Jackets," Civil Engineering Department, University of Nevada, Reno, Report No. CCEER-99-1, February 1999.

CCEER-99-2 Mangoba, N., M. Mayberry, and M. Saiidi, "Prestress Loss in Four Box Girder Bridges in Northern Nevada," Civil Engineering Department, University of Nevada, Reno, Report No. CCEER-99-2, March 1999.

CCEER-99-3 Abo-Shadi, N., M. Saiidi, and D. Sanders, "Seismic Response of Bridge Pier Walls in the Weak Direction", Civil Engineering Department, University of Nevada, Reno, Report No. CCEER-99-3, April 1999.

CCEER-99-4 Buzick, A., and M. Saiidi, "Shear Strength and Shear Fatigue Behavior of Full-Scale Prestressed Concrete Box Girders", Civil Engineering Department, University of Nevada, Reno, Report No. CCEER-99-4, April 1999.

CCEER-99-5 Randall, M., M. Saiidi, E. Maragakis and T. Isakovic, "Restrainer Design Procedures For Multi-Span Simply-Supported Bridges", Civil Engineering Department, University of Nevada, Reno, Report No. CCEER-99-5, April 1999.

CCEER-99-6 Wehbe, N. and M. Saiidi, "User's Manual for RCMC v. 1.2, A Computer Program for Moment-Curvature Analysis of Confined and Unconfined Reinforced Concrete Sections", Civil Engineering Department, University

of Nevada, Reno, Report No. CCEER-99-6, May 1999.

CCEER-99-7 Burda, J. and A. Itani, "Studies of Seismic Behavior of Steel Base Plates," Civil Engineering Department, University of Nevada, Reno, Report No. CCEER-99-7, May 1999.

CCEER-99-8 Ashour, M., and G. Norris, "Refinement of the Strain Wedge Model Program," Civil Engineering Department, University of Nevada, Reno, Report No. CCEER-99-8, March 1999.

CCEER-99-9 Dietrich, A., and A. Itani, "Cyclic Behavior of Laced and Perforated Steel Members on the San Francisco-Oakland Bay Bridge," Civil Engineering Department, University, Reno. December 1999.

CCEER 99-10 Itani, A., A. Dietrich, "Cyclic Behavior of Built Up Steel Members and their Connections," Civil Engineering Department, University of Nevada, Reno. December 1999.

CCEER 99-11 Itani, A., J. Woodgate, "Axial and Rotational Ductility of BuiltUp Structural Steel Members," Civil Engineering Department, University of Nevada, Reno December 1999.

CCEER-99-12 Sgambelluri, M., Sanders, D.H., and Saiidi, M.S., Behavior of One-Way Reinforced Concrete Bridge Column Hinges in the Weak Direction, Report No. Department of Civil Engineering, University of Nevada, Reno, December 1999.

CCEER-99-13 Laplace, P., Sanders, D.H., Douglas, B, and Saiidi, M, "Shake Table Testing of Flexure Dominated Reinforced Concrete Bridge Columns," Report No. 99-13,
Department of Civil Engineering, University of Nevada, Reno, December 1999.

CCEER-99-14 Ahmad M. Itani, Jose A. Zepeda, and Elizabeth A. Ware "Cyclic Behavior of Steel Moment Frame Connections for the Moscone Center Expansion," Report No. 99-14,
Department of Civil Engineering, University of Nevada, Reno December 1999.

CCEER 00-1 Ashour, M., and Norris, G. "Undrained Lateral Pile and Pile Group Response in Saturated Sand", Civil Engineering Department, University of Nevada, Reno, Report No. CCEER-00-1, May 1999. January 2000.

CCEER 00-2 Saiidi, M. and Wehbe, N., "A Comparison of Confinement Requirements in Different Codes for Rectangular, Circular, and Double-Spiral RC Bridge Columns," Civil Engineering Department, University of Nevada, Reno, Report No. CCEER-00-2, January 2000.

CCEER 00-3 McElhaney, B., M. Saiidi, and D. Sanders, "Shake Table Testing of Flared Bridge Columns With Steel Jacket Retrofit," Civil Engineering Department, University of Nevada, Reno, Report No. CCEER-00-3, January 2000.

CCEER 00-4 Martinovic, F., M. Saiidi, D. Sanders, and F. Gordaninejad, "Dynamic Testing of Non-Prismatic Reinforced Concrete Bridge Columns Retrofitted with FRP Jackets," Civil Engineering Department, University of Nevada, Reno, Report No. CCEER-00-4, January 2000.

CCEER 00-5 Itani, A., and M. Saiidi, "Seismic Evaluation of Steel Joints for UCLA Center for Health Science Westwood Replacement Hospital," Civil Engineering Department, University of Nevada, Reno, Report No. CCEER-00-5, February 2000.

CCEER 00-6 Will, J. and D. Sanders, "High Performance Concrete Using Nevada Aggregates," Civil Engineering Department, University of Nevada, Reno, Report No. CCEER-00-6, May 2000.

CCEER 00-7 French, C., and M. Saiidi, "A Comparison of Static and Dynamic Performance of Models of Flared Bridge Columns ," Civil Engineering Department, University of Nevada, Reno, Report No. CCEER-00-7, October 2000.

CCEER 00-8 Itani, A., H. Sedarat, "Seismic Analysis of the AISI LRFD Design Example of Steel Highway Bridges," Civil Engineering Department, University of Nevada, Reno, Report No. CCEER 00-08, November 2000.

CCEER 00-9 Moore, J., D. Sanders, and M. Saiidi, "Shake Table Testing of 1960's Two Column Bent with Hinges Bases," Civil Engineering Department, University of Nevada, Reno, Report No. CCEER 00-09, December 2000.

CCEER 00-10 Asthana, M., D. Sanders, and M. Saiidi, "One-Way Reinforced Concrete Bridge Column Hinges in the Weak Direction," Civil Engineering Department, University of Nevada, Reno, Report No. CCEER 00-10, April 2001.

CCEER 01-1 Ah Sha, H., D. Sanders, M. Saiidi, "Early Age Shrinkage and Cracking of Nevada Concrete Bridge Decks, "Civil Engineering Department, University of Nevada, Reno, Report No. CCEER 01-01, May 2001.

CCEER 01-2 Ashour, M. and G. Norris, "Pile Group program for Full Material Modeling an Progressive Failure." Civil Engineering Department, University of Nevada, Reno, Report No. CCEER 01-02, July 2001.

CCEER 01-3 Itani, A., C. Lanaud, and P. Dusicka, "Non-Linear Finite Element Analysis of Built-Up Shear Links." Civil Engineering Department, University of Nevada, Reno, Report No. CCEER 01-03, July 2001.

CCEER 01-4 Saiidi, M., J. Mortensen, and F. Martinovic, "Analysis and Retrofit of Fixed Flared Columns with Glass Fiber-Reinforced Plastic Jacketing," Civil Engineering Department, University of Nevada, Reno, Report No. CCEER 01-4, August 2001

CCEER 01-5 Saiidi, M., A. Itani, I. Buckle, and Z. Cheng," Performance of A Full-Scale Two-Story Wood Frame Structure Supported on Ever-Level Isolators," Civil Engineering Department, University of Nevada, Reno, Report No. CCEER 01-5, October 2001

CCEER 01-6 Laplace, P., D. Sanders, and M. Saiidi, "Experimental Study and Analysis of Retrofitted Flexure and Shear Dominated Circular Reinforced Concrete Bridge Columns Subjected to Shake Table Excitation, "Civil Engineering Department, University of Nevada, Reno, Report No. CCEER 01-6, June 2001.

CCEER 01-7 Reppi, F., and D. Sanders, "Removal and Replacement of Cast-in-Place, Post-tensioned, Box Girder Bridge," Civil Engineering Department, University of Nevada, Reno, Report No. CCEER 01-7, December 2001.

CCEER 02-1 Pulido, C., M. Saiidi, D. Sanders, and A. Itani, "Seismic Performance and Retrofitting of Reinforced Concrete Bridge Bents," Civil Engineering Department, University of Nevada, Reno, Report No. CCEER 02-1, January 2002.

CCEER 02-2 Yang, Q., M. Saiidi, H. Wang, and A. Itani, "Influence of Ground Motion Incoherency on Earthquake Response of Multi-Support Structures," Civil Engineering Department, University of Nevada, Reno, Report No. CCEER 02-2, May 2002.

CCEER 02-3 M. Saiidi, B. Gopalakrishnan, E. Reinhardt, and R. Siddharthan, A Preliminary Study of Shake Table Response of A Two-Column Bridge Bent on Flexible Footings
Civil Engineering Department, University of Nevada, Reno, Report No. CCEER 02-03,

June 2002.

CCEER 02-4 Not Published

CCEER 02-5 Banghart, A., Sanders, D., Saiidi, M., "Evaluation of Concrete Mixes for Filling the Steel Arches in the Galena Creek Bridge," Civil Engineering Department, University of Nevada, Reno, Report No. CCEER 02-05, June 2002.

CCEER 02-6 Dusicka, P., Itani, A., Buckle, I. G., "Cyclic Behavior of Shear Links and Tower Shaft Assembley of San Francisco – Oakland Bay Bridge Tower" Civil Engineering Department, University of Nevada, Reno, Report No. CCEER 02-06, July 2002.

CCEER 02-7 Mortensen, J., and M. Saiidi, " A Performance-Based Design Method for Confinement in Circular Columns," Civil Engineering Department, University of Nevada, Reno, Report No. CCEER 02-07, November 2002.

CCEER 03-1 Wehbe, N., and M. Saiidi, "User's manual for SPMC v. 1.0 : A Computer Program for Moment-Curvature Analysis of Reinforced Concrete Sections with Interlocking Spirals," Center for Civil Engineering Earthquake Research, Department of Civil Engineering, University of Nevada, Reno, Nevada, Report No. CCEER-03-1, May, 2003.

CCEER 03-2 Wehbe, N., and M. Saiidi, "User's manual for RCMC v. 2.0 : A Computer Program for Moment-Curvature Analysis of Confined and Unconfined Reinforced Concrete Sections," Center for Civil Engineering Earthquake Research, Department of Civil Engineering, University of Nevada, Reno, Nevada, Report No. CCEER-03-2, June, 2003.

CCEER 03-3 Nada, H., D. Sanders, and M. Saiidi, " Seismic Performance of RC Bridge Frames with Architectural-Flared Columns," Civil Engineering Department, University of Nevada, Reno, Report No. CCEER 03-3, January 2003.

CCEER 03-4 Reinhardt, E., M. Saiidi, and R. Siddharthan, " Seismic Performance of a CFRP/ Concrete Bridge Bent on Flexible Footings." Civil Engineering Department, University of Nevada, Reno. Report No. CCEER 03-4, August 2003.

CCEER 03-5 Johnson, N., M. Saiidi, A. Itani, and S. Ladkany, "Seismic Retrofit of Octagonal Columns with Pedestal and One-Way Hinge at the Base," Center for Civil Engineering Earthquake Research, Department of Civil Engineering, University of Nevada, Reno, Nevada, Report No. CCEER-03-5, August 2003.

CCEER 03-06 Mortensen, C., M. Saiidi, and S. Ladkany, "Creep and Shrinkage Losses in Highly Variable Climates," Center for Civil Engineering Earthquake Research, Department of Civil Engineering, University of Nevada, Reno, Nevada, Report No. CCEER-03-6, September 2003.

CCEER 03-07 Ayoub, C., M. Saiidi, and A. Itani, "A Study of Shape-Memory-Alloy-Reinforced Beams and Cubes," Center for Civil Engineering Earthquake Research, Department of Civil Engineering, University of Nevada, Reno, Nevada, Report No. CCEER-03-7, October 2003.

Kenny C. Guinn, Governor

Nevada Department of Transportation
Tom Stephens, P.E. Director
Prepared by Research Division
Alan Hilton, Research Manager
(775) 888-7803
ahilton@dot.state.nv.us
1263 South Stewart Street
Carson City, Nevada 89712